# Genetics of Digitocutaneous Dysplasia

Kaya Fukushima

A thesis submitted for the degree of

Bachelor of Medical Science with Honours

at the University of Otago, Dunedin,

New Zealand

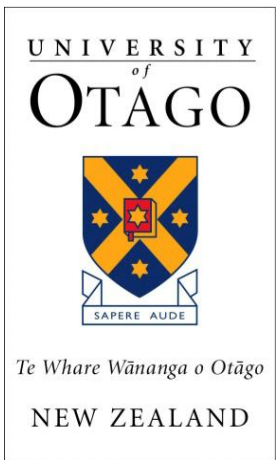


December 2020

*Think and Wonder,*
*Wonder and Think.*

*- Dr Seuss*

# Abstract

The development of the human skeleton is a precisely controlled process. The study of Mendelian diseases involving abnormalities in the skeleton enables the idenfication of factors critical to skeletal development.

Digitocutaneous dysplasia (DCD) is a rare genetic syndrome exhibiting abnormalities in the skeleton that are most pronounced in the hands and feet. This condition is caused by a single mis-splicing event that results in the in-frame deletion of 16 amino acids from the encoded filamin A protein (FLNA; NP_001104026.1:p.Val1724_Thr1739del). Tellingly, this region of FLNA has been shown to interact with the extracellular calcium-sensing receptor (CaSR). Activation of CaSR initiates downstream mitogen-activated protein kinase (MAPK) signaling that can trigger osteoblast recruitment and differentiation.

This project aimed to explore the pathomechanisms that lead to the skeletal abnormalities in DCD. This was achieved using two approaches, one examining the effects of this *FLNA* variant on osteoblast function, and the other investigating the possible involvement of CaSR.

Two immortalised cell lines, MC3T3-E1 and U2OS, were chosen to model osteoblasts. Given the murine origin of MC3T3-E1, the nucleotide sequence of mouse *Flna* was compared with that of human *FLNA*. It was discovered that rodents had what was equivalent to the pathogenic variant responsible for the mis-splicing of *FLNA* in humans. However, no mis-splicing was found in the mouse following the investigation of a publicly available mouse development RNA-seq dataset. Disrupting the splice site of interest in MC3T3-E1 using antisense oligonucleotides resulted in a mis-splicing event different to that associated with DCD. Taken together, these findings demonstrate that the regulation of splicing at this site differ between mice and humans.

Antisense oligonucleotides were also transfected into human U2OS cells but no mis-splicing was induced. Subsequently, a transient transfection approach to introduce the misspliced form of *FLNA* via a plasmid vector was initiated. A satisfactory transfection efficiency was unable to be achieved and consequently, no clear results were obtained.

Meanwhile, the expression of *CASR* was investigated using reverse transcription PCR. *CASR* was detected in mouse bone but not in two osteoblastic cell lines, MC3T3-E1 and U2OS. The apparent absence of *CASR* in these cell lines was thought to be due to this method lacking the sensitivity to detect very the low expression of this gene common in *in vitro* cultures.

The experiments utilising antisense oligonucleotides along with the exploration of interspecific differences in the nucleotide sequence of *FLNA* has led to the uncovering of putative factors that influence mis-splicing at this site. The finding of *Casr* expression in bone has called attention to the possible role that osteocytes may have in the pathogenesis of DCD. Overall, this project has laid a foundation for further work and opened up some new avenues that can be explored in the future to better understand the various aspects of this disease.

# Acknowledgements

First and foremost, I must say an enormous thank you to my supervisor Prof. Stephen Robertson. You welcomed me into your lab for a summer studentship and provided me with a stimulating experience that sparked in me a desire for more. I am so glad to have been able to undertake this BMedSc(Hons) project under your supervision. Your kind support and encouragements have been invaluable in helping me grow not only as a student researcher but as an individual.

A huge thank you also goes to Dr Emma Wade, who supervised my wet lab work and helped shape my project. Prior to this year, I had very little experience in the lab but you managed to skilfully guide me through so many techniques. I cannot thank you enough for always being so approachable and willing to answer all my questions. You seem to have an endless supply of patience and advice and your positivity kept me excited for this project.

To all members of the Robertson lab, both past and present, I would like to say thanks for being the wonderful bunch you are. A special thank you goes to Dr Zandra Jenkins for sharing her expertise and to Tim Morgan for teaching me the foundations of lab work during my summer studentship. Thank you to Liz Goodin, Ben Halliday, Amy Jones, and Annika Sjoeholm, for providing me with delightful chats and helpful advice in the lab.

I would also like to thank the friendly people I have had the pleasure of sharing my office with. A special mention goes to Meghan Mulligan who made me feel so welcome when I first arrived, and Danielle Jenkins who provided some great chats when the office was eerily empty during the first level two lockdown.

To all those people that I met in the pathology tearoom, thanks for the great company and the lively discussions during all those lunchtimes. I cannot mention you all but shoutout to Katrin Campbell, Amarni Thomas, Lorissa McDougall, Rosie Sullivan, Priyal Dass, and several others I have already mentioned, who I saw regularly.

My thanks also go out to my friends outside the Hercus building for keeping in contact and providing me with a healthy distraction. And of course I owe my family a great many thanks for their love and support.

Finally, I wish to express my grattitude towards the Maurice and Phyllis Paykel Trust and the Otago Medical School who have funded my year. Despite the unexpected challenges presented by COVID-19, this year has truly been incredible and certainly rich with learning which I will take with me into the next chapter of my life.

# Table of Contents

# List of Tables

# List of Figures

# List of Abbreviations

| | |
|---|---|
| **ACS** | American Chemical Society |
| **ADH1** | Autosomal dominant hypocalcaemia type 1 |
| **ALP** | Alkaline phosphatase |
| **AON** | Antisense oligonucleotide |
| **CaSR** | Calcium-sensing receptor |
| **cDNA** | Complementary deoxyribonucleic acid |
| **CES** | Combined enhancer solution |
| **CKCO** | Condition characterised by contractures, keloid, cardiac and optic anomalies |
| **CST** | Cell Signaling Technology |
| **ddNTP** | Dideoxynucleotide triphosphate |
| **DCD** | Digitocutaneous dysplasia |
| **DCD-FLNA** | Variant of filamin A missing 16 amino acids, observed in DCD |
| **DMEM** | Dulbecco's modified eagle medium |
| **DNA** | Deoxyribonucleic acid |
| **DTT** | Dithiothreitol |
| **eGFP** | Enhanced green fluorescent protein |
| **ELISA** | Enzyme-linked immunosorbent assay |
| **ERK** | Extracellular signal-regulated kinase |
| **FBSF** | Fetal bovine serum, filtered |
| **FHH1** | Familial hypocalciuric hypercalcemia type 1 |
| **FLNA** | Filamin A |
| **FLNB** | Filamin B |
| **FLNC** | Filamin C |
| **FMD1** | Frontometaphyseal dysplasia type 1 |
| **GPCR** | G protein-coupled receptor |
| **HCl** | Hydrochloric acid |
| **IDF** | Infantile digital fibromatosis |
| **iPSC** | Induced pluripotent stem cell |
| **MAPK** | Mitogen-activated protein kinase |
| **MEM** | Minimum essential medium |
| **MNS** | Melnick-Needles syndrome |

| | |
|---|---|
| **mRNA** | Messenger ribonucleic acid |
| **MSC** | Mesenchymal stem cell |
| **NEB** | New England Biolabs |
| **NSHPT** | Neonatal severe hyperparathyroidism |
| **nt** | Nucleotides |
| **OPD1** | Otopalatodigital syndrome type 1 |
| **OPD2** | Otopalatodigital syndrome type 2 |
| **OPDSD** | Otopalatodigital spectrum disorders |
| **PCR** | Polymerase chain reaction |
| **PBS** | Phosphate buffered saline |
| **PFA** | Paraformaldehyde |
| **PTH** | Parathyroid hormone |
| **p-ERK** | Phosphorylated ERK1/2 |
| **p-p38** | Phosphorylated p38 |
| **qPCR** | Quantitative polymerase chain reaction |
| **RNA** | Ribonucleic acid |
| **RNase** | Ribonuclease |
| **RT-PCR** | Reverse transcription polymerase chain reaction |
| **RTP** | RNA-to-protein |
| **SDS** | Sodium dodecyl sulfate |
| **shRNA** | Short hairpin ribonucleic acid |
| **SRE** | Serum response element |
| **TEMED** | N,N,N’,N’-Tetramethylethylenedimine |
| **TOD** | Terminal osseous dysplasia |
| **TODPD** | Terminal osseous dysplasia with pigmentary defects |

Symbols for genes are italicised while the corresponding protein products are not (e.g. *FLNA* gene vs FLNA protein). Full capital letters are used when referring to human genes (e.g. *FLNA*) while only the first letter is capitalised for mouse genes (e.g. *Flna*).

# Chapter 1: Introduction

# Chapter 1 Introduction

## 1.1 Overview

The human skeleton is a dynamic organ that is constantly being remodelled in response to cues from the external and internal environment. This occurs through the combination of bone resorption and bone deposition. Disorders of bone result when there is a dysregulation of one or both of these processes (1). By far, the most common disease of bone is age-related osteoporosis – this presents a significant health burden which is set to increase with the ageing population (2).

Studies on rare diseases of bone have provided mechanistic insights into the processes that underpin skeletal modelling and remodelling. The development of next generation sequencing technology has allowed the advancement of knowledge surrounding the genetic aetiology of these rare diseases, and functional studies on these genetic variants have elucidated key signaling pathways active in bone. Improved understanding of bone biology allows the identification of possible targets for therapeutic interventions aiming to treat both rare and common diseases of bone.

The work in this thesis focuses on a rare genetic disease affecting skeletal development, known as digitocutaneous dysplasia (DCD). While the genetic defect responsible has already been identified, the mechanisms by which this genetic variant gives rise to abnormal bone development remains elusive (3). In order to explore such mechanisms, *in vitro* cell cultures were used to study the functional consequences of this genetic defect in osteoblastic (bone building) cells, and to investigate possible signaling pathways that may be mediating these effects.

## 1.2 Digitocutaneous dysplasia (DCD)

### 1.2.1 Clinical features of DCD

Digitocutaneous dysplasia (DCD) is a genetic syndrome that exhibits abnormal skeletal development (4). It is extremely rare, and there have only been thirty-five previously reported cases from twenty-one unrelated families (3,4,13–22,5,23,6–12). It is an X-linked disorder with presumed prenatal male lethality, inferred from the absence of affected males and the reduced male:female offspring ratio in affected females (3,9).

Formerly known as terminal osseous dysplasia with pigmentary defects (TODPD) or more simply terminal osseous dysplasia (TOD), this syndrome was first recognised by Bacino et al (8) to be defined by the presence of three major features: skeletal abnormalities, digital fibromatosis, and skin defects (Figure 1.1).

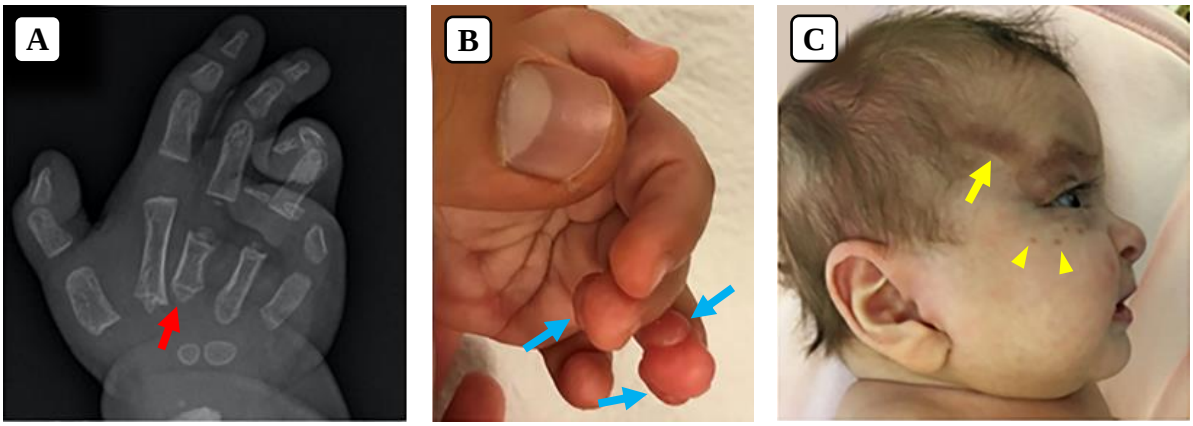


Figure 1.1: Clinical features of DCD. Triad of skeletal dysplasia, digital fibromatosis, and skin defects typical of DCD. (A) Hand radiograph showing a malformed metacarpal (red arrow). (B) Digital fibromata on the lateral aspects of the tips of the third and fourth digits (blue arrows). (C) Hyperpigmented atrophic lesion in the temporal region lateral to the eyebrow (yellow arrow) along with depressed hyperpigmented spots on the cheek (yellow arrowheads).

Images modified and reproduced with permission from Azakli et al. (23)

As the original name suggests, the ‘osseous dysplasia’ or the skeletal abnormalities are most pronounced in the ‘terminal’ or distal limbs, i.e. the hands and the feet. Clinically, this is observed as a variable combination of clinodactyly (curvature of the digits in the plane of the

palm), brachydactyly (shortening of the digits), and camptodactyly (fixed flexion deformity in the digits, usually referring to the proximal interphalangeal joint) (22,23). Although these descriptors apply to both the hands and the feet, these features are more difficult to discriminate in the feet and therefore reports are often limited to 'overlapping toes' (13,19,23). Radiologically, unusually short or underdeveloped metacarpals and metatarsals are detected and are often accompanied by hypoplasia of one or more phalanges (Figure 1.1A) (3,23). A detailed skeletal survey conducted by Brunetti-Pierri et al. (17) was able to confirm the persistence of these features into adulthood. Fusion of bones (carpal and tarsal coalitions, carpal-metacarpal or tarsal-metatarsal fusions), were also identified in this study (17). This feature was previously infrequently described in this syndrome (15) perhaps due to most radiological investigations having been done prior to the bones being fully ossified. Additionally, it was discovered that the skeletal abnormalities were more widespread than initially thought, with the presence of abnormal bony architecture (e.g. striations, amorphous ossification, lucent defects with sclerotic borders) being detected in proximal limb bones such as the humerus and the femur (17). The generalised skeletal involvement could be indicative of a more fundamental defect in the regulation of bone development.

The second key feature of DCD, the digital fibromata, are round nodules or tumours that develop on the fingers and toes. They typically appear in the first few months of life as firm, non-tender swellings on the lateral aspects of the distal ends of the fingers and toes (Figure 1.1B) (10,13,14,23). While they initially undergo a phase of rapid growth, spontaneous regression ensues soon after – usually sometime during childhood (10). Consequently, digital fibromata are absent in affected adults, although sometimes scar-like lesions on the fingertips remain, marking the areas where they used to be located (8,10). The clinical progression of the digital fibromata is remarkably similar to another condition known as infantile digital fibromatosis (IDF) (24). However, IDF is not accompanied by other congenital malformations,

and is histologically distinguished from the digital fibromata in DCD by the presence of intracytoplasmic inclusion bodies (12,24). The inclusion bodies were initially demonstrated to be absent in all digital fibromata sampled from individuals with a diagnosis of DCD (3,5,7,10,12,13,18). However, a single case of DCD was recently reported where inclusion bodies were detected in the digital fibromata (22). This might suggest that the underlying pathology is shared between these disorders. Although, unlike DCD, cases of IDF have been sporadic and no known causes have been identified – genetic or acquired (24,25).

The third key feature of DCD is the skin defects. They are depressed or atrophic, apparently hyperpigmented patches, that are usually observed on the temporal regions of the face lateral to the eyebrows (Figure 1.1C). Note that the histological evidence for increased pigmentation in these lesions has been inconsistent (10,20), and consequently dermatologists have preferred the term DCD over TODPD for this syndrome (22).

While skeletal abnormalities, digital fibromata, and skin defects are the most striking features of this syndrome, other features have also been reported, albeit variably. These include accessory gingival frenula (8,10,11,13), iris coloboma (8,10,23), dysplastic teeth (3,11,19,20), and cardiac septal defects (8,10,16,20,23).

It has been proposed that a possible contributor to the phenotypic variability is the X-linked nature of this syndrome (9). In females, random X-inactivation (a phenomena whereby dosage compensation of the X chromosome is attained) results in two populations of cells: one with most genes on the maternal X-chromosome silenced and the other with most genes on the paternal X-chromosome silenced (26). Individuals with DCD (which are all female) will exhibit the effects of the disease only in cells where the affected allele is transcriptionally active.

Interestingly, individuals with DCD have been found to show highly skewed X-inactivation patterns in peripheral blood leucocytes, with preferential inactivation (82-93%) of the

chromosome carrying the affected allele (9). However, the level of skewing in blood did not correlate with severity of the clinical phenotype, probably because this did not reflect the inactivation patterns in other tissues.

### 1.2.2 DCD is caused by a single recurrent variant in *FLNA*

The variant responsible for causing DCD is a single synonymous transition that affects the last nucleotide of exon 31 in the *FLNA* gene (NM_001110556.1:c.5217G>A) (16). To date, all cases of DCD, for which genetic analysis has been conducted, have been shown to carry this pathogenic variant in *FLNA* (3,16,18–21,23). Note that *FLNA* resides on the X chromosome and all affected individuals have been female heterozygotes. Homozygosity or hemizygosity for this variant (in females and males respectively) is presumably non-survivable as such occurrences have never been reported.

This variant was predicted to be synonymous at the protein level. However, its location at the exon-intron boundary meant that it had the potential to alter the encoded protein through the disruption of splicing (16). Splicing is an essential part of pre-mRNA processing and it involves the removal of introns and joining of adjacent exons to produce mature mRNA that can be used for translation. The 5’ splice region consists of the six nucleotides at the 5’ end of the intron and the three nucleotides at the 3’ end of the preceding exon (Figure 1.2A) (27). The appropriate sequence at the 5’ splice region is necessary for the proper recognition of the exon-intron boundary (28), and consequently variants that alter this sequence can cause abnormal splicing and result in disease (27).

However, only the first two nucleotides at the 5’ end of the intron, which make up the splice donor, are strictly conserved (with exceptions, see ref. (29)). The other nucleotides show significant variability, and this makes the interpretation of variants in this region complicated

(28). Contributing to the complexity of this issue is the influence of other factors such as splicing enhancers and silencers which are degenerate and consequently difficult to define (28). The only way to prove that a certain variant in the 5' splice region is pathogenic, is to demonstrate the presence of an aberrantly spliced transcript.

Demonstration of the mis-splicing of *FLNA* in DCD proved difficult because the affected allele was not transcriptionally active in sampled skin fibroblasts from these individuals (a consequence of the extremely skewed X-inactivation patterns) (16). However, the expression of the disease allele was detected in three fibroma samples obtained from a single individual, and it was found that this G>A variant promoted the use of a cryptic splice site positioned 5' to the original site (16). The result of this was the removal of the last forty-eight nucleotides of exon 31 during splicing of the *FLNA* pre-mRNA molecule (Figure 1.2B) (16). At the protein level, this is an in-frame deletion of sixteen amino acid residues near the middle of the encoded filamin A protein (FLNA; NP_001104026.1:p.Val1724_Thr1739del) (16). It is thought that this alters the protein structure in a way that disrupts specific functions of FLNA; however, the exact mechanisms by which this results in the DCD phenotype still remains unclear (3,16,30).

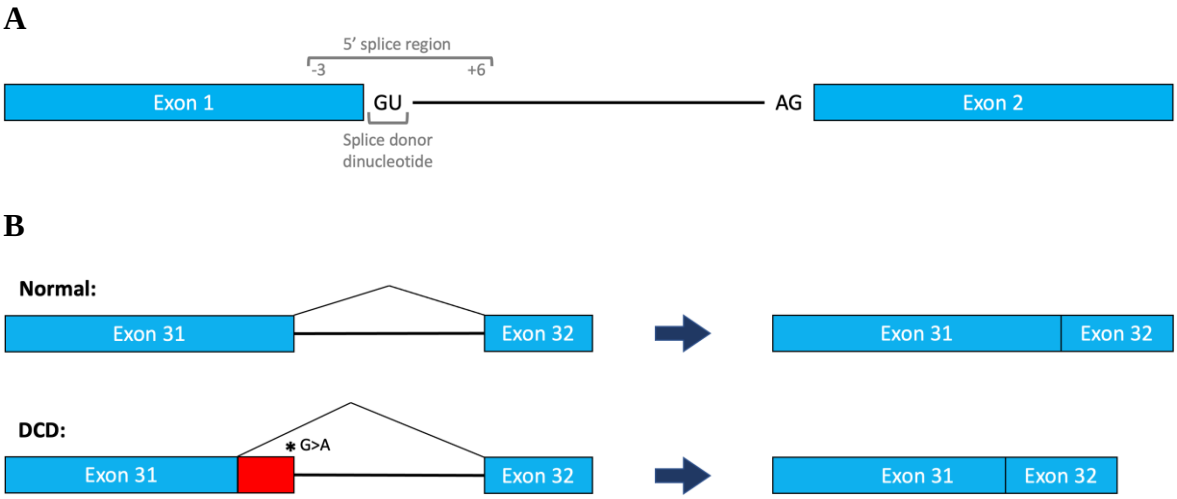


Figure 1.2: The recurrent DCD variant lies in the exonic section of the 5' splice region of *FLNA* exon 31. (A) The 5' splice region encompasses the last three nucleotides of the exon and the first six nucleotides of the following intron. The splice donor dinucleotide is the most conserved position in this region; guanine and uracil take these positions in ~99% of all 5' splice sites. (B) Normal splicing of *FLNA* involves the removal of an intron to join exon 31 and 32. The G>A transition at the last nucleotide of exon 31 results in the use of a cryptic splice site positioned 5' to the original splice site resulting in the removal of the forty-eight nucleotides at the end of exon 31 during splicing.

Figure created using Microsoft PowerPoint for Mac.

### 1.2.3 An atypical case of DCD

A case brought to our attention through personal communication (not yet published in the literature) deserves a mention here as it is highly relevant to the work that follows. A 6-month-old female was given a clinical diagnosis of DCD on the basis of multiple digital fibromata, multiple oral frenulae, and skeletal abnormalities of the hands including metacarpal hypoplasia. In addition to these features, she also developed restrictive cardiomyopathy, interstitial lung disease (with atelectasis and bronchiectasis), and tonic seizures, none of which have been previously associated with DCD. This individual subsequently died from heart failure at the age of 5.

Analysis of *FLNA* in this individual did not demonstrate the presence of the recurrent variant (NM_001110556.1:c.5217G>A) found in previously reported cases of DCD; however, a novel c.5217+5G>C variant was detected. This variant is located in the intron just five nucleotides 3'

to the recurrent variant (see Figure 1.3). The mis-splicing event identical to that previously demonstrated by Sun et al. (16) (leading to the deletion of 16 amino acids in FLNA) was detected in the cardiac tissue of this individual postmortem (but not in lung or skin, presumably due to skewed X-inactivation), thus confirming the pathogenicity of this novel variant.

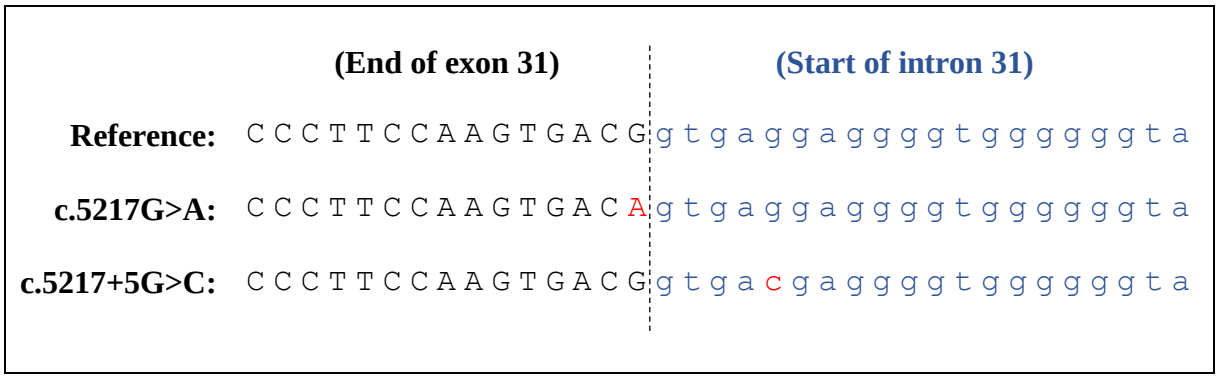


Figure 1.3: Variant responsible for the atypical case of DCD. Position of the NM_001110556.1:c.5217+5G>C variant found in the atypical case of DCD in relation to the recurrent c.5217G>A variant. Part of the sequence from the end of exon 31 (in capitals) to the start of intron 31 (in lowercase) of *FLNA* is shown. The dashed line separates the exon from the intron. The variants are indicated in red font. The reference sequence was obtained from Ensembl version 101 (31), transcript ID: ENST00000369850.10.

Figure created using Microsoft Word for Mac.

It is possible that this c.5217+5G>C variant also produces other mis-spliced transcripts to produce the phenotypic features not typical for DCD in this individual. However, this was not specifically investigated, and the method used to demonstrate mis-splicing (RT-PCR) had limited ability to detect other transcripts, and therefore this remains unclear.

## 1.3 Filamin A (FLNA)

### 1.3.1 Diseases associated with *FLNA*

Gain-of-function variants in *FLNA* have been associated with the otopalatodigital spectrum disorders (OPDSD), of which DCD is one (30). These disorders are characterised by a combination of skeletal anomalies and other congenital defects. There are five other disorders in this group: otopalatodigital syndrome type 1 and type 2 (OPD1 and OPD2), frontometaphyseal dysplasia

type 1 (FMD1), Melnick-Needles syndrome (MNS), and a more recently described syndrome of joint contractures, susceptibility to keloid formation, and cardiac valvular and optic tract defects (CKCO) (30). As with DCD, these disorders are each caused by restricted sets of variants in *FLNA* that cluster in one or several regions along this gene (30). The clustering of variants is suggestive of a pathogenesis that involves the dysregulation of specific functions residing in different regions of the encoded FLNA protein to produce these distinct, yet overlapping phenotypes.

Other conditions that have been associated with pathogenic variants in *FLNA* include: periventricular nodular heterotopia (a neuronal migration disorder) (32), X-linked congenital intestinal pseudo-obstruction (an intestinal motility disorder) (33), familial cardiac myxomatous polyvalvular dystrophy (34), and macrothrombocytopenia (35). These conditions can co-exist in the same individual, and it is thought that they are caused by variants which fall under the loss-of-function category (30). These may either involve localised loss-of-functions (e.g. affecting a single functional domain while leaving the rest of the FLNA protein intact) or through a global reduction of function (e.g. decreased abundance of the protein).

The atypical case of DCD introduced in the previous section could be a mixed phenotype (36,37), with the typical features of DCD representing a gain-of-function effect, while the interstitial lung disease (38) and the tonic seizures (possible periventricular nodular heterotopia) representing a loss-of-function effect. As suggested earlier, the novel c.5217+5G>C variant may be inducing other mis-splicing events that produce transcripts responsible for the loss-of-function effects. For example, out-of-frame transcripts that are degraded through nonsense-mediated decay could lead to a decreased abundance of FLNA protein (37).

### 1.3.2 Functions of FLNA

FLNA is a widely distributed cytoskeletal protein with diverse and complex functions in various organ systems around the body. At the cellular level, FLNA is important for cell spreading and migration (39) and the protection of cells from mechanical stress (40,41). Both of these functions are mediated by the binding of FLNA to F-actin, which allows the cross-linking and reorganisation of the actin cytoskeleton.

FLNA also is important for the localisation of other proteins within the cell (e.g. retention of transcription factors in the cytoplasm) (42), and the organisation of proteins into groups that function in a common signaling pathway (i.e. FLNA serves as a signalling scaffold) (43). These functions are mediated by the ability of FLNA to bind a wide variety of transmembrane and cytoplasmic proteins.

Although the term ‘scaffold’ might suggest an inert, stationary structure, FLNA is quite the opposite. FLNA structure can be altered by mechanical forces (44), phosphorylation (45), partner binding (46), and proteolysis (47). All of these factors contribute to the regulation of the abovementioned functions of FLNA.

### 1.3.3 Structure of FLNA

FLNA is a large, 280 kDa protein composed of an N-terminal actin-binding domain, followed by twenty-four repeating structures that are immunoglobulin-like (Ig 1-24) (48). These repeats are organised into rod domain-1 (Ig 1-15), rod domain-2 (Ig 16-23), and the C-terminal self-association domain (Ig 24) (48). Rod domain-1 and rod domain-2 are separated by a region named hinge 1, while rod domain-2 and the self-association domain are separated by hinge 2 (49,50). FLNA exists as a homodimer and forms a V-shaped structure that allows the cross-linking of the actin cytoskeleton into orthogonal networks (Figure 1.4).

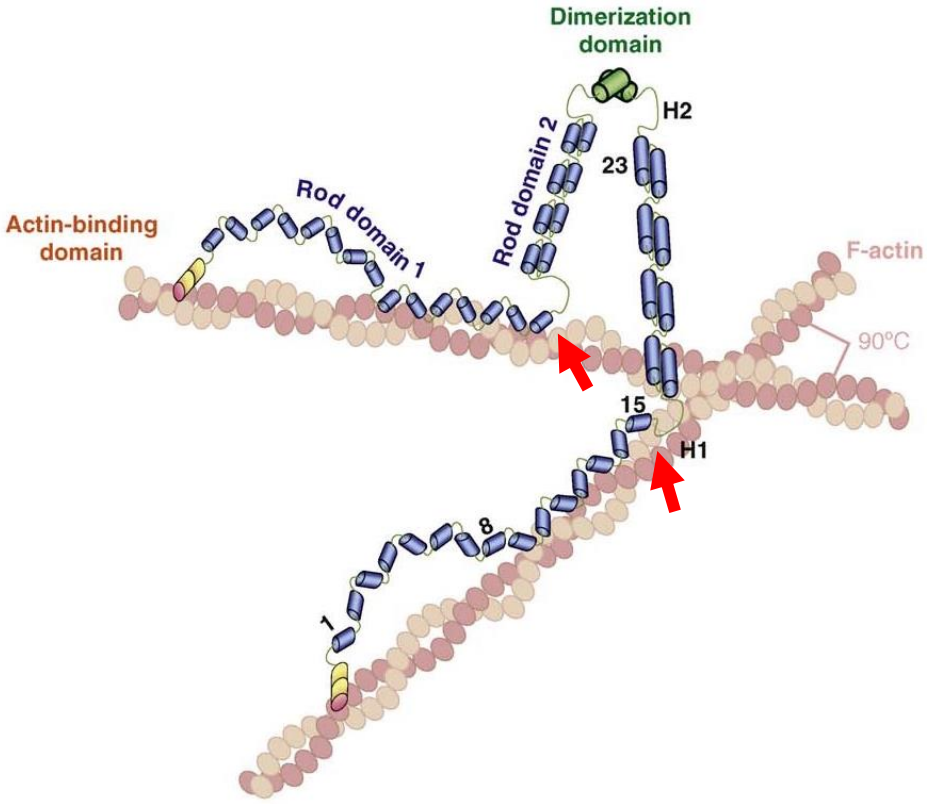


Figure 1.4: Structure of the FLNA homodimer bound to F-actin. The red arrows indicate the location of the sixteen amino acid deletion responsible for DCD. The N-terminal actin binding domain is depicted in yellow. The immunoglobulin-like repeats are shown as blue cylinders (Ig 1, Ig 8, Ig 15, and Ig 23 are numbered for orientation). Rod domain-1 and rod domain-2 are labelled, showing that they are made up of Ig 1-15 and Ig 16-23 respectively. Ig 24, in green, serves as the dimerization domain. Hinge 1 (H1) and hinge 2 (H2) are also labelled here.

Figure modified and reproduced with permission from Zhou et al. (51)

In broad terms, the region of FLNA preceding hinge 1 (i.e. actin-binding domain and rod domain-1) functions in actin-binding (52), while the region after hinge 1 (i.e. rod domain-2 and the self-association domain) is important for the scaffolding function. Pertinently, the vast majority of interactions with binding partners occur in rod domain-2 of FLNA, thus bringing components of signalling cascades into close proximity (50). Meanwhile, the two hinge regions provide flexibility, with hinge 1 in particular being important for maintaining the viscoelastic properties of the FLNA–F-actin network (53). Both hinge 1 and hinge 2 possess a calpain cleavage site (48). Such cleavage results in the release of rod domain-2 which is then transported, along with its binding partners, into the nucleus to fulfil its functions there also.

### 1.3.4 Mis-splicing of *FLNA* in DCD

As previously described in section 1.2.2, a single mis-splicing event in *FLNA* has been associated with DCD (16). This event results in the exclusion of sixteen amino acid residues from the full length protein. This in-frame deletion in Ig 15, just before hinge 1, is expected to alter the secondary structure and thus disrupt normal function of FLNA to result in the disease phenotype, although the exact mechanisms are yet unknown (3,30).

Insights from allelic conditions described in section 1.3.1 may provide clues about the pathogenesis of this disease. Firstly, the clinical similarities between DCD and other OPDSD suggest that DCD is caused by gain-of-function in FLNA rather than a loss-of-function (30). Secondly, the clustering of variants responsible for OPDSD in Ig 15 could mean that the DCD variant is affecting a region of FLNA that has an important function in normal skeletal development (Figure 1.5A). Note that the skeletal abnormalities do differ between the different conditions (e.g. prominent supraorbital ridges and skull base sclerosis are observed in FMD1 (54) but not in DCD) suggesting that the variants responsible for these conditions affect the same function of FLNA but in a different manner, to produce these distinct phenotypes.

To show the spatial relationship between the FMD variants and the DCD deletion, these have been mapped onto filamin B (FLNB) Ig 15 solution structure (PDB ID: 2DMB) (55) which is homologous to FLNA Ig 15, as no structure has yet been described for the latter (Figure 1.5B). One FMD variant is located within the region of the DCD deletion (NP_001447:p.Gly1728Cys) (56), while another lies adjacent to the beginning of the deletion (p.Cys1723Trp; Dr Emma Wade, Department of Women's and Children's Health, University of Otago, personal communication). A further two variants, also unpublished, have been found within Ig 15, and these reside on the other side of this structure (p.Gly1682Arg, p.Thr1673Pro).

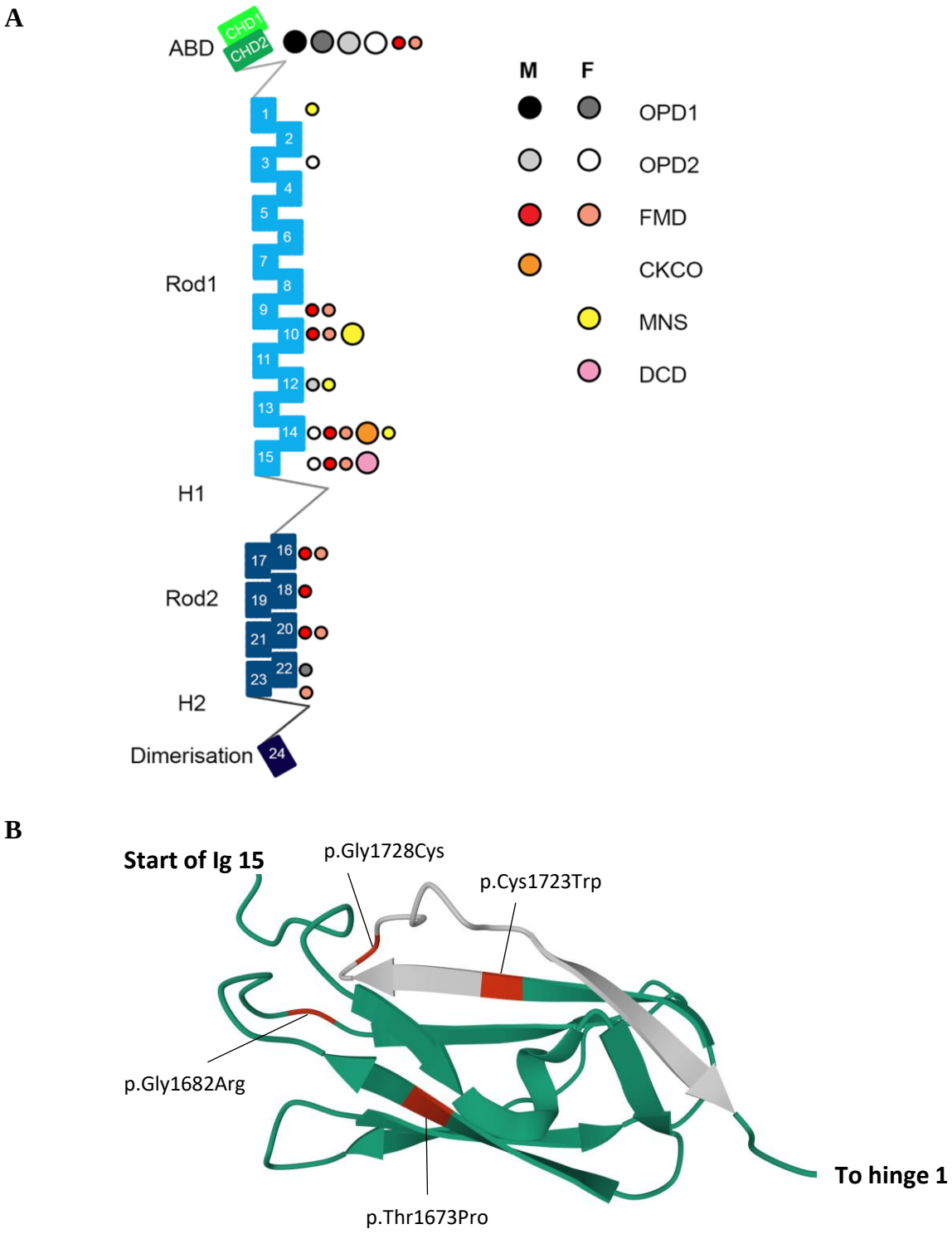


Figure 1.5: Location of variants in FLNA causative of OPDSD. (A) Variants responsible for the otopalatodigital spectrum of disorders (OPDSD) are mapped onto a diagrammatic representation of the FLNA protein. 'Hotspots' harbouring multiple variants causative of these disorders are denoted with larger symbols. Note the clustering of variants around Ig 15. (B) Structure of FLNB Ig 15 which is homologous to that of FLNA Ig 15. The sixteen amino acid deletion responsible for DCD is shown in grey, while the FMD1 variants found in this repeat are shown in red. ABD, actin binding domain; CKCO, syndrome consisting of contractures, keloid, cardiac defects and optic anomalies; DCD, digitocutaneous dysplasia; FMD, frontometaphyseal dysplasia; H1, hinge 1; H2, hinge 2; MNS, Melnick-Needles syndrome; OPD, otopalatodigital syndrome.

Figures reproduced modified with permission from Wade et al. (30) and Tomizawa et al. (55)

Interestingly, there is a variant nearby in Ig 14 that is responsible for CKCO. This condition shares many features with other disorders on the OPD spectrum including joint contractures and cardiac/valvular abnormalities (i.e. some pathogenesis is shared) but no defects in ossification are observed – suggesting that the gain-of-function effect is not active in bone tissue (30,57,58). This observation emphasises the fact that gain-of-function variants in *FLNA* have quite specific effects on the function of the encoded protein.

Clearly, the section of FLNA that is removed due to mis-splicing of *FLNA* in DCD is integral to its function since hemizygosity in males is presumed embryonic lethal (3,9). Curiously, a large deletion between Ig 14 and Ig 17 of FLNA (thus encompassing the sixteen amino acid deletion in Ig 15 observed in DCD), has been found to be responsible for a severe but male-survivable form of FMD (Dr Emma Wade, Department of Women's and Children's Health, University of Otago, personal communication). Evidently, the smaller deletion confers a more profound gain-of-function. This is perhaps through the dysregulation of the functions of FLNA that reside in Ig 14-17, which remain intact in DCD but are removed in the abovementioned case of FMD.

Such an effect could be mediated by alterations in the local secondary structure of FLNA that leads to the dysregulation of the interactions with its binding partners. To date, twenty-one different proteins have been identified to interact with FLNA between Ig 14 and Ig 17 (Table 1-1).

Table 1-1: FLNA Ig 14-17 binding partners

| Gene | Protein | Ig repeat on FLNA | References |
|---|---|---|---|
| *MRTFA* | MKL1 | 4-7, 16-21 | (59) |
| *FOXC1* | FOXC1 | 4-9, 16-21 | (60) |
| *RACK1* | RACK1 | 8-15 | (61) |
| *CFTR* | CFTR | 9, 12, 17, 19, 21, 23 | (62,63) |
| *PRNP* | Pro-Prion protein | 10, 16-18, 20, 21, 23 | (64,65) |
| *FURIN* | Furin | 13-14 | (66) |
| *CASR* | CaSR | 14-15 | (67–69) |
| *KCNMB1* | $BK_{Ca}$ $\beta_1$ subunit | 14-19 | (70) |
| *NPHP1* | Nephrocystin | 15-16 | (71) |
| *PACSIN2* | Syndapin II | 15-16, 20 | (72,73) |
| *ECSCR* | ECSM2 | 15-16, 19-21 | (74) |
| *FILIP1* | FILIP1 | 15-18 | (75) |
| *TRAF2* | TRAF2 | 15-19 | (76) |
| *CAPN1/2* | Calpain-1 and -2 | Cleavage at hinge 1 | (48,77) |
| *CMIP* | Tc-mip | 16-18 | (78) |
| *GRB7* | Grb7 | 16-19 | (79) |
| *DNM1L* | Drp1 | 16-23 | (80) |
| *RRN3* | TIF-90 | 16-24 | (81) |
| *GP1BA* | GPIba | 17 | (82) |
| *SH2B1* | Adaptor protein SH2B1 beta | 17-23 | (83) |

Although specific Ig repeats of FLNA to which they interact are indicated, these are not necessarily precise or accurate. For instance, the mapping of the binding site of syndapin II on FLNA in two different studies have given conflicting results. The earlier study identified Ig 15-16 to be the minimum region necessary for binding using a series of truncations (72), while a later study used mutually exclusive constructs to show binding of syndapin II to Ig 20 but not to an Ig 13-16 construct (73). The mapping of interactions are conducted in non-physiological settings and therefore it is not clear whether they occur *in vivo* (84). This illustrates that a combination of different techniques should be used to give confidence to these interactions.

Aside from the technical issues, the nature of FLNA also introduces some complexity into interpreting the relevance of each binding partner to the pathogenesis of DCD. Firstly, its

repetitive form with the twenty-four immunoglobulin-like structures permits several interaction partners to bind at multiple sites along FLNA. For example, CFTR has been shown to bind Ig 9, 12, 17, 19, 21, and 23 (62,63). Whether all of these are physiologically relevant, and whether binding at Ig 17 is sufficiently critical to be relevant to the pathogenesis of DCD is something that needs to be considered.

Another key consideration is the presence of two other highly homologous proteins in the human – filamin B (FLNB) and filamin C (FLNC). These proteins share the same general structure consisting of the N-terminal actin binding domain followed by twenty-four immunoglobulin-like repeats which are separated into rod domain-1 and rod domain-2 by the two hinge structures (85,86). The three filamins have also been shown to have high amino acid sequence homology (>70%) (87). The implication of this is that many interaction partners of FLNA also bind one or both of FLNB and FLNC (50). It therefore becomes a bit more difficult to determine whether each binding partner really has a functional relationship with FLNA. Note that the expression patterns of the three filamins differ (87). This can be used to rule in or rule out each filamin isoform as a functionally relevant interaction partner. Co-expression with the binding partner of interest, in one or more tissues could mean that the interaction is physiologically (or pathologically) relevant.

Of interest to this project is the interaction of FLNA with the extracellular calcium-sensing receptor (CaSR). In 2001, two independent groups identified FLNA to be a binding partner of CaSR (67,68). Both groups narrowed down the region of FLNA critical for the interaction using a series of truncation and deletion constructs. Awata et al. (68) described the critical region to be between Ig 14 to the start of Ig 17 (amino acid residues 1566-1875), while Hjalm et al. (67) reported the region to be from Ig 14 to near the end of Ig 15 (residues 1534-1719). Putting these

together, it would be reasonable to assume that the binding site lies within Ig 14-15. Hence, this interaction is a candidate for one that is affected by the mis-splicing event observed in DCD.

## 1.4 Calcium-Sensing Receptor (CaSR)

The extracellular calcium-sensing receptor (CaSR) is a G protein-coupled receptor (GPCR) that is highly expressed in the parathyroid gland and the kidney (88). Its expression has also been detected in various other organs and tissues throughout the body including bone, pancreas, intestine, lung, skin, vasculature, and brain (88). It plays a pivotal role in whole body extracellular calcium homeostasis through the control of parathyroid hormone (PTH) release from the parathyroid gland and calcium excretion through the kidneys (88). The role of CaSR in other organs is less well established; however, emerging evidence has revealed an increasingly diverse range of functions for CaSR – from the regulation of neuronal excitability to the control of fetal lung development (88–90).

### 1.4.1 Diseases associated with *CASR*

Pathogenic variants in the gene encoding CaSR have been found to cause several conditions that involve the dysregulation of extracellular calcium homeostasis. Normally, a drop in extracellular calcium concentration is detected by CaSR expressed in the parathyroid gland and this initiates the release of PTH into the bloodstream. This hormone acts to increase extracellular calcium through decreasing excretion through the kidney, increasing release from bone, and increasing absorption in the gut, thereby restoring calcium homeostasis (see ref. (88) for a review on CaSR function in extracellular calcium homeostasis).

It is therefore not surprising that loss-of-function variants in *CASR* are responsible for hypercalcaemic conditions. Germline heterozygosity for such variants causes familial

hypocalciuric hypercalcemia type 1 (FHH1) (91). This condition is characterised by mild to moderate elevations in serum calcium and magnesium, a relative hypocalciuria, and often a plasma PTH level that sits within the normal range but is considered high in the context of the hypercalcemia (88,92). These findings are often incidental as affected individuals are usually asymptomatic (92). Meanwhile, homozygosity or compound heterozygosity for loss-of-function variants in *CASR* results in a life-threatening disorder known as neonatal severe hyperparathyroidism (NSHPT) (91). Affected individuals have marked hypercalcemia, elevated plasma PTH, hypercalciuria (a consequence of the hypercalcemia), and bone demineralisation leading to pathological fractures (88,92).

In contrast, gain-of-function variants in *CASR* are responsible for hypocalcaemic conditions. Germline heterozygosity (and more rarely homozygosity (93,94)) for such variants lead to autosomal dominant hypocalcaemia type 1 (ADH1), a condition characterised by moderate hypocalcaemia accompanied by maladjusted plasma PTH and urine calcium levels (88,92,95).

Alterations in the level of *CASR* expression have been implicated in the pathogenesis of primary and secondary hyperparathyroidism, and single nucleotide polymorphisms in this gene have been linked to nephrolithiasis (96–99).

### 1.4.2 The role of CaSR in bone

Although the diseases linked to CaSR do not appear to have an impact on bone development or maintenance directly (e.g. demineralisation in NSHPT occurs as a consequence of elevated PTH), emerging studies in bone cells and animal models have provided insights into the possible roles of CaSR in bone biology.

CaSR is expressed in osteoblasts, osteocytes, osteoclasts, and chondrocytes, albeit variably in the latter two cell types depending on the stage of differentiation or maturation (100). Evidence

from studies using knockout mouse models have been difficult to interpret, in part, due to confounding from the effects of dysregulated PTH secretion. Initial CaSR null mice displayed skeletal abnormalities which were able to be rescued by the elimination of PTH (101–104). This seemed to suggest that the skeletal manifestations were mediated through the abnormal levels of PTH rather than direct effects of loss of CaSR in bone cells. Note however, that this knockout may have been incomplete due to the presence of alternative splicing, although, the functionality of this splice form lacking exon 5 in osteoblasts has not been verified (105,106). Whether the lack of skeletal phenotype in the double knockout model (*Casr*$^{-/-}$;*Pth*$^{-/-}$) truly indicates the redundancy of CaSR in bone cells is therefore uncertain. Subsequently, an osteoblast specific knockout using a different approach and targeting a different exon was developed (107). These mice exhibited profound effects on skeletal development, but mild PTH-dependent hypercalcemia was also observed (107,108). Again, the extent to which this phenotype is mediated by PTH rather than loss of CaSR in bone cells is uncertain.

A mouse model with a constitutively active CaSR targeted to mature osteoblasts has also been generated (109). Here, loss of trabecular bone was observed, which was deemed secondary to an increase in osteoclasts due to an increase in RANKL expression by osteoblasts (109). Notably, no other changes in osteoblast parameters were observed (109).

While the last mouse model suggests that the constitutive activity of CaSR has little impact on osteoblasts, evidence from *in vitro* studies suggest otherwise. Numerous studies involving the stimulation of CaSR in osteoblasts and related cells (e.g. osteosarcoma cell lines) have reported increases in osteoblast recruitment, proliferation, differentiation, and mineralisation (110–112). The discrepancies between the *in vitro* and the whole mouse studies, may well be explained by the presence of systemic factors that modulate CaSR signalling in osteoblasts.

### 1.4.3 Functional relationship between CaSR and FLNA

Since the identification of FLNA as an interaction partner of CaSR, the exploration of the functional significance of this interaction has revealed an increasingly complex relationship between these two proteins.

The initial reports describing the interaction between CaSR and FLNA demonstrated that the interaction was necessary for the CaSR-mediated increase in phosphorylation of extracellular signal-regulated protein kinase (ERK1/2; a mitogen-activated kinase (MAPK) that is involved in coordinating a diverse range of cellular processes from proliferation to differentiation to apoptosis) in response to stimulation with extracellular calcium (67,68).

The CaSR-FLNA interaction has also been shown to be necessary for extracellular calcium induced activity of the serum response element (SRE; a transcriptional regulatory element present in promoters of genes which participate in cell cycle regulation) via Gaq, RhoA, and RhoGEF lbc (113). As SRE activity has been found to be downstream of ERK1/2 (114), the above finding supports the idea that the CaSR-FLNA interaction is necessary for the CaSR-mediated activation of ERK1/2.

However, Zhang and Breitwieser (69) found that the CaSR-FLNA interaction was not essential for ERK1/2 activation stimulated by extracellular calcium, despite the presence of both CaSR and FLNA being necessary. The discrepancy between this study and the previous studies could have arisen from the differences in the methods used to disrupt the interaction. The first two studies used peptides to block the binding sites on CaSR (67) or FLNA (68), while Zhang and Breitwieser (69) utilised truncations of CaSR which were missing the binding site. However, Pi et al. (113) used a combination of the above three methods to demonstrate that the interaction was necessary for the extracellular calcium induced activation of SRE. Since the exact

truncation was not identical to that used by Zhang and Breitwieser (69) different results might be expected.

Note that the CaSR-FLNA interaction is likely to be involved in only some of the pathways initiated by CaSR stimulation. This was highlighted in the study by Rey et al. (115), which demonstrated that the interaction was necessary for the increase in intracellular calcium oscillations observed with stimulation with L-phenylalanine (another CaSR agonist), but not extracellular calcium.

Most studies investigating the interaction between FLNA and CaSR have been conducted using CaSR-transfected HEK293 cells and therefore expression levels and cellular context may not represent physiologically relevant conditions (67–69,98,113,115). Nevertheless, there have also been a few studies using cells with endogenous expression of CaSR and these support the idea that this interaction is physiologically and/or pathologically relevant. Among these, Tu et al. (116) has shown that calcium stimulation of human neonatal foreskin keratinocytes induces interactions between CaSR, RhoA, FLNA, and E-cadherin at the membrane. The CaSR-FLNA interaction was necessary for the calcium induced membrane translocation of Rho as well as E-cadherin-mediated cell-cell adhesion (116). Here, the scaffolding function of FLNA in CaSR signaling appears to be physiologically relevant in keratinocytes.

FLNA and CaSR also seem to influence the expression and/or stability of each other. In HEK293 cells transfected with CaSR, FLNA protects CaSR from degradation (69) and increases CaSR mRNA levels (98). Meanwhile, in androgen receptor-deficient prostate cancer cell lines, extracellular calcium stimulation resulted in FLNA cleavage at hinge 1, and subsequent increase in cell migration via CaSR-p115RhoGEF-calpain dependent pathway (77). Note that this was not observed in androgen-sensitive LNCaP prostate cancer cell line (77), highlighting the complexity of the relationship between CaSR and FLNA.

### 1.4.4 Possible role of CaSR-FLNA interaction in bone

Clearly, there are cell and tissue specific factors that influence the relationship between CaSR and FLNA. To date, no studies have looked into the involvement of FLNA in CaSR signaling in osteoblastic cells. The MAPK pathways activated by CaSR have the potential to induce differentiation and mineralisation in osteoblastic cells (see ref. 110 for a review). Tellingly, FMD (one of the OPDSD characterized by sclerotic skeletal dysplasia) has been shown to be also caused by variants in two genes encoding proteins that function as upstream regulators of p38 MAPK (118). These genes are *MAP3K7* and *TAB2* which encode TAK1 (transforming growth factor β-activated kinase) and TAB2 (TAK1-associated binding protein) respectively (118). There is considerable phenotypic overlap between the different forms of FMD caused by variants in *FLNA*, *MAP3K7*, and *TAB2*, which suggests that the same biochemical pathway is affected in all three forms of this condition (119). This pathway is yet to be elucidated but one plausible pathway is through CaSR-FLNA-TAK1/TAB2-p38 (Figure 1.6). CaSR stimulation in osteoblastic cells has been shown to elicit mitogenic responses via activation of p38 (120), thus such a pathway may be acting in bone and be dysregulated in OPDSD to produce the skeletal dysplasia.

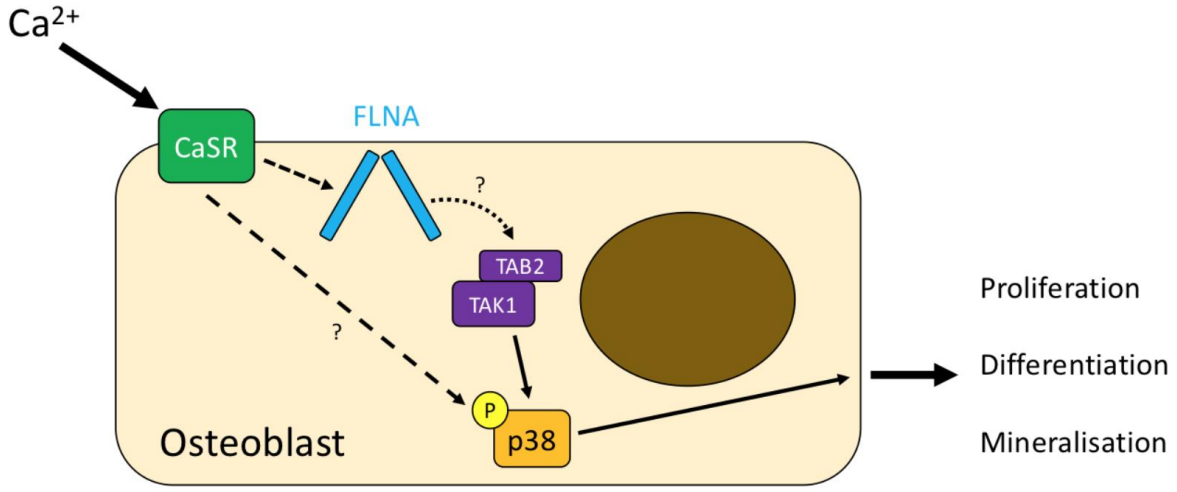


Figure 1.6: Proposed CaSR-FLNA-TAK1/TAB2-p38 pathway. Extracellular calcium can stimulate proliferation, differentiation, and mineralisation in osteoblasts via CaSR. Yamaguchi et al. (120) has shown that the mitogenic response occurs via p38 but the exact pathway is unknown (dashed arrow between CaSR and p38). The TAK1/TAB2 signalling complex is a known upstream regulator of p38, as indicated by the solid arrow. FLNA is hypothesised to be the intermediate that permits the CaSR initiated activation of the TAK1/TAB2 signalling complex (dotted arrow between FLNA and TAK1/TAB2).

Figure created using Microsoft PowerPoint for Mac.

## 1.5 Aims of study

The aim of this project was to explore the possible mechanisms by which the mis-spliced form of *FLNA* causes the skeletal dysplasia observed in DCD. Two different approaches were taken to achieve this objective.

The first approach utilised cell models in an attempt to characterise the functional consequences of this *FLNA* variant on osteoblast function. I hypothesised that this variant causes accelerated differentiation of osteoblasts and an accompanying increase in mineralisation to produce the hyperostotic phenotype. The skeletal manifestations of DCD were considered to be hyperostotic for three reasons. Firstly, DCD had been placed into the OPDSD which include other disorders that are clearly hyperostotic (e.g. FMD1 presents with progressive skull base sclerosis). Secondly, the bony fusions that develop in individuals affected with DCD suggest that inappropriate bone deposition is present. Finally, the absence of any reports of pathological

fractures in individuals affected by DCD, supports the idea that this condition is hyperostotic rather than hypoostotic.

The second approach attempted to elucidate the specific pathway that could be mediating such an effect, specifically in reference to the proposed CaSR-FLNA-TAK1/TAB2-p38 pathway. I hypothesised that the *FLNA* variant responsible for DCD would inappropriately activate the signaling pathways downstream of CaSR to promote the differentiation of osteoblasts.

The knowledge gained from this study is hoped to contribute to the advances in our understanding of bone biology. This may guide the development of treatments and management strategies that are able to achieve better outcomes for individuals affected by various diseases of bone.

# Chapter 2: Materials and Methods

# Chapter 2 Materials and Methods

## 2.1 Ethics

The work in this thesis was conducted under the approvals MEC/08/08/094 and 13/STH/56 (Health and Disability Ethics Committee, New Zealand).

## 2.2 Cell culture

### 2.2.1 Cell lines and culture conditions

The mouse calvarial pre-osteoblastic cell line MC3T3-E1 subclone 4 was cultured in MEM (Minimum Essential Medium, GlutaMAX supplement; Gibco), supplemented with 10% fetal bovine serum (FBSF; Moregate Biotech, New Zealand). Differentiation and mineralisation was induced by further supplementing the media with 50 μg/mL ascorbic acid (Sigma) and 10 mM β-glycerophosphate (Sigma).

The human immortalised cell lines U2OS (osteosarcoma) and T24 (urinary bladder transitional cell carcinoma) were cultured in DMEM (Dulbecco's Modified Eagle Medium, high glucose, pyruvate; Gibco), supplemented with 10% FBSF. Differentiation and mineralisation was induced in U2OS cultures by further supplementing the media with 50 μg/mL ascorbic acid (Sigma), 10 mM β-glycerophosphate (Sigma), and 0.02 μM dexamethasone (Sigma).

Primary human fibroblasts were cultured in DMEM (high glucose, pyruvate; Gibco) supplemented with 10% FBSF and 1% Pen-Strep (10,000 units penicillin and 10 mg streptomycin /mL; Gibco).

All cells were maintained at 37°C in a humidified atmosphere consisting of 5% $CO_2$ in air. Media was refreshed every two to three days and passaged as necessary using trypsin-EDTA

(0.25%, with phenol red; Gibco) to avoid >80-90% confluency, as determined using phase contrast microscopy.

### 2.2.2 Cell counting and cell plating

Media was removed and the adherent cells were detached by incubating in trypsin-EDTA (Gibco) for 5 minutes at 37°C. Trypsin was deactivated by adding an equal amount of media. The cells were pelleted by centrifugation at 250 rcf for 5 minutes, and supernatant discarded to remove the trypsin before resuspending in fresh media. Cell counting was conducted by loading a 20 μL sample of this cell suspension onto a haemocytometer. Cell counts were made on two grids, and the average was used to calculate the concentration of cells. The cell suspension was diluted with media accordingly for seeding 24-well or 6-well plates.

## 2.3 RNA techniques

### 2.3.1 RNA isolation

RNA was isolated from adherent cells using the NucleoSpin RNA Plus (Machery-Nagel) as per the instructions. The RNA was eluted with 30 μL of RNase-free water which was provided in the kit. The eluate was passed through the same column a second time to maximise RNA yield. RNA concentration and quality measurements were made using NanoDrop One C Spectrophotometer (Thermo Scientific). The absorbance ratio Δ260/280 of ~2.0 and Δ260/230 of ~2.0-2.2 were considered ideal values indicating pure RNA; however, samples outside this range were utilised if alternatives were unavailable. RNA isolates were stored at -20°C.

### 2.3.2 DNase treatment of RNA isolate

RNA isolates to be used for quantitative polymerase chain reaction (qPCR) were DNase treated using the TURBO DNA-free kit (Invitrogen) as per the instructions to remove any remnant genomic DNA prior to cDNA synthesis.

### 2.3.3 Synthesis of cDNA from total RNA

The primers for cDNA synthesis were first annealed to the isolated RNA by combining 10 µL of RNA isolate (15-200 ng/µL), with 1 µL of oligo dT (50 µM; ordered as primers from Sigma-Aldrich), 1 µL of random primers (100 ng/µL; Invitrogen), 1 µL of dNTPs (20 mM), and incubating at 65°C for 10 minutes. The samples were then cooled on ice before the addition of the next reaction mix: 4 µL of 5X first-strand buffer (Invitrogen), 1 µL of DTT (0.1 M; Invitrogen), 1 µL of RNase OUT (Invitrogen), 1 µL of SuperScript III Reverse Transcriptase (Invitrogen). The samples were incubated at 25°C for 5 minutes, then 50°C for 50 minutes, and finally 70°C for 15 minutes, before being stored in the fridge at 4°C. For each batch of cDNA, a -RT sample (containing a combination of RNA isolates) was run alongside the other samples without the addition of the reverse transcriptase in order to assess for any contamination with DNA.

## 2.4 Quantitative PCR (qPCR)

### 2.4.1 qPCR reaction set up

All primers used for qPCR were already available in the laboratory, and primer efficiencies had already been calculated for all except the mouse filamin A (*Flna*) primer pair. Primer sequences and amplification efficiencies are listed in Appendix A.

To calculate the primer efficiencies for the *Flna* primer pair, standard curves were generated using five serial dilutions of cDNA from MC3T3-E1: from 5 ng/µL to 0.008 ng/µL. Each 20 µL reaction contained 10 µL of LightCycler 480 SYBR Green I Master mix (Roche), 1 µL forward primer (3 µM), 1 µL reverse primer (3 µM), 3 µL of $H_2O$ (PCR grade, provided with the master mix), and 5 µL of cDNA (1 ng/µL; or 5 ng/µL to 0.008 ng/µL for the standard curve). Each reaction was set up in technical duplicates to account for pipetting errors. The cycling conditions used on the LightCycler 480 Instrument II (Roche) are indicated in Table 2-1.

Table 2-1: Cycling conditions for qPCR

| **Step** | | **Temperature** | **Duration** |
|---|---|---|---|
| Initial denaturation | | 95°C | 5 minutes |
| 45 cycles of: | Denaturation | 95°C | 10 seconds |
| | Annealing | 60°C | 10 seconds |
| | Extension | 72°C | 10 seconds |
| Melting curve | | 72 – 95°C | Heat at 0.11°C/second |

### 2.4.2 Analysis of qPCR data

Several quality control measures were taken to ensure the validity of results obtained. Firstly, the -RT and no template negative controls were run alongside the samples of interest and checked for any amplification to exclude possible contamination. Secondly, melt curve genotyping was conducted using the LightCycler 480 software version 1.5.1.62 (121). Samples were only accepted for downstream analysis if only a single curve was present because additional curves would indicate the presence of off-target amplification. Technical duplicates with cycle quantification (Cq) values which differed by greater than 0.5 were also excluded from analysis.

Cycle quantification values from the LightCycler 480 software was imported into qbase+ software, version 2.1 (Biogazelle, Zwijnaarde, Belgium - http://www.qbaseplus.com) for

analysis. Primer pair specific amplification efficiencies (Appendix A) which were calculated using standard curves on LightCycler 480 software, were imputed into qbase+ to be incorporated into the calculations.

The samples were normalised using housekeeping genes to control for any differences in the total amount of template initially added to the reaction. Three housekeeping genes (*Gapdh, Ppia, Rps29*) were run for the experiments involving the differentiation of MC3T3-E1, while just *Gapdh* was run for obtaining the preliminary result for shRNA-mediated knockdown of *Flna*. When three housekeeping genes (i.e. reference targets) were run, reference target stabilities were checked in qbase+; a geNorm expression stability value (M) of < 0.5 and a coefficient of variation (CV) of < 0.2 was considered acceptable. If one housekeeping gene deviated from the above parameters, it was removed and normalisation was conducted using the remaining two.

Relative expression levels of the genes of interest (*Sp7, Runx2, Col1a1, Flna*) were exported into Microsoft Excel for statistical analysis, detailed in the next section.

## 2.5 Statistical analysis of quantitative data

Quantitative data obtained from qPCR (section 2.4) or western blotting (section 2.13.2) were imported into Microsoft Excel for statistical analysis. Each experiment had technical duplicates for which the mean was calculated. Data from three independent repeat experiments were combined by scaling and normalising to the baseline (i.e. day 0 of differentiation or vehicle treated T24 cells). P-values were calculated using a two-tailed, unpaired t-test. Critical P-values for the Western blotting experiments were Bonferroni corrected for multiple testing as two different conditions (i.e. calcium and strontium treatments) were being tested. Graphs were

drawn using Microsoft Excel for Mac, version 16.16.27, and the error bars represent the standard error of the means.

## 2.6 Phylogenetic analysis of *FLNA* sequence

The search for species in which the last nucleotide of the exon corresponding to exon 31 of human *FLNA* (NM_001110556.1) is not conserved, was conducted using the UCSC genome browser (122) conservation track showing Multiz alignment from 100 vertebrate species – available from: https://genome.ucsc.edu/cgi-bin/hgTrackUi?db=hg19&g=cons100way.

Sequences from human and the identified rodent species were downloaded from Ensembl version 101 (31) and aligned using the MUSCLE algorithm (123) on MEGA X (124) for further inspection. Transcript IDs can be found in Appendix B.

## 2.7 Alizarin Red S staining for calcium deposits

### 2.7.1 Fixing of cells

Media was removed from the wells (24-well plates) and the adherent cells were washed by adding 0.5 mL of phosphate buffered saline (PBS; Oxoid) and swirling for a few seconds before draining. Fixing was then achieved by incubating in 0.5 mL of 4% paraformaldehyde (PFA; Sigma) in PBS for 10 minutes at room temperature. The PFA was subsequently drained and three more washes with PBS were performed. A final 0.5 mL of PBS was added for storage at 4°C.

### 2.7.2 Alizarin Red S staining

The cells fixed with PFA were drained of PBS and then incubated with 0.5 mL of 1% Alizarin Red S (Sigma) for 20 minutes at room temperature. The wells underwent four washes with PBS to remove any non-specific staining before being air dried for 10 minutes at room temperature. Staining was inspected with the naked eye and also microscopically using the Olympus IX71 inverted microscope under bright field with the Olympus TH4-200 halogen light.

## 2.8 Antisense oligonucleotide (AON) transfections

### 2.8.1 AON design

Guidelines for antisense oligonucleotide (AON) design as described by Aartsma-Rus (125) were taken into account when designing the following AONs. The secondary structure of the region of interest was evaluated using RNAfold (http://rna.tbi.univie.ac.at/cgi-bin/RNAWebSuite/RNAfold.cgi) (126). The locations of predicted exonic splicing enhancers were determined by Human Splicing Finder (http://www.umd.be/HSF/) (127). Calculation of the free energy of the AONs, AON-AON complexes, and the binding energy of the AON and its target sequence, was carried out on RNAstructure (http://rna.urmc.rochester.edu/RNAstructureWeb/) (128).

AON sequences are shown in Table 2-2 below. All were made with 2'-O-methyl RNA phosphorothioate modified bases. Scramble AON was already available in the laboratory, and were ordered from TriLink BioTechnologies. The new AONs were ordered dry with desalt-only purification from Sigma-Aldrich.

Table 2-2: AON sequences

| Name | Sequence |
|---|---|
| mAON 1 | AUCCUUGGCCUCUUCUCACU |
| mAON 2 | CACCCAUCCUUGGCCUCUUC |
| hAON 1 | ACCCCCCACCCCUCCUCACC |
| hAON 2 | GACCUACCCCCCACCCCUCC |
| Scramble | CCUCUUACCUCAGUUACAAUUUAUA |

### 2.8.2 AON transfection

AONs were resuspended in Milli-Q purified water. A 10 μM working solution was made and stored at -20 °C. Transfections mixes were made by combining 50 μL of Opti-MEM (Gibco) containing 1-20 μL of AON (10 μM working solution), with another 50 μL of Opti-MEM containing 2 μL of Lipofectamine 2000 (Invitrogen) for each well to be transfected. Mixes were incubated for at least 5 minutes at room temperature to allow the lipid-RNA complexes to form.

Cells were seeded in 24-well plates at a density of 1 x $10^5$ cells/well in 0.5 mL media and allowed to adhere for 24 hours. The media was refreshed prior to the addition of the 100 μL transfection mixes. Transfected cells were incubated at 37°C in 5% $CO_2$ for 24 hours, then cell lysates were harvested for RNA as described in section 2.3.1. The RNA isolate was used for cDNA synthesis (section 2.3.3) for subsequent reverse transcription polymerase chain reaction (RT-PCR; detailed in section 2.9) to identify transcripts representing alternative splicing events.

## 2.9 Polymerase chain reaction (PCR)

### 2.9.1 RT-PCR primer design

Primers for reverse transcription polymerase chain reaction (RT-PCR) were designed to flank exon-exon junctions so that it was possible to distinguish between amplification from cDNA and genomic DNA. Primer3web version 4.1.0 (http://primer3.ut.ee) was used to select the following optimal parameters: length of 20 bases, $T_m$ of 60°C, and product size of 150-350. Complementarity and specificity were checked using the UCSC In-Silico PCR tool (https://genome.ucsc.edu/cgi-bin/hgPcr). All primers were ordered dry from Sigma-Aldrich with desalt-only purification. These were rehydrated with Milli-Q purified water to make 100 μM stock solutions which were subsequently stored at -20°C. From these 100 μM stock solutions, 10 μM working solutions were made by further dilution with Milli-Q purified water and these were stored at 4°C. See Appendix C for RT-PCR primer sequences, product sizes, and optimised cycling conditions for each primer pair.

### 2.9.2 PCR reaction

PCR reactions were carried out by combining 0.8 μL of cDNA (as prepared in 2.3.3 and diluted to 10-20 ng/μL) with 0.8 μL each of the forward and reverse primers (10 μM as prepared in 2.9.1), 1 μL of GeneAmp 10X PCR Gold Buffer (Applied Biosystems), 0.6 μL of 25 mM $MgCl_2$ solution (Applied Biosystems), 0.1 μL of dNTPs (20 mM solution), 0.05 μL of AmpliTaq Gold DNA Polymerase (Applied Biosystems) and 5.85 μL of Milli-Q purified water. A blank was run without the addition of cDNA to serve as a negative control. See Table 2-3 and Table 2-4 for cycling temperatures for the standard and touchdown programs respectively. Some primers required the addition of 2 μL of combined enhancer solution (2.7 M betaine [Sigma], 20 nM DTT [Sigma], 55 ng/mL bovine serum albumin [Sigma], 6.7% dimethyl

sulfoxide [Sigma], in Milli-Q purified water) which replaced 2 μL of the Milli-Q purified water from the 10 μL PCR reaction mixture.

Table 2-3: Standard thermal cycling conditions for PCR

| **Step** | | **Temperature** | **Duration** |
|---|---|---|---|
| Initial denaturation | | 94°C | 10 minutes |
| 35 cycles of: | Denaturation | 95°C | 1 minute |
| | Annealing | 65°C | 1 minute |
| | Extension | 72°C | 1 minute |
| Final extension | | 72°C | 10 minutes |
| Hold | | 10°C | Until transferred to 4°C storage |

Table 2-4: Touchdown program thermal cycling conditions for PCR

| **Step** | | **Temperature** | **Duration** |
|---|---|---|---|
| Initial denaturation | | 94°C | 10 minutes |
| 3 cycles of: | Denaturation | 94°C | 30 seconds |
| | Annealing | 65°C | 30 seconds |
| | Extension | 72°C | 1 minute |
| 3 cycles of: | Denaturation | 94°C | 30 seconds |
| | Annealing | 62°C | 30 seconds |
| | Extension | 72°C | 1 minute |
| 3 cycles of: | Denaturation | 94°C | 30 seconds |
| | Annealing | 59°C | 30 seconds |
| | Extension | 72°C | 1 minute |
| 36 cycles of: | Denaturation | 94°C | 30 seconds |
| | Annealing | 56°C | 30 seconds |
| | Extension | 72°C | 1 minute |
| Final extension | | 72°C | 10 minutes |
| Hold | | 10°C | Until transferred to 4°C storage |

### 2.9.3 Gel electrophoresis

PCR products were visualised and product sizes estimated using gel electrophoresis. A 1-2% gel was made by dissolving 1-2 g of agarose (HydraGene) in 100 mL of TBE buffer solution

(1.08 g/L UltraPure Tris Buffer [Invitrogen], 0.55 g/L boric acid [LabServ, ThermoFisher], 0.093 g/L EDTA [Sigma], in 100 mL distilled water). 3 μL of PCR product was combined with 1.5 μL of SYBR Green I Nucleic Acid Gel Stain (1:2000 dilution; Invitrogen) and run at 96 V for 15-60 minutes alongside 0.5 μL of 100 bp or 1 kb ladder (New England Biolabs; NEB) also combined with 1.5 μL of SYBR. Gels were imaged under UV light using FireReader V4 (UVITEC, Cambridge, UK).

## 2.10 Sanger sequencing

### 2.10.1 Pre-sequencing reaction for clean-up of PCR products

PCR products were prepared for Sanger sequencing by removing residual dNTPs and primers through the following pre-sequencing reaction: 4 μL of PCR product was combined with 2 μL of shrimp alkaline phosphatase (E70092, Cytiva), 0.6 μL of exonuclease I (NEB), 7.5 μL Milli-Q purified water. This mixture was incubated at 37°C for 15 minutes, then at 80°C for 20 minutes, and then held at 10°C until used for the BigDye Terminator reaction or transferred to storage at 4°C.

### 2.10.2 Sequencing reaction (BigDye Terminator)

For the sequencing of PCR amplified products, 7 μL of the pre-sequencing reaction (described in 2.10.1) was combined with 2 μL of BigDye Terminator v3.1 Ready Reaction Mix (Applied Biosystems), 1 μL of BigDye Sequencing Buffer (Applied Biosystems), and 0.64 μL of the relevant forward or reverse primer (10 μM working solution).

For the sequencing of plasmids, 1 μL of extracted plasmid (preparation described in 2.11.3) was combined with 2 μL of BigDye Terminator v3.1 Ready Reaction Mix, 1 μL of BigDye

Sequencing Buffer, 5 μL of Milli-Q purified water, and 1 μL of the relevant forward or reverse primer (10 μM working solution). Table 2-5 shows the thermal cycling conditions.

Table 2-5: BigDye Terminator thermal cycling conditions

| **Step** | | **Temperature** | **Duration** |
|---|---|---|---|
| Initial denaturation | | 96°C | 1 minute 15 seconds |
| 25 cycles of: | Denaturation | 96°C | 45 seconds |
| | Annealing | 50°C | 45 seconds |
| | Extension | 60°C | 3 minutes 30 seconds |
| Hold | | 10°C | Until transferred to 4°C storage |

### 2.10.3 Clean-up of sequencing reaction

Unincorporated dideoxynucleotide triphosphates (ddNTPs) were removed from products of the BigDye Terminator reaction by ethanol precipitation of the sequencing products. 2 μL of 3 M sodium acetate (Sigma), 10 μL of Milli-Q purified water, and 50 μL of 96% ethanol (Lab Supply) was added to 10 μL of the sequencing product. This mixture was incubated at room temperature for 15 minutes and subsequently centrifuged at 3220 rcf for 20 minutes. Supernatant was removed and the pellet was washed with ethanol by adding 150 μL of 70% ethanol and centrifuging at 3220 rcf for 10 minutes. The ethanol wash was repeated once more. The supernatant was removed and the pellet left to air dry at room temperature for approximately 40 minutes.

### 2.10.4 Sequencing service

The ethanol precipitated sequencing products were submitted to Genetic Analysis Services, University of Otago, for capillary sequencing using the 3730xl DNA Analyzer (Applied Biosystems).

### 2.10.5 Sequence analysis

Sequencing results were received as .abi files and electropherograms were visualised and analysed using the Sequencher software version 5.4 (Gene Codes Corporation, USA).

## 2.11 Cloning techniques

### 2.11.1 Ligation, transformation, and culture with the pGEM-T vector

PCR products were inserted into the pGEM-T vector (Promega) with the following reaction: 1-3 µL of PCR product was combined with 5 µL of 2X Rapid Ligation Buffer (Promega), 1 µL of pGEM-T vector (Promega), 1 µL of T4 DNA Ligase (Promega), and 0-2 µL Milli-Q purified water. The reaction mixture was incubated at room temperature for 1 hour. Transformation of 100 µL of chemically competent *E. coli* was carried out by adding 5 µL of the ligation mix and incubating at room temperature for 1 hour. Following this, 100 µL of the transformation culture was spread on agar plates containing carbenicillin (100 µg/mL; Sigma) and incubated at 37°C overnight. Agar plates showing colonies were subsequently stored at 4°C.

### 2.11.2 Lysogeny broth culture

Lysogeny broth (LB) for bacterial culture was prepared by dissolving two LB medium capsules (3002-041, MP Biomedicals), 2.4 g of bacteriological peptone (Oxoid), and 1.2 g of BD Bacto yeast extract (BD biosciences) in 320 mL of distilled water. This solution was sterilised in an autoclave at 121°C for 30 minutes and subsequently stored at room temperature.

Colonies were picked from agar plates using autoclave-sterilised toothpicks and inoculated into 3 mL LB for small plasmid preparation (minipreps) or 100 mL LB for large plasmid preparations (midipreps). For plasmids with ampicillin selection (pGEM-T plasmid),

carbenicillin (Sigma) was added immediately to a final concentration of 100 μg/mL. For plasmids with kanamycin selection (dual expression plasmid), inoculated cultures were incubated at 37°C with agitation for one hour prior to the addition of kanamycin (Sigma) for a final concentration of 50 μg/mL. Cultures were incubated at 37°C with agitation and grown to saturation (typically overnight).

The cultures were then centrifuged at 3220 rcf for 20 minutes. The supernatant was discarded, and the pelleted *E. coli* were stored at 4°C.

### 2.11.3 Plasmid DNA purification

Plasmid DNA purification was carried out using the NucleoSpin Plasmid kit (Machery- Nagel) or NucleoBond Xtra Midi (Machery-Nagel) according to the provided protocols, for mini- and midipreps respectively. For the midipreps, precipitated DNA was resuspended in 400 μL of Milli-Q purified water and left to dissolve thoroughly overnight at 4°C before quantification to obtain an accurate measurement. The quality and quantity of the purified plasmid was verified using the NanoDrop One C Spectrophotometer (Thermo Scientific).

## 2.12 Construction of the shRNA-eGFP expression plasmid

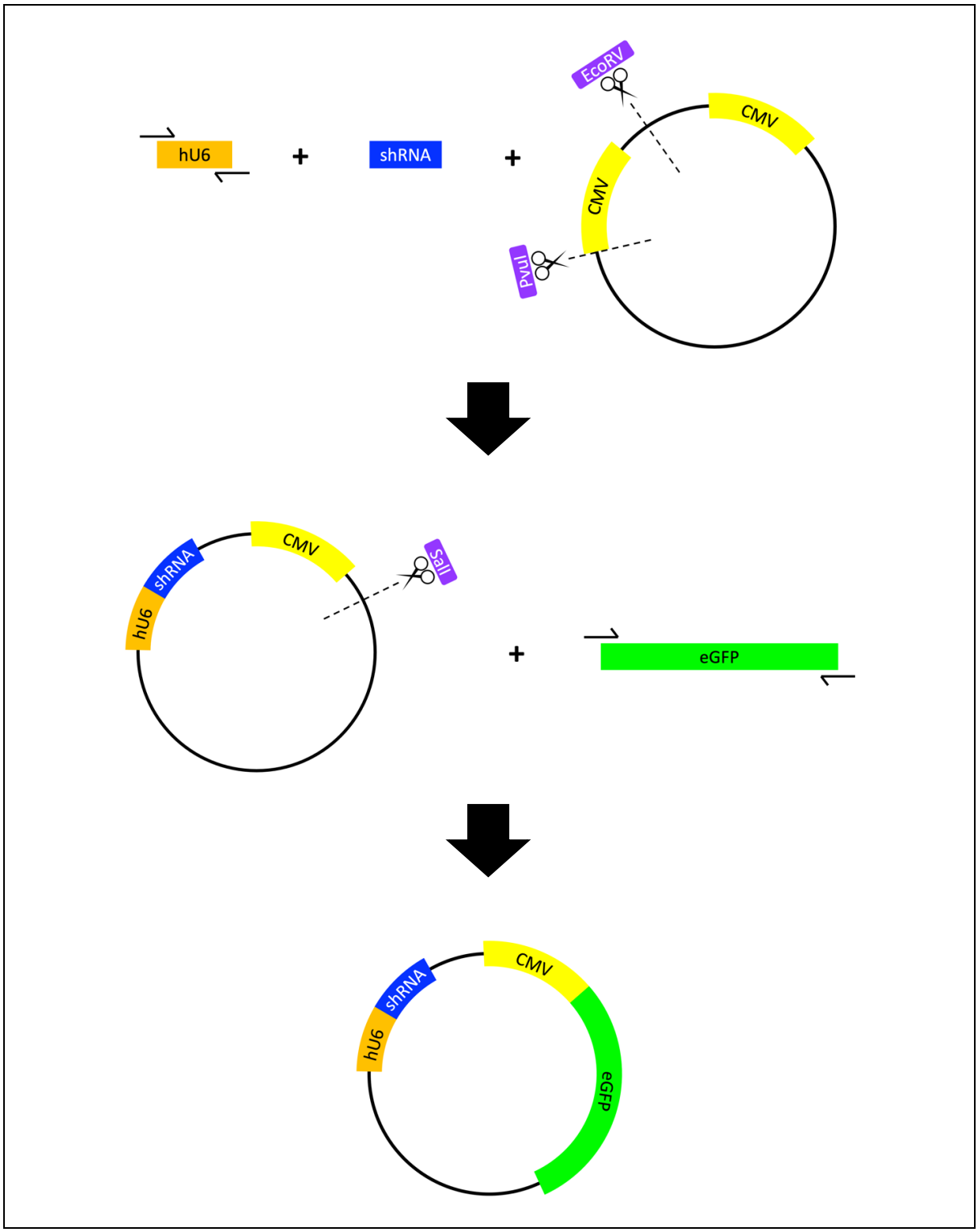


Figure 2.1: Construction of the shRNA-eGFP dual expression plasmid. hU6 promotor and eGFP fragments were produced by PCR amplification (forward and reverse arrows). Restriction enzymes are indicated in purple above scissor symbols. CMV, cytomegalovirus mammalian expression promoter; eGFP, enhanced green fluorescent protein; shRNA, short hairpin RNA.

Figure created using Microsoft PowerPoint for Mac.

### 2.12.1 Digestion of the vector

PSF-CMV-CMV-SBFI dual CMV expression plasmid provided the backbone for the production of the shRNA-eGFP construct. The original vector which had already been digested with PvuI and EcoRV restriction enzymes, was available in the laboratory.

Subsequent digestion of the plasmid in which the hU6 promotor and shRNA sequences had been added, was conducted using SalI restriction enzyme. For the digestion reaction, 1 μg of plasmid was combined with 5 μL of 10X CutSmart Buffer (NEB) and 20 units (1 μL) of SalI-HF (NEB), and made up to a final volume of 50 μL with Milli-Q purified water. This mixture was incubated at 37°C for 1 hour, then subsequently stored at 4°C.

### 2.12.2 Design and production of shRNA fragments

The sequence for shRNA1 which targets the 3'UTR of mouse *Flna* was obtained from the Sigma-Aldrich website under the clone ID: NM_010227.2-8049s21c1. The sequence for shRNA2, which targets the 5'UTR of mouse *Flna* was designed using BLOCK-iT RNAi Designer (available at: https://rnaidesigner.thermofisher.com/rnaiexpress/). The accession number NM_010227.3 was used to search for targets in the 5'UTR using the default settings. The highest ranking sequence was chosen. The sequences of shRNA1 and shRNA2 are shown in Table 2-6 along with shRNA consisting of scramble sequence (shRNAscr) that had previously been incorporated into the dual expression plasmid by another member of the lab.

Table 2-6: Sequences of shRNA1, shRNA2, and shRNAscr

| Name | Sequence |
|---|---|
| **shRNA1** | CCGGCTAGAAGCTCCCATGGCAATGCTCGAGCATTGCCATGGGAGCTTCTAGTTTTTG |
| **shRNA2** | CACCGCCTACTGCTTTAATTAAAGGCGAACCTTTAATTAAAGCAGTAGGCTTTT |
| **shRNAscr** | GGGGGUCGAUCAACUGCGACUUAGCGCCUGACCCACGCTAAGTCGCAGTTGATCGACTTTTT |

Overhang sequences were added to the 5' and 3' ends of shRNA1 and shRNA2 to facilitate HiFi assembly. The 5' overhang consisted of the final twenty nucleotides of the hU6 promoter sequence, while the 3' overhang consisted of the first twenty nucleotides following the EcoRV cut site in the PSF-CMV-CMV-SBFI vector. The forward and reverse strands of the complete sequence for shRNA1 and shRNA2 with the overhangs were ordered as oligos from Sigma-Aldrich, in a dry format with desalt-only purification. Sequences of these oligos are listed in Appendix D. These were resuspended to 100 μM with Milli-Q purified water and stored at -20°C.

The forward and reverse oligos for each shRNA were annealed to produce double stranded fragments. An annealing buffer composed of 10 mM UltraPure Tris Buffer (Invitrogen) and 50 mM NaCl (Merck) in distilled water was adjusted to pH 7.5 by the addition of HCl (ACS reagent 37%; Sigma). The oligos were added to the annealing buffer to a final concentration of 1 pmol/μL. This solution was heated to 95°C for 5 minutes, then incubated at 92°C for 2 minutes, 89°C for 2 minutes, and so on (drop 3°C every 2 minutes), until 23°C was reached, after which it was stored at 4°C.

### 2.12.3 Q5 PCR amplification of hU6 and eGFP fragments

Primers to amplify hU6 promotor and eGFP (enhanced green fluorescent protein) sequences were available in the laboratory. However, the reverse primer for amplifying hU6 needed to be ordered new so that overhangs matching the first twenty bases of shRNA1 and shRNA2 could be added to facilitate HiFi assembly. These primers were ordered from Sigma-Aldrich in a dry format with desalt-only purification.

Q5 High-Fidelity DNA polymerase (NEB) was used for PCR amplification of the hU6 and eGFP fragments. Reactions were made to a final volume of 10 μL according to the

accompanying protocol, with 1 ng of plasmid DNA (another shRNA-eGFP plasmid available in the laboratory) serving as the template for both the hU6 and eGFP fragments. A touchdown program was utilised for this reaction (Table 2-7). The primers used for the PCR reactions are listed in Appendix D.

Table 2-7: Touchdown thermal cycling conditions for Q5 PCR

| **Step** | | **Temperature** | **Duration** |
|---|---|---|---|
| Initial denaturation | | 98°C | 30 seconds |
| 3 cycles of: | Denaturation | 98°C | 10 seconds |
| | Annealing | 65°C | 30 seconds |
| | Extension | 72°C | 15 seconds |
| 3 cycles of: | Denaturation | 98°C | 10 seconds |
| | Annealing | 62°C | 30 seconds |
| | Extension | 72°C | 15 seconds |
| 3 cycles of: | Denaturation | 98°C | 10 seconds |
| | Annealing | 59°C | 30 seconds |
| | Extension | 72°C | 15 seconds |
| 36 cycles of: | Denaturation | 98°C | 10 seconds |
| | Annealing | 56°C | 30 seconds |
| | Extension | 72°C | 15 seconds |
| Hold | | 10°C | Until transferred to 4°C storage |

PCR products were visualised using gel electrophoresis, as described in section 2.9.3. 1 μL of PCR product was combined with 1 μL of SYBR and run alongside 1 μL of 100 bp ladder (NEB) also combined with 1 μL of SYBR. Gels were checked to confirm the presence of a band of the appropriate size and the absence of extra bands that would indicate the presence of off-target amplification. PCR products were quantified by measuring the intensity of the band compared to the 100 bp ladder using the ImageJ software, version 1.53a (129).

### 2.12.4 HiFi assembly of plasmids

NEBuilder HiFi DNA Assembly (NEB) was used according to the accompanying protocol to assemble the DNA fragments with the cut vector. Initially a vector:insert ratio of 1:5 was used as suggested by the protocol but this yielded no colonies and subsequently higher concentrations of insert (hU6, shRNA, eGFP) were trialled and found to achieve more efficient assembly. Table 2-8 shows the amounts of vector and insert used for a 5 μL assembly reaction. Reactions mixes were incubated at 50°C for 1 hour, and subsequently stored at -20°C or used immediately for transformation of chemically competent *E. coli* as described in section 2.11.1. Transformed cells were grown overnight on agar plates containing kanamycin at 50 μg/mL.

Table 2-8: Amounts of vector and insert added to a 5 μL assembly reaction

| | **shRNA1** | **shRNA2** | | **shRNA-eGFP** |
|---|---|---|---|---|
| **pSF.CMV.CMV.sbfI digested with PvuI and EcoRV (Vector)** | 0.009 pmol | 0.009 pmol | **pSF.hU6-shRNA.CMV.sbfI digested with SalI (Vector)** | 0.007 pmol |
| **hU6 (PCR)** | 1.362 pmol | 1.385 pmol | **eGFP (PCR)** | 0.209 pmol |
| **shRNA (Annealed)** | 0.500 pmol | 0.500 pmol | | |

### 2.12.5 Colony PCR

Colony PCR was used to identify transformants with the correctly assembled plasmid. Initially, four colonies were picked using autoclave-sterilised toothpicks to add into PCR reaction mixes, made as described in section 2.9.2. Reactions were carried out using the standard cycling conditions as described in Table 2-3. Primers used for this purpose were available in the laboratory and are listed in Appendix D.

PCR products were run on a gel (section 2.9.3), and product sizes were used to determine whether the plasmid had assembled correctly. If none of the colonies picked were deemed to

have the correct plasmid, then further colonies were picked for colony PCR. If this did not yield any positive colonies, then optimisation of the assembly step was conducted.

Colonies which were positive for correct insert on colony PCR, were then grown in LB culture for plasmid DNA purification (miniprep; section 2.11.2 and 2.11.3). These plasmids were sequenced (section 2.10) to verify correct assembly and absence of any unwanted mutations. Primers used for sequencing the plasmids were available in the laboratory and are listed in Appendix D.

Plasmids with the correct sequence were reproduced at a larger quantity by first transforming chemically competent *E. coli* with the miniprep and growing them overnight on kanamycin selective agar. A single colony was picked to be inoculated into a 100 mL of LB culture containing kanamycin, to be grown to saturation for subsequent plasmid purification (midiprep; section 2.11.2 and 2.11.3).

### 2.12.6 Plasmid transfections

Initially forward transfections were trialled. MC3T3-E1 cells were seeded in 24-well plates at a density of 5 x $10^4$ cells/well in 0.5 mL media and allowed to adhere for 24 hours. The media in each well was refreshed prior to the addition of transfection mixes containing 400 ng of plasmid DNA in 50 µL of Opti-MEM (Gibco) combined with 2 µL of Lipofectamine 2000 (Invitrogen) in 50 µL of Opti-MEM.

Transfected cells were incubated at 37°C in 5% $CO_2$ and transfection efficiency was monitored at 24, 48, and 72 hours using the Olympus IX71 inverted microscope under fluorescence (green filter) with the X-cite series 120Q (Lumen Dynamics) and bright field with Olympus TH4-200 halogen light. Photographs were taken using the Olympus DP71 camera and the cellSens software version 2.3 (Olympus).

Subsequently, a modified reverse transfection procedure was adopted. MC3T3-E1 cells were seeded into 24-well plates at confluence (~1.5 x $10^5$ cells/well) in 0.5 mL media and transfection mixes immediately added. Transfected cells were incubated at 37°C in 5% $CO_2$ for five to six hours before being subcultured into four wells to allow room for growth. The subculturing process involved the removal of media then the addition of 100 µL of Trypsin-EDTA (0.25%, with phenol red; Gibco) to detach the cells. Once the cells had detached (after ~5 mins), the trypsin was neutralised with the addition of 1.9 mL of media. Cells were mixed into this volume by pipetting and this cell suspension was distributed to four wells, each with 0.5 mL. Transfection efficiency was monitored as described above, at 24, 48, and 72 hours post the transfection procedure.

Experiments which yielded transfection efficiencies of >30% were lysed for RNA and subsequent qPCR to determine mRNA levels of *Flna* as described in section 2.3 and 2.4.

## 2.13 CaSR stimulation and measurement of MAPK activation

### 2.13.1 Calcium and strontium treatment of T24 cells

1 M $CaCl_2$ and $SrCl_2$ stock solutions were made by dissolving calcium chloride (dihydrate, ACS; BDH, United Arab Emirates) and strontium chloride (anhydrous; Sigma) respectively in Milli-Q purified water. This was added to media (DMEM + 10% FBSF, see section 2.2.1) to achieve a final concentration of 10 mM $CaCl_2$ or $SrCl_2$ in the treatment media. Vehicle control media was made up by adding the same volume of Milli-Q purified water to media.

T24 cells were seeded at 5 x $10^4$ cells/well in 24-well plates in 0.5 mL media and incubated for 24 hours at 37°C in 5% $CO_2$ to allow the cells to adhere prior to the experiment. Each

experimental condition (i.e. vehicle, $CaCl_2$, and $SrCl_2$ treatment) was set up with duplicate wells.

For the treatment, media was replaced with treatment or vehicle control media and the cells were incubated at 37°C in 5% $CO_2$ for 10 minutes. The cells were then immediately placed on ice and media was replaced with 100 µL of lysis buffer made up of 1% Triton X-100 (Fisher Scientific) in a solution containing protease and phosphatase inhibitors (cOmplete Mini, EDTA-free, protease inhibitor cocktail and phosSTOP; Roche) in PBS (Oxoid). Cell lysates were stored at -20°C or used immediately for western blotting.

### 2.13.2 Western blotting analysis

Protein in the cell lysates were denatured by combining 25 µL of lysate with 5 µL of 6X denaturing-SDS loading dye (Appendix E) at 95°C for 5 minutes. 25 µL of the denatured protein was loaded onto a 10% polyacrylamide gel containing 0.1% SDS (Appendix E) in a Tris/Glycine running buffer containing 0.1% SDS (Appendix E). Proteins were separated by size using electrophoresis conducted at 200 V for 30 minutes.

Resolved proteins were then transferred onto a nitrocellulose membrane (0.2 µm pores, Bio-Rad) in a Tris/Glycine transfer buffer containing 10% isopropanol (Appendix E), using the Trans-Blot Turbo transfer system (12 V for 10 minutes followed by 25 V for 30 minutes). Membranes were blocked in Odyssey blocking buffer (PBS; LI-COR) for 1 hour at room temperature.

Incubation with primary antibodies was conducted overnight at 4°C in 50% Odyssey blocking buffer diluted in PBS. Anti p38 (rabbit, Cell Signaling Technology [CST] #9212), anti p-p38 (mouse, CST #9216), anti ERK1/2 (rabbit, CST #9102), and anti p-ERK1/2 (mouse, CST #9106) were all used at 1:1000.

Membranes were briefly rinsed in PBS before incubating with secondary antibody for 1 hour at room temperature. IRDye 800CW goat anti-mouse (926-32210, LI-COR) and IRDye 680CW goat anti-rabbit (926-68071, LI-COR) were used at 1:25000 in 5% non-fat milk powder (Pams) in PBS.

Membranes were washed three times with PBS for 5 minutes and dried prior to visualisation on Odyssey CLx imaging system (LI-COR). Image Studio Lite software version 5.2.5 (LI-COR), was used to quantify the bands relative to the background above and below the band. Quantitative outputs were exported into Microsoft Excel for statistical analysis as described in section 2.5.

# Chapter 3: Results

# Chapter 3 Results

## 3.1 Investigating the effects of DCD-FLNA on osteoblast function

### 3.1.1 Introduction

Digitocutaneous dysplasia (DCD) is caused by a single mis-splicing event in *FLNA*. This results in the deletion of sixteen amino acids from the encoded filamin A protein (FLNA; NP_001104026.1:p.Val1724_Thr1739del) (16). This FLNA variant (referred to as DCD-FLNA from here on) evidently has an impact on the normal development of the skeleton, yet, how this is mediated remains unclear (3).

Abnormal development of bone can result from the dysregulation of one or both of bone deposition and bone resorption (1). These processes are controlled by three main cell types: bone-building osteoblasts, bone-resorbing osteoclasts, and mature osteocytes which monitor and modify the bone tissue they are embedded within – either directly, or indirectly by coordinating the activities of local osteoblasts and osteoclasts (1). While DCD-FLNA may be disrupting the function of any or all of these cell types, the work in this section is focused on the possible effects on osteoblasts. This is to address the hypothesis that the bony defects are mediated by the dysregulated activity of osteoblasts.

The study of genetic diseases is commonly conducted using patient cell lines. However, this was not feasible in this context for two reasons. Firstly, the rarity of this disease and the type of cell desired (osteoblasts) made inaccessibility an issue. Secondly, any cells sampled from patients could not be guaranteed to express the disease allele due to the extremely skewed X-inactivation patterns present in these individuals (16). Therefore, it was necessary to develop

a method by which we could introduce the mutation or the expression of DCD-FLNA into an established osteoblastic cell line.

The first step required was to identify a suitable cell line to model osteoblasts. It was important that this cell line was able to model the early stages of differentiation. This was necessary so that I could test the hypothesis that DCD-FLNA would induce accelerated differentiation and increased mineralization. Subsequently, methods to introduce the expression of DCD-FLNA into the chosen cell line were developed and optimised.

### 3.1.2 MC3T3-E1 differentiation can be examined using *Sp7* and *Runx2*

MC3T3-E1 is an immortalised pre-osteoblastic cell line initially isolated from the calvarium of a newborn mouse (130), and is widely used to study the factors that influence osteoblastic differentiation (131). Osteoblastic differentiation associated with collagen matrix deposition can be induced by stimulating these cells with ascorbic acid (132). Meanwhile, supplementation with organic phosphates enables the matured matrix to be mineralised (133,134).

To identify markers suitable for monitoring the early stages of osteoblastic differentiation in MC3T3-E1, gene expression was measured following treatment with ascorbic acid and β-glycerophosphate. Cells were seeded in 24-well plates at a density of $5 \times 10^4$ cells/well and allowed to adhere for 24 hours. Media was subsequently changed to differentiation media containing 50 μg/mL ascorbic acid and 10 mM β-glycerophosphate, and this time point was assigned as day 0. Samples were subsequently collected at 24 hour intervals over six days in culture with differentiation media. Quantitative PCR (qPCR) was used to measure the expression levels of three genes associated with osteoblast differentiation and mineralisation: *Sp7* (*osterix*) and *Runx2* encode transcription factors required for osteoblast differentiation

(135,136), while *Col1a1* encodes a component of type I collagen and is commonly used as an osteoblast-specific marker (137).

An increase in the expression of *Sp7* and *Runx2* was observed from day two in differentiation media. This increase was found to be statistically significant ($P < 0.05$) in unpaired, two tailed t-tests comparing each time point to the baseline at day 0. While there was a slight increase in the expression of *Col1a1* over the course of treatment with differentiation media, this was not statistically significant (Figure 3.1).

The results here indicate that *Sp7* and *Runx2* can be used as markers of osteoblastic differentiation in the MC3T3-E1 cell line. These can be used to measure the impact of DCD-FLNA expression on this process.

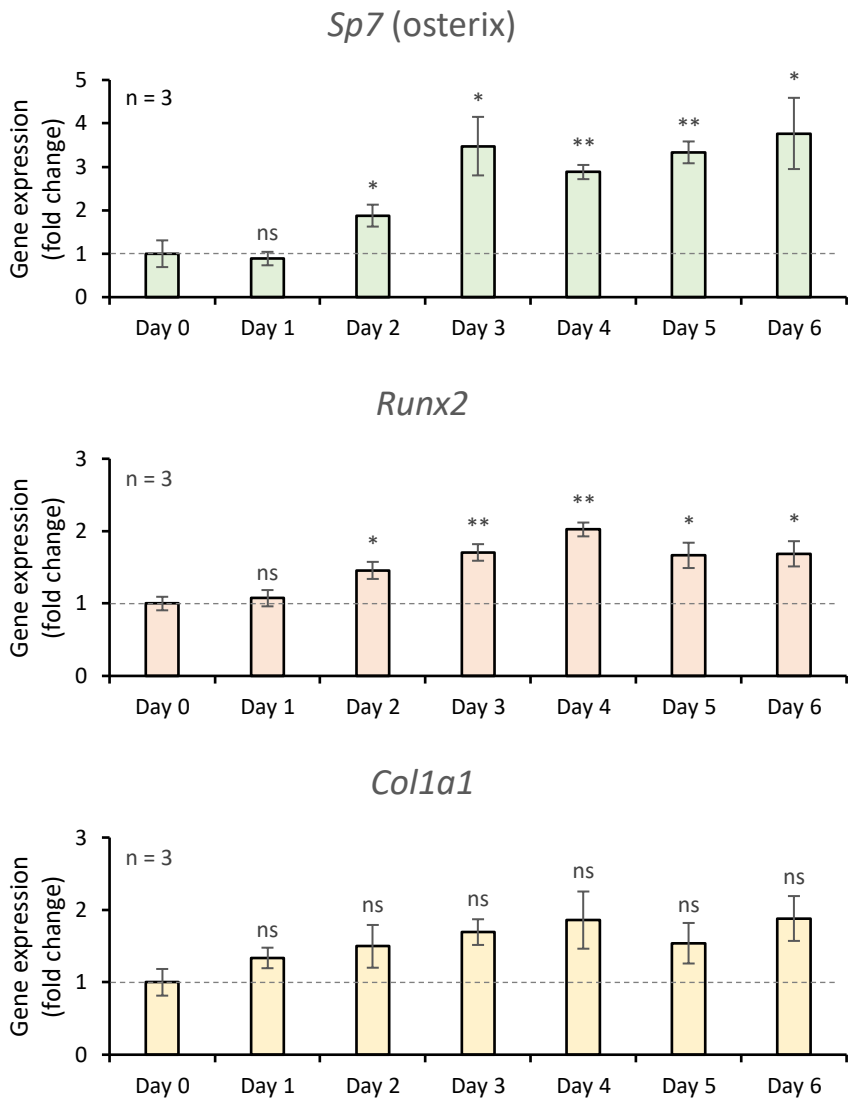


Figure 3.1: Expression levels of osteoblast markers in MC3T3-E1 as measured using qPCR following treatment with differentiation media for six days. There was a significant increase in the mRNA expression of *Sp7* and *Runx2* from day 2 while the increase in *Col1a1* was not found to be significant. Expression levels are described as fold change relative to baseline at day 0. Data was combined from three independent repeats (n = 3). Error bars indicate standard error of the means. *P < 0.05; **P < 0.01; calculated using an unpaired, two tailed t-test.

### 3.1.3 *Mus musculus* has the DCD variant in *Flna* but exhibits normal splicing

In the previous section, the MC3T3-E1 cell line was confirmed to have the necessary attributes to model the process of osteoblastic differentiation. However, the fact that it was derived from another species was something that needed to be considered. This was especially pertinent because the original study that identified the recurrent DCD variant had stated that this

nucleotide was not conserved in rodents (16). Accordingly, the genetic sequence encoding filamin A in mouse was compared to that of human to examine the differences that were present.

The reference sequences for human *FLNA* and mouse *Flna*[1] were obtained from Ensembl version 101 (31) and aligned to facilitate the identification of such differences. The final base of mouse exon 30 (corresponding to human exon 31) was found to be an adenine – the same as the disease allele responsible for DCD in humans (Figure 3.2). Other sequence differences were also observed in this region and these are highlighted using red font in Figure 3.2. These differences were much more common in the intronic sequences. This latter observation was not unexpected given that introns are typically not well conserved compared to exons (138).


Figure 3.2: Alignment of the human *FLNA* and mouse *Flna* sequences flanking the position of the recurrent DCD variant. Sequence from the end of human exon 31 and the start of the following intron is shown with the equivalent mouse exon 30 and its following intron. The final nucleotide of human *FLNA* exon 31 corresponding to the position of the recurrent G>A variant, is highlighted in yellow. The equivalent position in mouse is occupied by an adenine. Exonic sequences are in capitals and in black font while intronic sequences are in lower case and in dark blue. The nucleotides in the mouse sequence which differ from the human sequence are highlighted in red font.

In humans, the presence of an adenine at the last nucleotide of exon 31 is disruptive to normal splicing of this exon, as demonstrated in DCD. Whether the presence of an adenine at the equivalent position in mouse *Flna* would have the same effect was clearly an important question. There was a possibility that DCD-FLNA could in fact be a physiological isoform of FLNA in

[1] Transcript IDs: ENST00000369850.10 (*Homo sapiens*) and ENSMUST00000033699.12 (*Mus musculus*)
NB further references to exon numbers correspond to these transcripts

the mouse. In that case, cells derived from mice would not be suitable for investigating how DCD-FLNA causes disease in humans.

A publicly available mouse organ development RNA-seq datasets from the Wold lab, Caltech (139), was used to investigate this (with help from Dr Greg Gimenez, Department of Pathology, University of Otago). Rare, non-canonical alternative splicing events that utilised cryptic donor splice sites within mouse exon 30 (i.e. events that were potentially analogous to the mis-splicing event observed in DCD) were searched for by identifying split reads spanning from inside of exon 30 to the start of exon 31.

A total of 17 reads representing 3 potential cryptic splice sites in mouse exon 30 were identified. Eleven reads utilised a cryptic splice site located six nucleotides 5' to the original splice site (position -6; the last nucleotide of the exon being position -1), while 1 read utilised a site located forty-eight nucleotides from the original site (position -48; analogous to that observed in DCD), and the remaining 5 reads utilised a site that was located 132 nucleotides away (position -132) (Figure 3.3A). The levels at which these three events were observed were minimal compared to the >7600 reads mapping to the canonical junction between the end of exon 30 and start of exon 31 (Figure 3.3B). These mis-splicing events were considered to be background noise and not physiologically or pathologically relevant. The presence of an adenine at the last nucleotide of this exon did not appear have a detrimental effect on the normal splicing of this exon-intron junction in *Mus musculus*.

It was judged that, while the nucleotide variant itself cannot be studied in MC3T3-E1, the protein consequences (i.e. the deletion of the 16 amino acids in FLNA) should still be able to be studied using this cell line, given that DCD-FLNA was not a physiological isoform in the mouse.

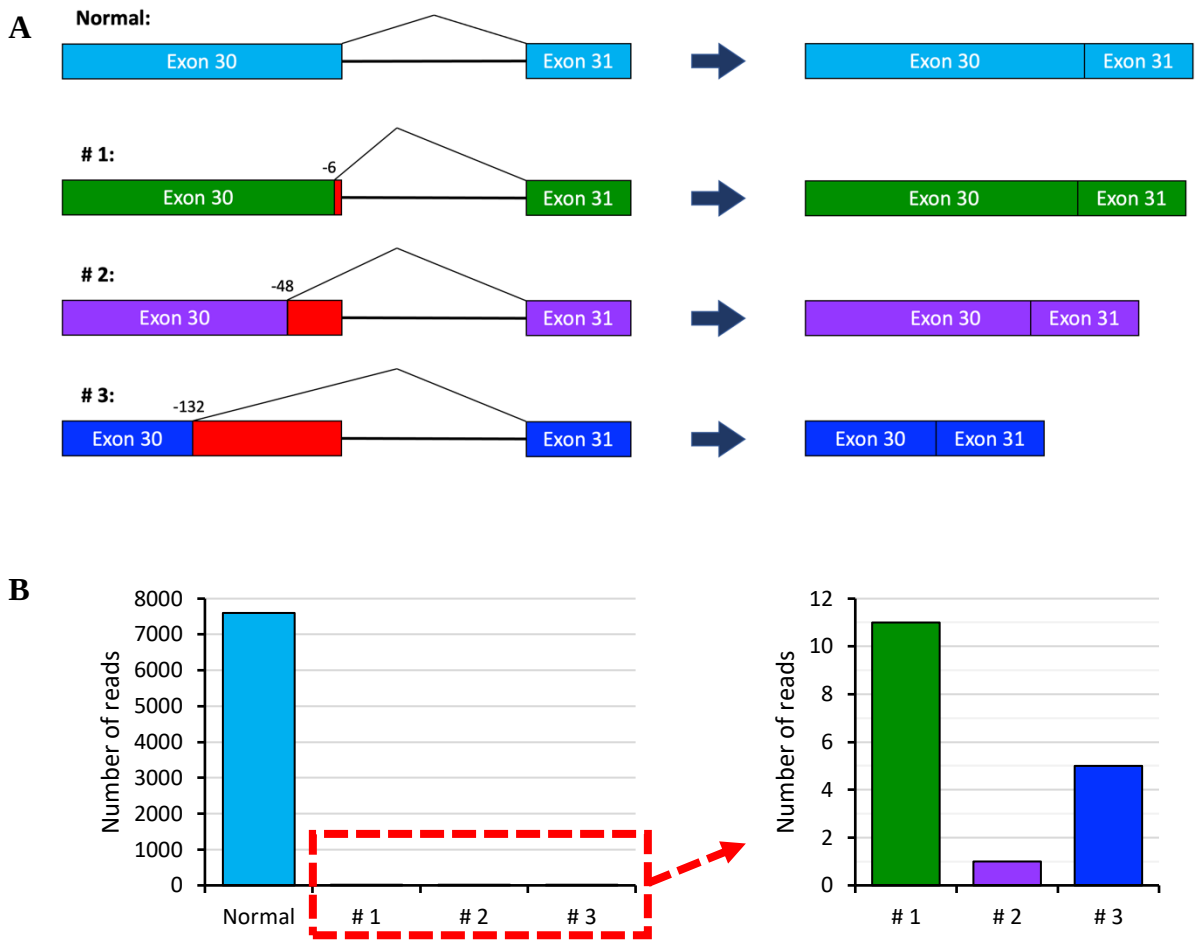


Figure 3.3: Alternative splicing events involving mouse *Flna* exon 30 that were identified in the mouse organ development RNA-seq data. (A) Three different cryptic donor splice sites were identified at 6, 48, and 132 nucleotides 5' to the original donor site. (B) Number of reads for the splicing events depicted in (A) are shown in the graph on the left. The graph on the right shows only the mis-splicing events with an adjusted scale.

### 3.1.4 Other species in the order Rodentia also have the DCD variant

The wild type allele of the mouse *Flna* contains a G>A transition (compared to the orthologous human site) which is equivalent to the recurrent DCD variant. In humans, this variant causes mis-splicing at this splice site, but no evidence of such mis-splicing was found in mice. There must be some differences between mouse and human in the regulation of splicing at this site to account for this observation.

Such differences may reside in *cis*-acting sequence features or *trans*-acting splicing regulatory factors. Investigation of the former was initiated by comparing the human and mouse DNA

sequences in this region (a small section is shown in Figure 3.2). However, with this strategy, there was no ability to differentiate between sequence differences which had some role in influencing splicing at this exon, and those that were simply a result of genetic divergence since the last mouse-human common ancestor, ~87 million years ago (140). Thus, a phylogenetic approach was taken.

A search was conducted to identify further species that carried the equivalent of the recurrent DCD variant (i.e. an adenine at the last nucleotide of the exon corresponding to human exon 31 of *FLNA*). The UCSC genome browser (http://genome.ucsc.edu) (122), with the conservation track (Vertebrate Multiz Alignment) was used to examine this nucleotide position in 100 vertebrate species. This nucleotide position was found to be highly conserved over a wide range of species; however, the same G>A transition was observed in a total of nine species belonging to the order Rodentia (branches highlighted in red in Figure 3.4). This was consistent with what had been reported by Sun et al. (16). The chinchilla, although part of the order Rodentia, did not have the G>A transition indicating that a reversion event had likely taken place. The only other species in this group of 100 vertebrates in which this nucleotide was not conserved was the spotted gar, which instead had a G>T transversion (highlighted in blue in Figure 3.4).

Subsequently, the sequences of the nine species of rodent were aligned with exon and intron 31 of human *FLNA*, as shown in Figure 3.5. Sequences were obtained from Ensembl version 101 (31), transcript IDs can be found in Appendix B. Nucleotides which differed from human but were the same in this group of rodents (i.e. changes that were co-inherited with the G>A transition equivalent to the recurrent DCD variant) are boxed in orange: one was found in the exonic sequence, and a further eleven in the intronic sequence. These were considered as candidates for the *cis*-acting features that could be preventing the G>A transition from mediating mis-splicing.

The finding of differences between rodents and human highlighted how interspecific differences could potentially generate further issues in experiments utilising the MC3T3-E1 cell line. This prompted the search for an established human-derived cell line that could be used to model osteoblast function.

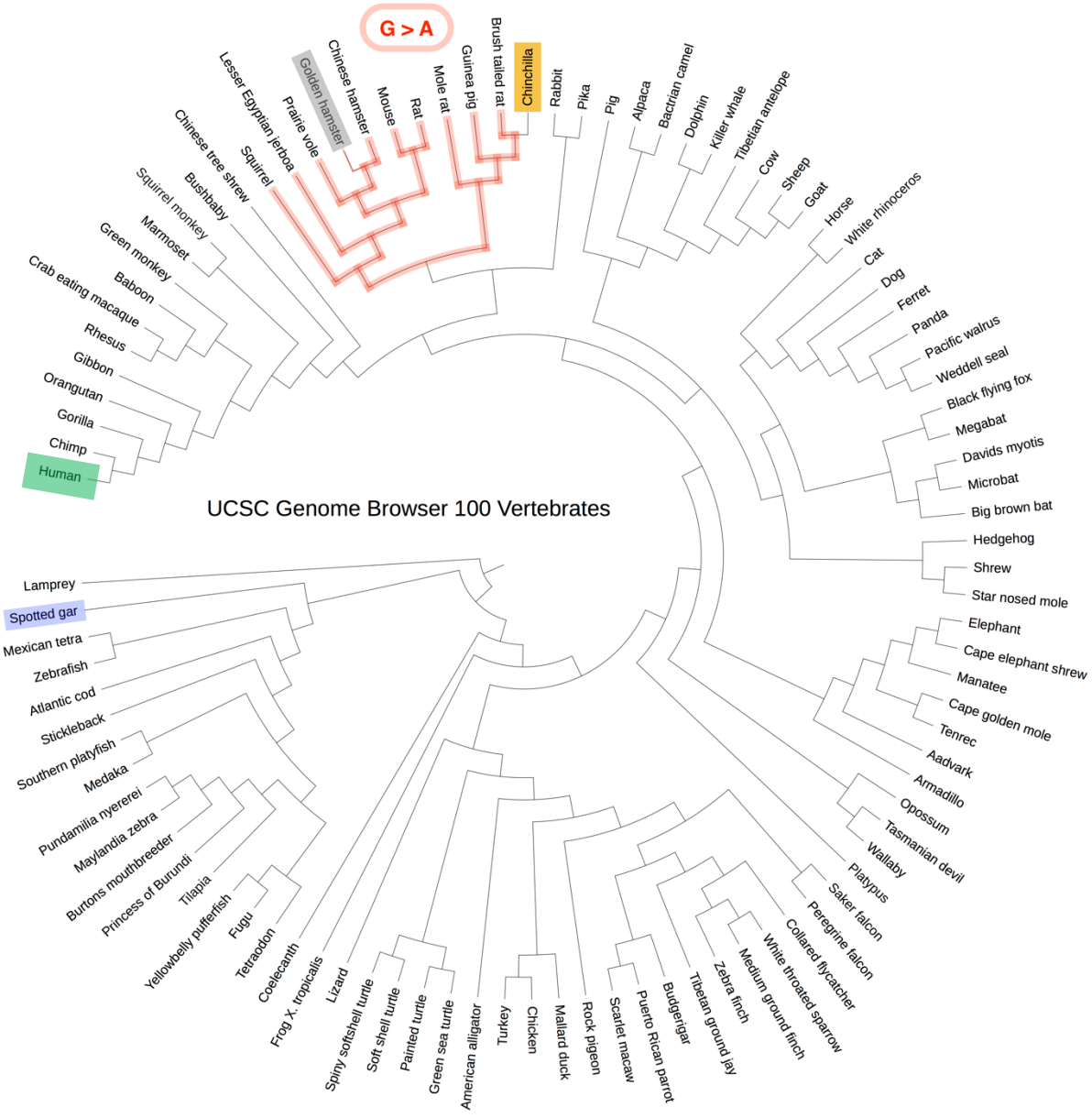


Figure 3.4: Phylogenetic tree of 100 vertebrate species. Human is highlighted in green. The branches that connect the species carrying the G>A transition equivalent to the recurrent DCD variant, are highlighted in red. This group represents the order Rodentia. No sequence was available for the golden hamster (greyed out). The chinchilla (highlighted in yellow) does not have the G>A transition at this position despite being part of the rodents, likely indicating a reversion event. The spotted gar (highlighted in blue) has instead a G>T transversion at this position and is the only other species in which this nucleotide is not conserved.

Figure created using Interactive tree of life (iTOL) (141), adapted from UCSC genome browser (142)

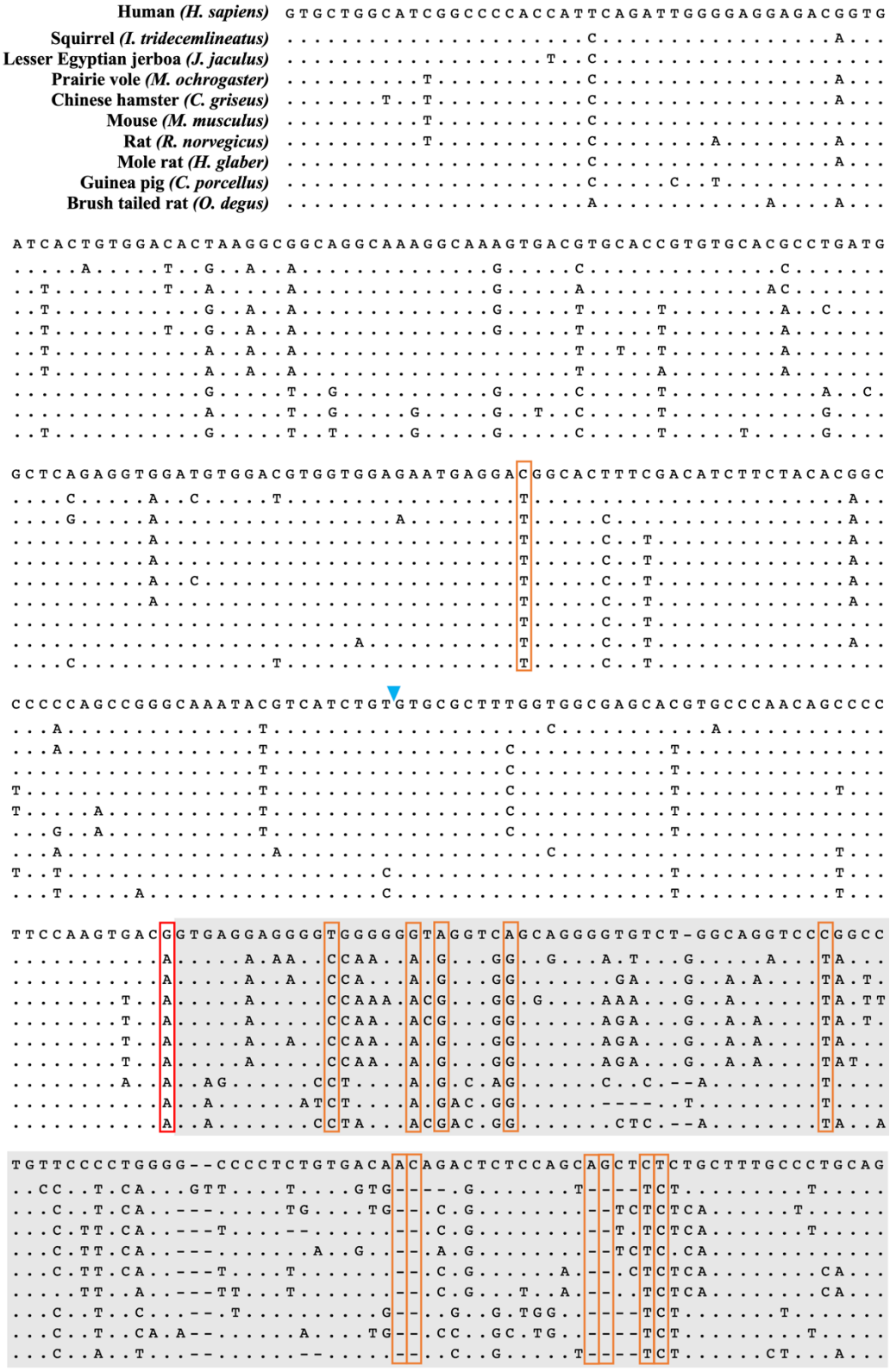


Figure 3.5: Alignment of human *FLNA* with that from nine species of rodent. Human exon 31 and intron 31 (greyed) with the equivalent sequences from rodent species. The G>A transition equivalent to the recurrent DCD variant is boxed in red. Dots (.) represent bases that are identical to the human sequence while dashes (-) indicate where there are gaps. Orange boxes indicate the nucleotides that are different to human but same within this group of rodents. The blue triangle indicates the location of the -48 cryptic splice site used in DCD. Sequences were obtained from Ensembl version 101 (31), and transcript IDs are listed in Appendix B.

Figure created using MEGA X (124) and Microsoft Word for Mac.

### 3.1.5 Human U2OS cell line can be stimulated to form a mineralised matrix

In the previous sections, it was established that mice do not normally express the mis-spliced isoform of FLNA and therefore MC3T3-E1 should be useful for studying the functional consequences of DCD-FLNA. However, it was thought possible that the interspecific differences could give rise to other issues that could interfere with future experiments. Hence, a human cell line to model osteoblast function was sought so that it could be used alongside or instead of the MC3T3-E1 cell line.

U2OS is a cell line that was isolated from a human osteosarcoma (143). Osteosarcoma is a primary bone cancer that consists of cells originating from mesenchymal stem cells which, at some stage of commitment to the osteoblastic lineage, have lost their ability to terminally differentiate (144). Cell lines derived from osteosarcoma are therefore commonly used to model osteoblasts. However, several studies have claimed that U2OS are unable to form mineralised matrix based on the finding that they express little to no functional alkaline phosphatase (ALP) under normal culture conditions (145,146).

I therefore hypothesised that U2OS, if cultured in the appropriate conditions, would undergo osteoblastic differentiation to form a mineralised matrix. A mineralisation assay was undertaken: U2OS cells were seeded in 24-well plates at a density of $5 \times 10^4$ cells/well and allowed to adhere for 24 hours. Media was changed to differentiation media containing 50 μg/mL ascorbic acid, 10 mM β-glycerophosphate, and 0.02 μM dexamethasone – this timepoint was taken as day 0. Cells were fixed at days 0, 2, 6, 10, 15 and 20, and then stained with Alizarin Red S to visualise the formation of calcium deposits. Figure 3.6 shows the stained cells when viewed under bright field microscopy. All images were taken at the same magnification, although the cells appear smaller in the later time points due to increased cell density as the cells continued to proliferate. The red staining of the calcified nodules was

particularly evident after 20 days, thus demonstrating the ability of U2OS to form mineralised matrix. This result confirms the utility of this cell line for investigating the effects of DCD-FLNA expression on osteoblast function.

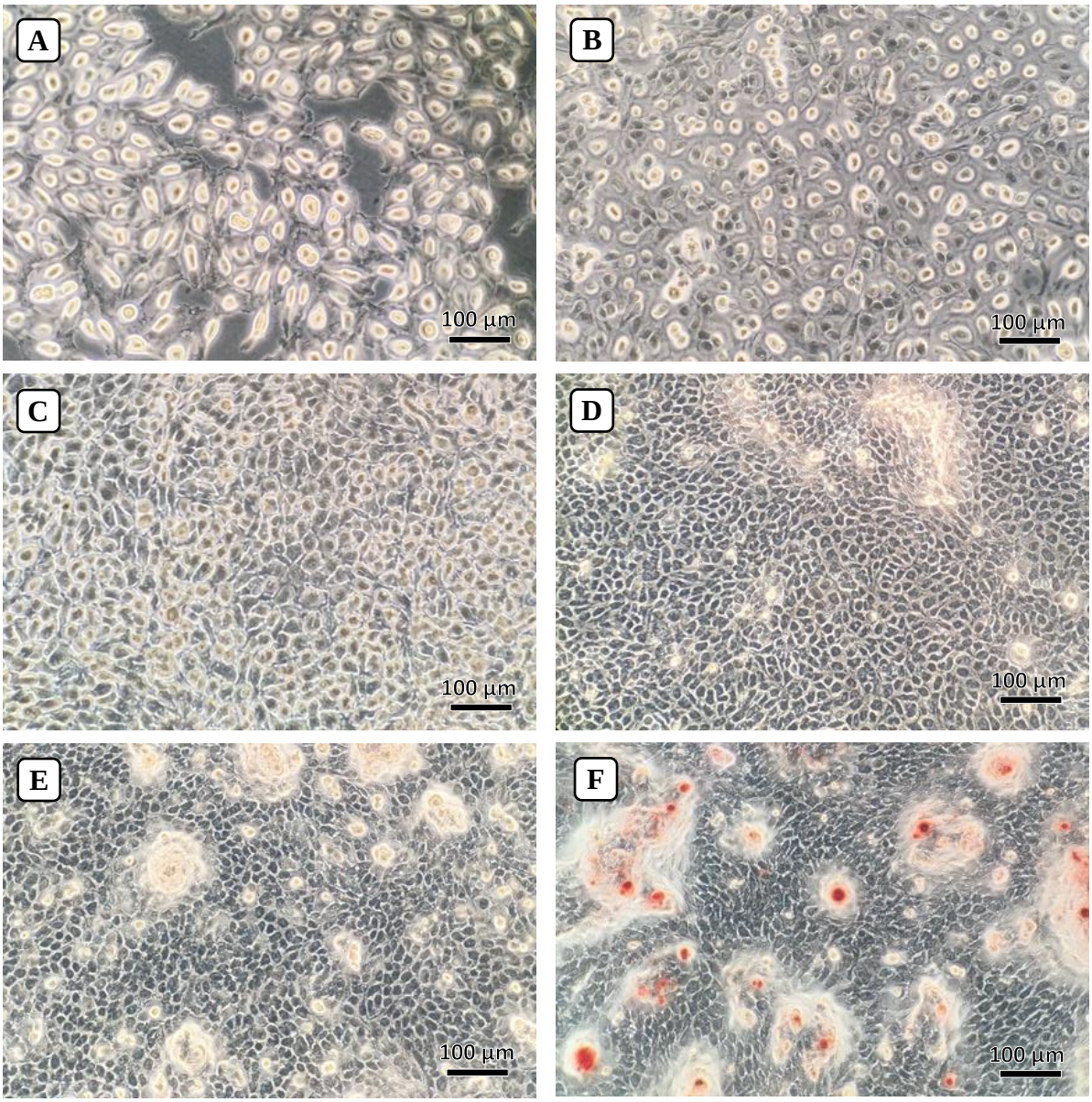


Figure 3.6: Alizarin Red S staining for calcium deposits produced by U2OS cells after being cultured in the presence of ascorbic acid, β-glycerophosphate, and dexamethasone for 0 days (A), 2 days (B), 6 days (C), 10 days (D), 15 days (E), and 20 days (F). Calcium deposits were particularly prominent on day 20. Scale bar = 100 µm.

### 3.1.6 AONs could not reproduce the mis-splicing event responsible for DCD

Mouse-derived MC3T3-E1 and human-derived U2OS were chosen to be used for modelling osteoblast behaviour. The next step to investigate the functional consequences of the mis-spliced variant of FLNA was to develop a method to introduce the expression of DCD-FLNA into these cells.

Antisense oligonucleotides (AONs) were employed for this purpose. AONs are modified RNA or DNA molecules that are designed to hybridise to complementary sequences in target pre-mRNA molecules (125). They disrupt normal splicing by interfering with the binding of trans-acting splicing factors, either directly by acting as a steric block, or indirectly by altering the secondary structure of the pre-mRNA molecule (147,148). The outcome of this is commonly whole exon exclusions and thus AONs are also known as splice switching oligonucleotides (147).

A suite of AONs designed to overlie this 5' splice region (of human *FLNA* exon 31 and mouse *Flna* exon 30; see Appendix B for transcript IDs) were evaluated *in silico* using the guidelines described by Aartsma-Rus (125). The 3' end of an oligonucleotide has been found to be important for annealing (149), therefore, two oligos were designed for each of mouse and human: the first had the 3' nucleotide binding to the position of the recurrent variant (final nucleotide of the exon), and the second binding to the position of the variant associated with the atypical case of DCD discussed in section 1.2.3 (five bases into the following intron) – see Figure 3.7. These were designated mAON1 and mAON2 respectively for mouse and hAON1 and hAON2 for human.

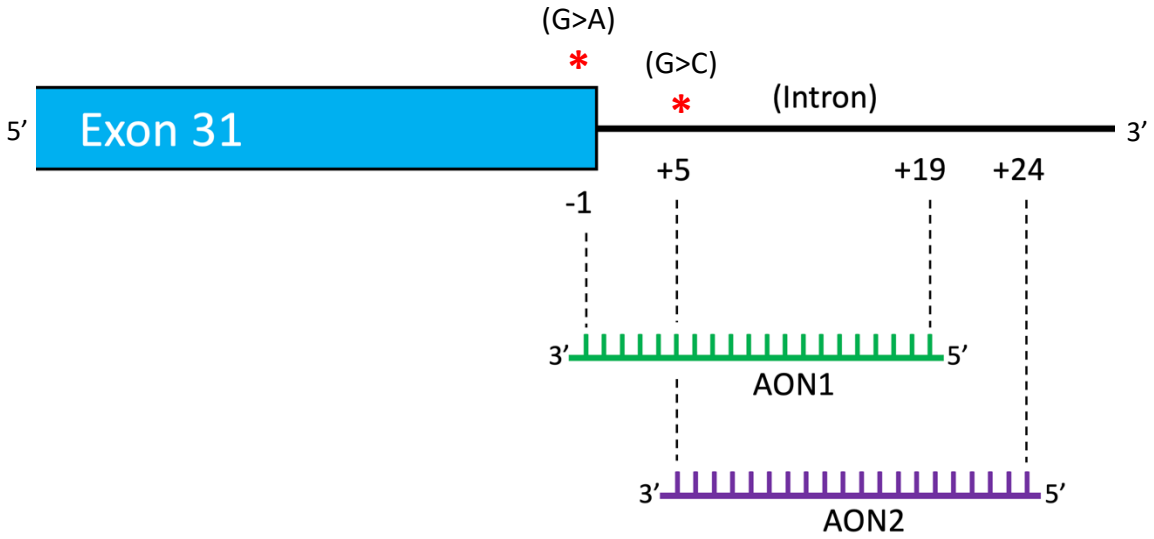


Figure 3.7: Positions of AON1 and AON2 relative to the exon-intron junction of interest (human *FLNA* exon 31, mouse *Flna* exon 30; see Appendix B for transcript IDs). The positions of the recurrent variant (G>A) and the variant responsible for the atypical case of DCD (G>C) are marked with red asterisks. -1 indicates the last nucleotide of the exon while +5 means five nucleotides into the intron. AON1 (green) and AON2 (purple) are lined up to illustrate how their 3' nucleotides bind to the locations of the recurrent and atypical variants respectively.

MC3T3-E1 cells were transfected with mAON1 and mAON2 to determine whether these AONs were capable of reproducing the pathogenic mis-splicing event. It was important that the event be exact given that other variants in this region of *FLNA* produce slightly different skeletal phenotypes (discussed in section 1.3.4). Cells were seeded at a density of 1 x $10^5$ cells/well in 24-well plates and allowed to adhere for 24 hours prior to transfection with AONs at 1 pmol/well. Cells were harvested 24 hours following transfection for the analysis of RNA using RT-PCR.

RT-PCR showed that both mAON1 and mAON2 induced mis-splicing. This was indicated by the presence of an extra band that was absent in our two controls (transfected with an AON with a scrambled sequence or untransfected; Figure 3.8A). Sequencing of these PCR products was pursued to confirm the identity of these bands. This was achieved by first separating the PCR products by cloning into the pGEM-T vector, and then subsequently Sanger sequencing directly from plasmid. The first band represented the expected sequence of normally spliced *Flna* – indicated as WT (wild type) in Figure 3.8. The second band represented a mis-spliced

form of *Flna* lacking the final 132 nucleotides (nt) of exon 30 (Figure 3.8B; diagrammatic representation of this splicing event in Figure 3.3A #3). This was not the DCD-associated event involving the removal of the final 48 nucleotides of exon 30 (analogous to the mis-splicing event in humans with DCD). Consequently, it was not deemed appropriate to utilise this approach for functional studies.

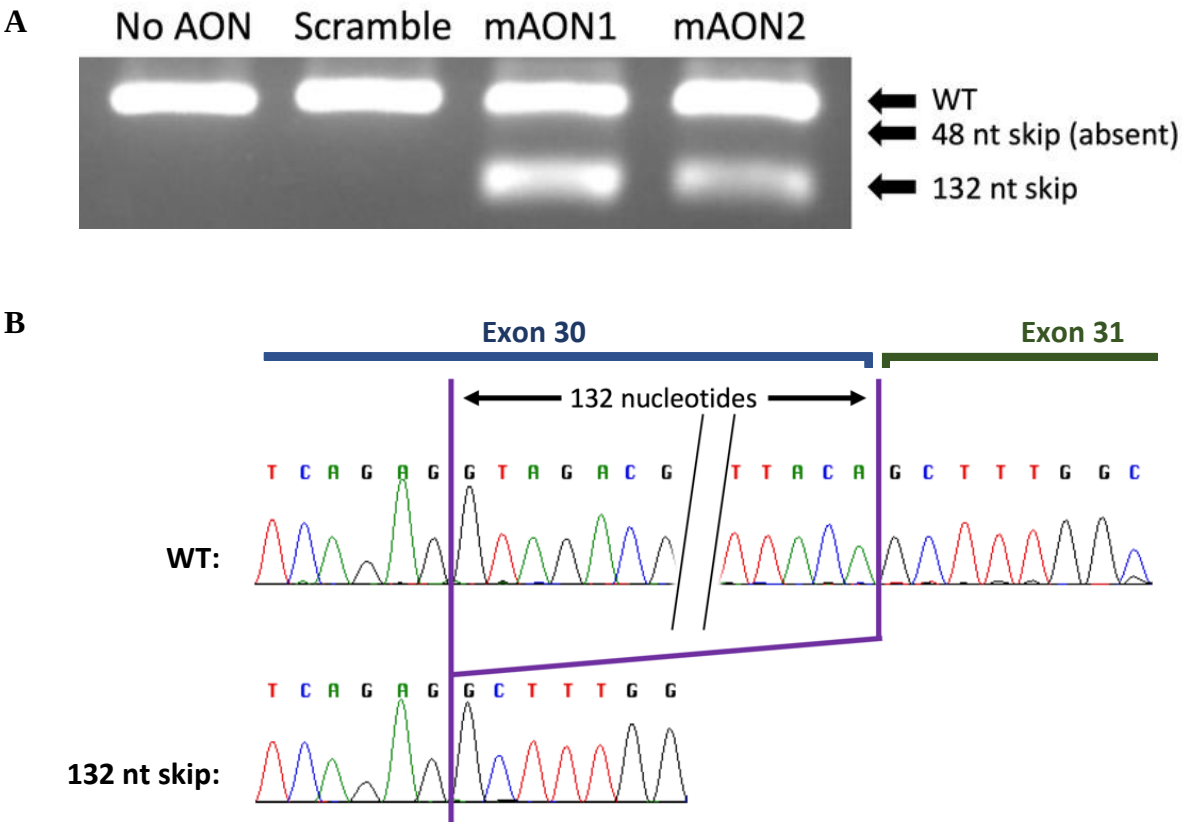


Figure 3.8: AON transfections into MC3T3-E1 were not able to produce the mis-splicing event analogous to that observed in DCD. (A) RT-PCR result showing the presence of the wild type *Flna* transcript in all four samples. In samples transfected with mAON1 and mAON2 an additional band indicating a smaller product was observed. (B) Sanger sequencing of the RT-PCR products from mAON1 demonstrated that the smaller product was an abnormally spliced *Flna* transcript lacking the final 132 nucleotides (nt) of exon 30. WT, wild type i.e. normally spliced *Flna*; Scramble, sample transfected with AON with random sequence.

Subsequently, AONs were tested on (human) U2OS cells as this approach should avoid any issues arising from interspecific differences. Transfections with hAON1 and hAON2 were carried out in U2OS cells at 1 pmol/well and harvested after 24 hours as with the MC3T3-E1 above. RT-PCR was unable to demonstrate the production of any mis-spliced transcripts (Figure 3.9A). To exclude the possibility that the dose of the AONs was too low, transfections

were repeated at concentrations that were two to twenty times the amount of AON i.e. at 2, 5, 10, and 20 pmol/well. No mis-splicing events were observed (Figure 3.9B).

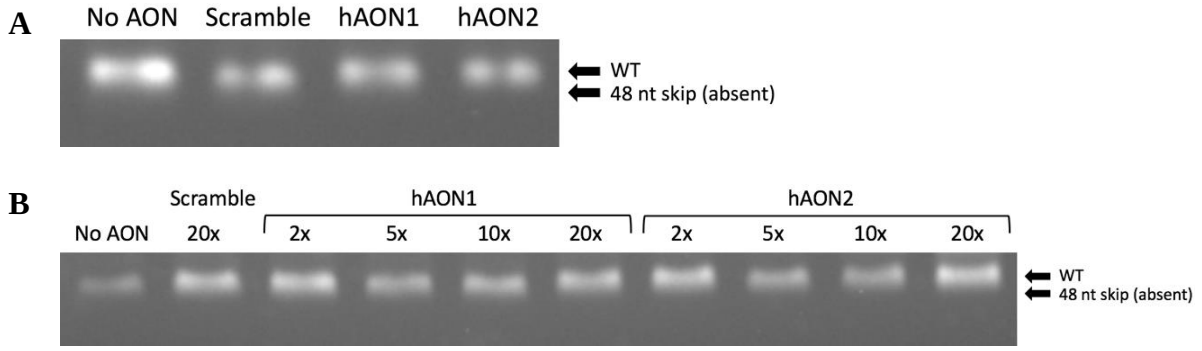


Figure 3.9: AON transfections into U2OS did not reproduce the mis-splicing event observed in DCD, at concentrations used for MC3T3-E1 (A), and with higher concentrations (B). WT, wild type i.e. normally spliced *FLNA*; Scramble, sample transfected with AON with random sequence.

The lack of response to transfection with AONs in U2OS cells could have been due to either host cell related factors (e.g. cell line specific abnormalities in regulation of splicing) or factors relating to the transfection (e.g. transfection reagent efficacy, AON design suitability). The former was investigated by testing the AONs in another human cell line.

Primary human fibroblasts were chosen for this purpose because the initial discovery of the mis-splicing event was made in samples of fibromas, which are composed of cells that are thought to be fibroblastic or myofibroblastic (12,16). Transfections with hAON1 and hAON2 were carried out in primary human fibroblasts in the same way as the previous two cell lines. RT-PCR on these samples was unable to demonstrate any mis-splicing in transfected fibroblasts (Figure 3.10). Having failed to reproduce the desired mis-splicing event in three separate cell lines, the use of AONs were abandoned and a different approach to express DCD-FLNA was pursued.

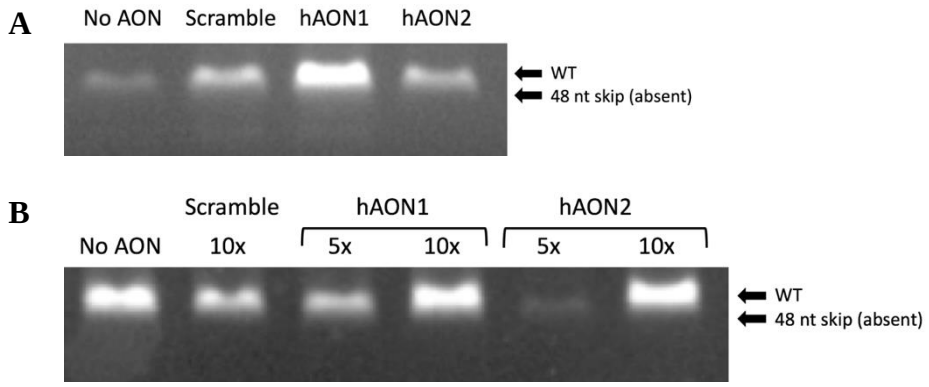


Figure 3.10: AON transfections into primary control fibroblasts were not able to reproduce the mis-splicing event observed in DCD, at concentrations used for MC3T3-E1 (A) and at higher concentrations (B). WT, wild type i.e. normally spliced *FLNA*; Scramble, samples transfected with AON with random sequence.

### 3.1.7 Construction of a DCD-FLNA plasmid for transfecting into MC3T3-E1

In the previous section, it was discovered that antisense oligonucleotides were unable to induce the DCD mis-splicing event in both mouse and human cell lines. Hence another method to introduce the expression of DCD-FLNA into the chosen osteoblastic cell line was needed. Thus, an approach involving transient transfections of DCD-FLNA expression plasmids was adopted. The MC3T3-E1 cell line would be used for these experiments as they were deemed to be a better model of osteoblasts than the U2OS cell line.

A dual expression plasmid was designed in order to introduce the expression of DCD-FLNA alongside short hairpin RNA (shRNA) to knockdown endogenous *Flna* (Figure 3.11A). Ultimately, this plasmid would be transfected into MC3T3-E1 cells and expression levels of markers of differentiation would be compared to transfections with the same vector containing the sequence encoding wild type FLNA (WT-FLNA).

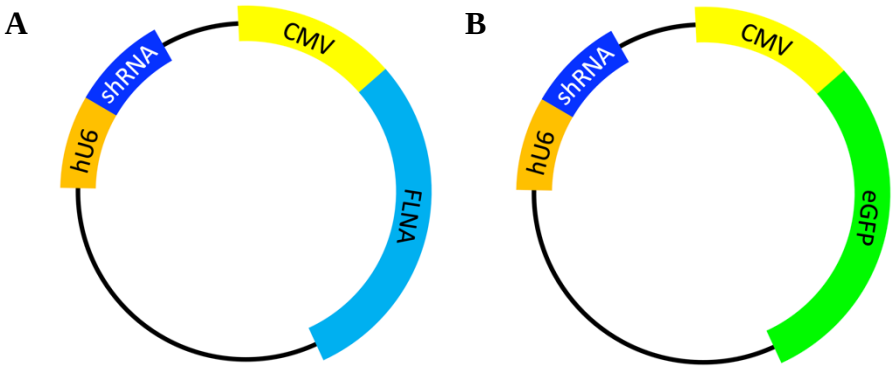


Figure 3.11: Design of the dual expression plasmid for expressing DCD-FLNA in MC3T3-E1. Human U6 (hU6) promoter drives the expression of short hairpin RNA (shRNA). shRNA would have one of: scrambled sequence (control; shRNAscr), sequence targeting the 3' UTR of *Flna* (shRNA1), or that targeting the 5'UTR (shRNA2). The cytomegalovirus promotor (CMV) drives the expression of (A) *FLNA* (WT or DCD-FLNA) for functional assays, or (B) enhanced green fluorescent protein (eGFP) for initial optimisation of transfections. Lengths of the sequences are not to scale.

The first step was to test the efficacy of the shRNA-mediated knockdown of endogenous FLNA. Two different shRNA sequences were evaluated. The first targeted the 3' UTR of *Flna* (shRNA1) and the second targeted the 5' UTR (shRNA2). Constructs with shRNA1 or shRNA2 under the hU6 promotor were produced as described in methods. Subsequently, the sequence encoding enhanced green fluorescent protein (eGFP) was inserted into the second multiple cloning site under the cytomegalovirus (CMV) promotor (which drives gene expression in mammalian cells; Figure 3.11B). The expression of eGFP would permit the visual detection of transfected cells under fluorescence microscopy for the assessment of the transfection efficiency. A construct containing an shRNA with scrambled sequence (shRNAscr) and eGFP was already available in the laboratory.

An initial transfection of the shRNA-eGFP plasmids into MC3T3-E1 cells was trialled at 400 ng/well in 24-well plates. This achieved a suboptimal transfection efficiency of 30-40% as determined by fluorescence microscopy. There were no observable differences in the transfection efficiency over three time points (24, 48, 72 hours), or between the three plasmid constructs (shRNAscr, shRNA1, shRNA2). Cell viability appeared to be adversely affected by the transfection, as determined by cell morphology (observed using phase-contrast

microscopy). Cells were harvested for RNA after 72 hours to assess the level of knockdown of *Flna* using qPCR. Both shRNA1 and shRNA2 showed some knockdown when *Flna* mRNA levels were compared to cells transfected with shRNAscr (Figure 3.12).

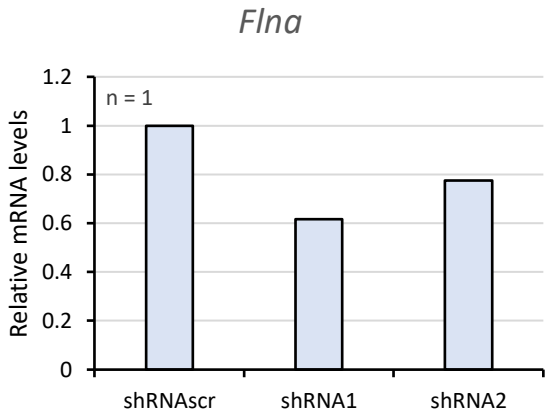


Figure 3.12: Knockdown of *Flna* in MC3T3-E1 by shRNA transfection, measured using qPCR 72 hours after transfection. Preliminary result from a single experiment (n = 1) shows that that there was some reduction in mRNA levels of *Flna* with both shRNA1 and shRNA2, and that the knockdown was greater with shRNA1. The mRNA levels are expressed as a relative quantity compared to cells that were transfected with shRNAscr.

This preliminary result indicated that both shRNA1 and shRNA2 were capable of silencing *Flna* expression but were limited by the transfection efficiency. Therefore, attempts were made to improve the transfection efficiency, and this is detailed below. Meanwhile, insertion of the sequences encoding WT- and DCD-FLNA into the vector containing shRNA1 was initiated as it had the greater knockdown effect. However, technical difficulties were encountered, and time constraints did not allow for this work to be completed.

Various aspects of the transfection protocol were modified to see if the transfection efficiency could be improved. Firstly, the amount of plasmid for transfection was adjusted. Transfections with 400 ng, 800 ng, and 1600 ng were trialled. Increasing the amount of plasmid did not substantially improve the transfection efficiency. Meanwhile, the cell viability was decreased. Therefore 400 ng of plasmid was used for subsequent optimisation steps.

The amount of transfection reagent used was also investigated. Increasing the amount of Lipofectamine 2000 from 2 μL to 3 μL did not visibly alter either transfection efficiency or cell viability. Therefore, I decided to continue using 2 μL of Lipofectamine 2000 per transfection.

Next, the transfection procedure was modified to improve the cell viability. A modified reverse transfection was conducted whereby the MC3T3-E1 cells were seeded at confluency and transfection mix added immediately. After five to six hours, the cells were split into four wells and allowed to grow. Transfection efficiency (observed after 24, 48, and 72 hours) did not seem to be substantially different to that from the initial forward transfection procedure. However, there was a significant improvement in cell viability, as determined by cell morphology.

There was a possibility that the poor transfection efficiency was due to the plasmid preparation being of low quality or purity, rather than the cell host being resistant to uptake. To exclude this possibility, transfections were trialled in HEK293FT cells which are known to be readily transfected. HEK293FT cells were seeded at confluency into 24-well plates and transfection mixes with 2 μL Lipofectamine 2000 and 400 ng of shRNA-eGFP plasmid were immediately added. Fluorescence microscopy was used to visualise transfected cells 72 hours after transfection. Figure 3.13 shows representative images from shRNA1-eGFP transfection into MC3T3-E1 and HEK293FT after 72 hours. The cells that have taken up the plasmid fluoresce green due to expression of eGFP. Since I observed greater transfection into HEK293FT, the plasmid preparation was unlikely to be the issue.

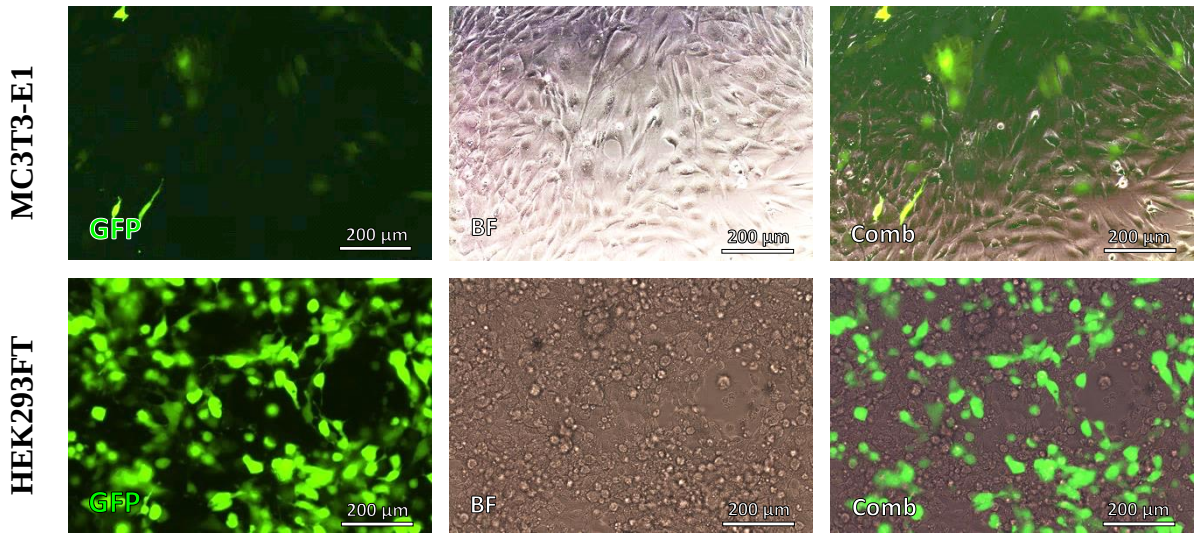


Figure 3.13: Transfection efficiency in MC3T3-E1 and HEK293FT as observed under fluorescence and bright field microscopy, 72 hours after transfection. Cells that have taken up the shRNA1-eGFP plasmid appear green under the GFP filter. Bright field (BF) view shows all cells present in the view. 'Comb' means combined image of GFP and BF.

One further factor that could have been limiting the transfection efficiency in MC3T3-E1 was the transfection reagent itself. Three other transfection reagents were trialled (Lipofectamine 3000, Lipofectamine LTX, FuGENE HD) at several different concentrations as indicated in the user manuals. However, none showed any significant improvement in transfection efficiency over the original transfection reagent (Lipofectamine 2000).

None of the above measures were able to produce a satisfactory transfection efficiency, and this line of work had to be concluded due to time constraints.

## 3.2 Investigating the possible role of CaSR in DCD

### 3.2.1 Introduction

The mis-splicing event responsible for DCD results in the deletion of sixteen amino acid residues near the middle of the FLNA protein (16). This region of FLNA has been shown to interact with the extracellular calcium-sensing receptor (CaSR) (67,68). This particular interaction may therefore be affected by the deletion of these 16 amino acid residues. This interaction has been found to be necessary for some of the signaling pathways utilised by CaSR (67,68,98,115,116). We hypothesised that the deletion in DCD disrupts osteoblast function by inappropriately activating signaling pathways downstream of CaSR – specifically, through the CaSR-FLNA-TAK1/TAB2-p38 pathway (see introduction section 1.4.4 and Figure 1.6 for details on this predicted pathway).

Stimulation of CaSR has previously been shown to activate p38 (120). The work in the next section aimed to prove the involvement of FLNA and the TAK1/TAB2 complex in this signaling pathway. This required the establishment of an assay in which the levels of p38 activation could be measured following CaSR stimulation. Subsequently FLNA and/or TAK1/TAB2 expression would be modulated to determine the necessity of these components in this pathway.

The first step involved the identification of a cell line that expresses *CASR*. Previous studies have used HEK293FT cells that have been stably transfected with CaSR; however, endogenously expressed CaSR was preferred as the expression levels were more likely to represent physiologically relevant levels. Thus, the next section describes the unexpectedly difficult process of finding a cell line that expresses CaSR.

### 3.2.2 Expression of CaSR in MC3T3-E1 at the mRNA level

There have been disagreements in the literature about whether the MC3T3-E1 cell line expresses *Casr* (110,112,150,151). It has been proposed that CaSR gene expression may be lost during *in vitro* cell culture (150), and therefore the discrepancies in the literature may represent differences between batches of the same cell line. RT-PCR was used to investigate whether the MC3T3-E1 used in our laboratory expressed *Casr* at the mRNA level.

The PCR conditions for the primer pair used to amplify *Casr* were optimised using cDNA from mouse bone (already available in the laboratory), in which mRNA expression of *Casr* was detected (Figure 3.14). The addition of 20% combined enhancer solution (CES) to the PCR reaction and the use of a touchdown program for thermal cycling enabled consistent results to be obtained. Sanger sequencing of the PCR product amplified from mouse bone cDNA confirmed that the band observed on the gel was indeed *Casr*.

RT-PCR on untreated MC3T3-E1 was initially conducted but this yielded no bands. Given that this cell line was considered to be pre-osteoblastic, it was hypothesised that expression of *Casr* would be induced during differentiation into mature osteoblasts. To investigate this, RT-PCR was conducted on samples obtained from the differentiation experiments described in section 3.1.2. No expression of *Casr* could be detected in MC3T3-E1 over the six days in differentiation media (Figure 3.14A). It was then questioned whether six days was long enough for the MC3T3-E1 to differentiate sufficiently. Therefore, samples were obtained from MC3T3-E1 cells cultured in differentiation media for 10, 15, 20, and 25 days; however, no *Casr* expression could be detected in these cells using RT-PCR (Figure 3.14B).

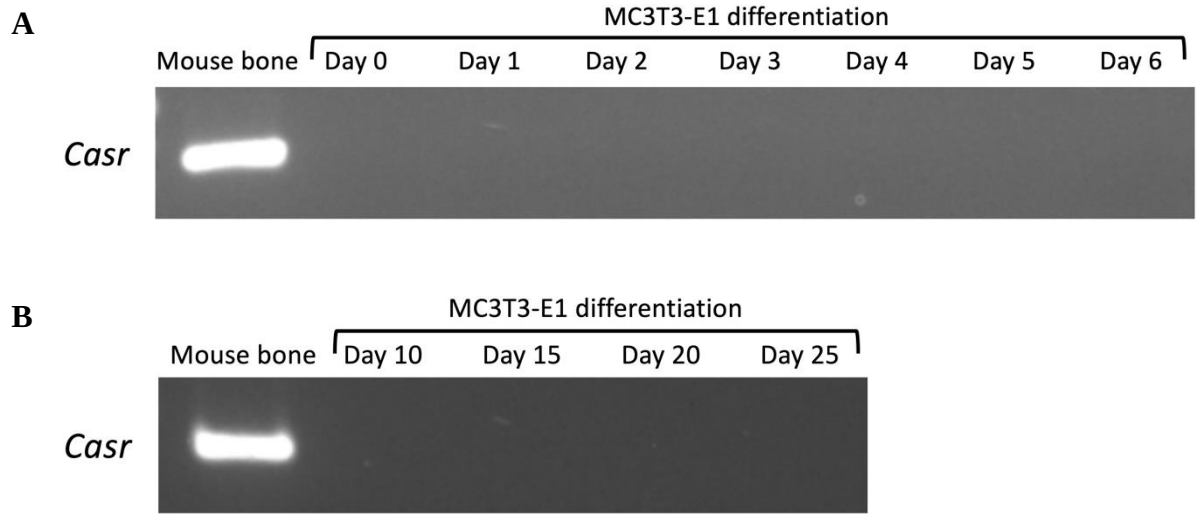


Figure 3.14: *Casr* expression was not able to be detected in MC3T3-E1 using RT-PCR. cDNA from mouse bone was used as a positive control for these experiments. (A) RT-PCR on MC3T3-E1 cultured in differentiation media for up to six days did not produce bands for *Casr*; representative image from three biological repeats. (B) RT-PCR on MC3T3-E1 cultured in differentiation media for up to twenty-five days also did not yield any bands. All MC3T3-E1 cells used were of less than twelve passages.

### 3.2.3 Expression of CaSR in human cell lines at the mRNA level

Following the inability to detect the expression of CaSR at the mRNA level in the MC3T3-E1 used in our laboratory, a search was initiated to identify a human cell line with such expression.

Initially, primer sequences obtained from D'Espessailles et al. (152) were tested on cDNA from three different cell lines: U2OS, human mesenchymal stem cells that had been cultured in osteogenic medium for 25 days (hMSC), and control human fibroblasts (RNA from the latter two were already available in the lab and cDNA was synthesized according to section 2.3.3). RT-PCR using the standard cycling conditions gave no bands, so a gradient PCR was used to determine the optimal annealing temperature. Bands were obtained at annealing temperatures between 51.7-58.4°C; however, none were of the expected size, and sequencing confirmed that the bands observed were the result of off-target amplification.

A further two primer pairs were designed, but neither yielded any bands apart from primer dimers. It was thought that this might be an indication of the absence of *CASR* expression in

these cell lines rather than there being an issue with all three primer pairs that were tested. In order to determine whether there were other cell lines available in the laboratory with *CASR* expression, the Human Protein Atlas (153), available at http://www.proteinatlas.org, was consulted. The RT4 cell line derived from transitional cell papilloma originating in the urinary bladder was shown to express *CASR*. While this cell line was not available in the laboratory, another cell line from the urinary bladder, T24 (derived from transitional cell carcinoma) was chosen to be tested for *CASR* expression.

An initial RT-PCR with cDNA from hMSC and T24 using a touchdown program and 20% CES produced a single band of a size matching *CASR* in T24 but not hMSC (Figure 3.15). Sanger sequencing of the PCR product confirmed the identity of the band to be *CASR*.

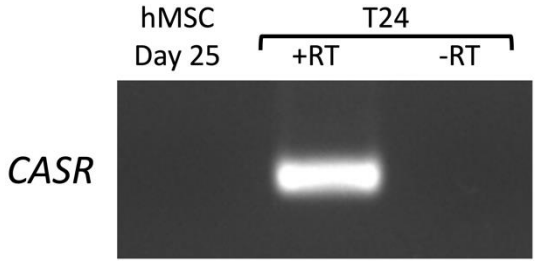


Figure 3.15: mRNA expression of *CASR* was detected in T24 cell line but not in human mesenchymal stem cells that had been cultured in osteogenic media for 25 days (hMSC Day 25). +RT and -RT indicates the presence and absence of reverse transcriptase in the reaction for cDNA synthesis (-RT can serve as a negative control to exclude PCR amplification from genomic DNA or contamination from other sources).

However, further repeats of this RT-PCR to confirm the absence of *CASR* expression in the other cell lines initially investigated, revealed that this primer pair was imperfect. Variable results were obtained from running the same sample (T24 cDNA) multiple times under the same conditions. On several occasions, a single clean band like that in Figure 3.15 was observed, while on other occasions, a band of a larger size was present with or without the band representing *CASR* (Figure 3.16). The larger band was confirmed to be off-target amplification of *RPS2* (encoding 40S ribosomal protein S2) with Sanger sequencing.

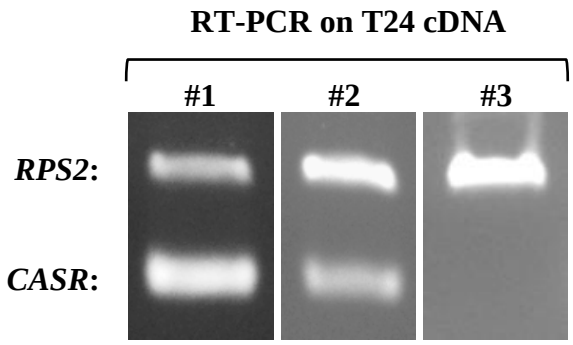


Figure 3.16: Repeats of RT-PCR for *CASR* on T24 produced different results on three different occasions. All were run using the same touchdown PCR programme with 20% CES added. Lane one shows a slightly greater intensity for the band representing *CASR* compared to *RPS2*, while lane two shows the opposite. Meanwhile, the band for *CASR* is completely absent in lane three.

In an attempt to circumvent the issue of off-target amplification, a further four primer pairs were tested using RT-PCR on cDNA from T24 cells. They either gave no bands or gave only bands representing non-specific amplification. Subsequently, these four primer pairs were tested on plasmid DNA containing sequence from human CaSR cDNA. The purpose of this was to allow the examination of the suitability of these primer pairs for PCR amplification of *CASR* without influence from off-target amplification of other cDNA sequences. Three of the four primer pairs yielded a single clean band of the appropriate size, indicating that these primers can successfully amplify *CASR*. Following this, various PCR conditions were tested in an attempt to achieve specific amplification of *CASR*. However, the issue was unable to be solved.

None of the primer pairs tested were considered to be sufficiently robust to be able to produce conclusive evidence for the absence of CaSR expression. However, given that the positive RT-PCR result from T24 was validated using Sanger sequencing, we could conclude with some confidence that CaSR expression was present in this cell line. Accordingly, the next line of work involving the stimulation of CaSR with calcium and strontium was conducted using the T24 cell line.

### 3.2.4 Stimulation of T24 cells with calcium and strontium

The T24 cell line was deemed useful for experiments investigating the hypothesised CaSR-FLNA-TAK1/TAB2-p38 pathway, given that *CASR* expression could be demonstrated at the mRNA level.

Previous studies have demonstrated that stimulation of CaSR with calcium or strontium can activate ERK1/2 and p38 (154,155). An attempt was made to replicate this result in the T24 cell line. Cells were seeded at a density of 5 x $10^4$ cells/well in 24-well plates and allowed to adhere for 24 hours prior to treatment with calcium or strontium. The cells were treated with media containing 10 mM $CaCl_2$ or 10 mM $SrCl_2$, or an equivalent volume of vehicle ($H_2O$) for 10 minutes. The cells were harvested thereafter and the quantity of phosphorylated p38 (p-p38) and phosphorylated ERK1/2 (p-ERK) were measured using western blotting. Both $CaCl_2$ and $SrCl_2$ were able to produce a statistically significant, albeit small, increase in p-p38 in T24 cells (combined data from three independent repeats). Neither $CaCl_2$ nor $SrCl_2$ were able to produce a statistically significant change in the levels of p-ERK (Figure 3.17).

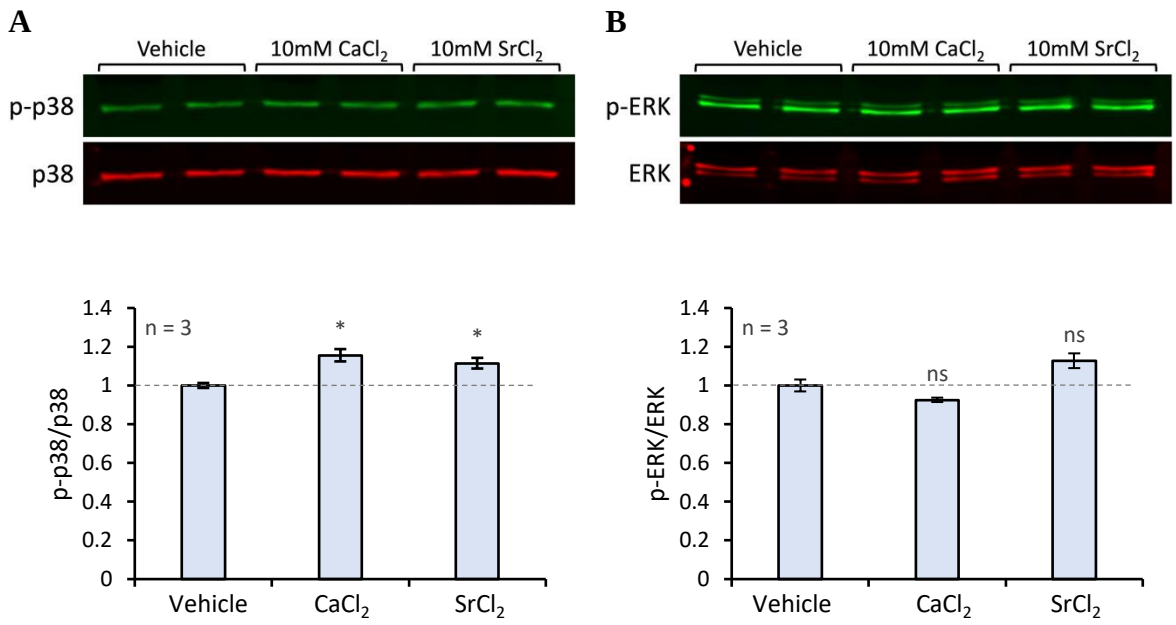


Figure 3.17: Effects of $CaCl_2$ and $SrCl_2$ treatment of T24 on phosphorylated p38 and ERK1/2. T24 were treated with media containing 10 mM $CaCl_2$, 10 mM $SrCl_2$, or an equivalent volume of vehicle ($H_2O$) for 10 minutes. Representative images of the western blots are shown. The graphs display the combined data from the three independent repeats (each with duplicates) as fold change compared to vehicle treatment. Error bars indicate standard error of the means. T24 treated with $CaCl_2$, and $SrCl_2$, showed a small but statistically significant increase in phosphorylated p38 (A), but no significant change in the levels of phosphorylated ERK1/2 (B). Statistical significance was determined using Bonferroni corrected P-values; *P < 0.025; calculated using an unpaired, two tailed t-test.

Failing to reproduce the substantial increase in p-p38 or p-ERK observed in previous studies involving the stimulation of CaSR (67,68,98,154,155), possible differences in the methodology were considered. Several studies had cultured their cells without serum overnight prior to the calcium or strontium treatment (67,68,98). This was thought to control the calcium levels in the media, as well as the phosphate levels. Phosphate had been shown to act as a non-competitive antagonist of CaSR (156) and therefore could have suppressed the response to stimulation with calcium and strontium. Hence, serum-deprivation was pursued.

The experimental procedure was identical to the above, except that the cells were seeded in media without serum supplementation and the treatment media with calcium or strontium was also without serum. Figure 3.18 shows the results combined from three independent repeats. Neither calcium nor strontium were able to produce a statistically significant change in the levels of phosphorylated p38 or ERK1/2 in serum deprived T24 cells.

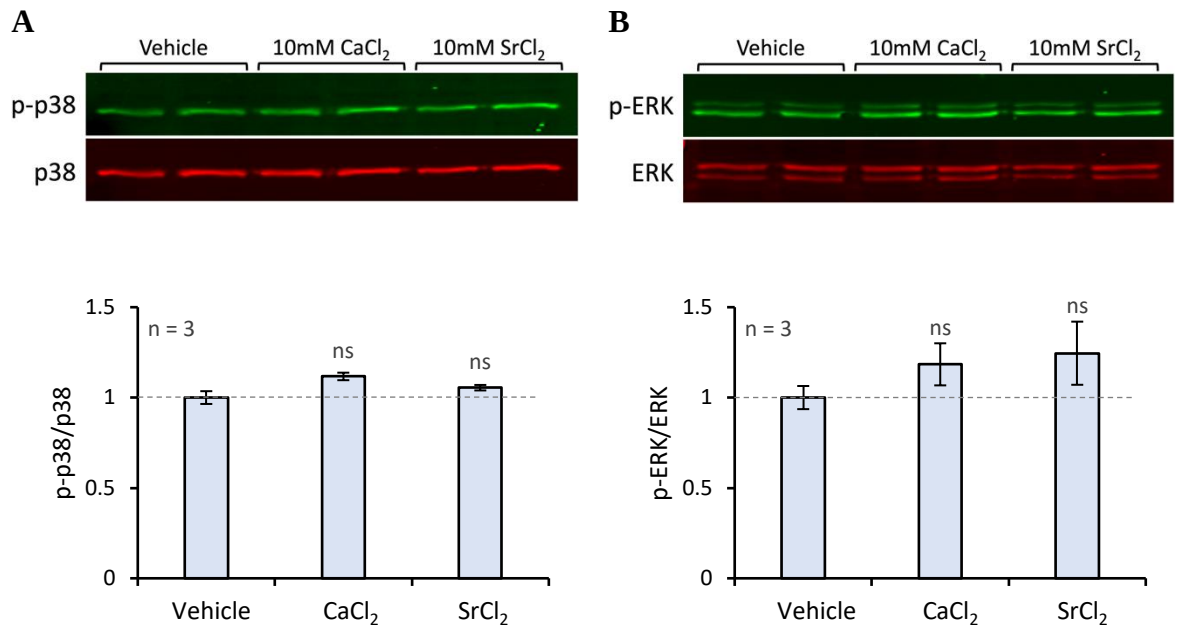


Figure 3.18: Effects of $CaCl_2$ and $SrCl_2$ treatment of serum deprived T24 on phosphorylated p38 and ERK1/2. T24 were treated with media containing 10 mM $CaCl_2$, 10 mM $SrCl_2$, or an equivalent volume of vehicle ($H_2O$) for 10 minutes. Representative images of the western blots are shown. The graphs display the combined data from the three independent repeats (each with duplicates) as fold change compared to vehicle treatment. Error bars indicate standard error of the means. T24 treated with $CaCl_2$, and $SrCl_2$, did not show any statistically significant change in phosphorylated p38 (A), or phosphorylated ERK1/2 (B). Statistical significance was determined using Bonferroni corrected P-values; *P < 0.025; calculated using an unpaired, two tailed t-test.

While an increase in phosphorylated p38 was observed following treatment of T24 cells (not serum deprived) with calcium and strontium, this was very mild in comparison to findings from previous studies (154,155). This effect was judged to be too small to be able to show any clear effects from modulation of components of this signaling pathway. Hence, the line of work investigating the pathway linking CaSR with FLNA was unable to be continued.

## 3.3 Summary of findings

The first approach utilised *in vitro* models of osteoblasts to investigate the effects of the FLNA variant responsible for DCD. I demonstrated that the differentiation of MC3T3-E1 could be monitored by measuring the expression levels of *Sp7* and *Runx2*. MC3T3-E1 were derived from mice and it was found that the wild type *Flna* sequence in mice, and other rodent species, contained the equivalent of the recurrent human disease variant responsible for DCD

(NM_001110556.1:c.5217G>A). This variant causes mis-splicing of *FLNA* in humans, but no such effect was apparent in a publicly available mouse development RNA-seq dataset that I investigated. By comparing the nucleotide sequences of *Flna* in rodents to that from human, I was able to identify twelve nucleotide changes that could be preventing mis-splicing of *Flna* in the presence of the human disease variant. A human osteosarcoma cell line, U2OS, was investigated for its ability to produce mineralized matrix. It was found that culture in differentiation media for twenty days was sufficient for U2OS to produce calcified nodules. Subsequently, AONs were used to introduce the mis-splicing event into these two cell lines. However, in MC3T3-E1, the mis-splicing of *Flna* resulted in the removal of 132 nucleotides from the end of the exon rather than the expected 48 nucleotides that is removed in DCD. Meanwhile, no detectable mis-splicing was observed in human U2OS cells following transfections with the AONs. This led to the development of plasmid constructs that were designed to knock down endogenous *Flna* and replace it with DCD-FLNA. Because a satisfactory transfection efficiency could not be achieved, no clear results were obtained.

The second approach aimed to investigate the hypothesis that DCD-FLNA dysregulates the signaling pathways downstream of CaSR to induce premature osteoblastic differentiation. RT-PCR was used to determine the expression of CaSR at the mRNA level. *CASR* expression was detected in cDNA from mouse bone but not in two osteoblastic cell lines, MC3T3-E1 and U2OS. *CASR* expression was however, detected in T24 (a cell line derived from urinary bladder transitional cell carcinoma) and thus this cell line was used for subsequent experiments. Calcium and strontium stimulation of T24 led to increased activation of p38, as determined by western blotting, but no changes in ERK1/2 activation was observed.

# Chapter 4: Discussion

# Chapter 4 Discussion

## 4.1 Overview

In the previous chapter, the utility of MC3T3-E1 and U2OS as *in vitro* model of osteoblasts was explored, and this work has highlighted some of the challenges surrounding the study of bone diseases. Attempts to reproduce the DCD mis-splicing event and the analysis of the nucleotide sequences in this region has uncovered the putative factors that may be influencing the splicing of *FLNA* at this site. Meanwhile, investigations into the possible role of CaSR in the pathogenesis of DCD has led to a shift in the hypothesis to include the involvement of cell types other than osteoblasts in the development of the skeletal abnormalities in this disease.

## 4.2 Developing an *in vitro* model of DCD

### 4.2.1 Modelling of diseases of bone

In this work, the MC3T3-E1 cell line was chosen as an *in vitro* model of osteoblasts to study the effects of DCD-FLNA. MC3T3-E1 originate from newborn mouse calvaria (130), and are commonly used for studying osteoblastic differentiation. Many studies monitor the progress of osteoblastic differentiation through the measurement of expression of genes involved in differentiation and mineralisation (157–159).

I conducted a differentiation assay to confirm the utility of three commonly used genes (*Sp7*, *Runx2*, *Col1a1*) as markers of osteoblastic differentiation in the MC3T3-E1 cells. A statistically significant increase in the expression of the two transcription factors, *Sp7* and *Runx2*, was observed from day two in differentiation media. These results are consistent with previous reports looking at osteoblastic differentiation in various cells, including MC3T3-E1, mesenchymal stem cells (MSCs), and induced pluripotent cells (iPSCs) (159–161). Since the

changes in gene expression levels were detectable at a relatively early time point, these markers would be useful in investigating how DCD-FLNA might affect the early stages of osteoblastic differentiation.

Interestingly, I was unable to show a significant increase in *Col1a1* over the six days of MC3T3-E1 differentiation. I did, however, see an increasing trend over this period which could simply mean that the duration of treatment was too short, or that the statistical power was insufficient for the effect size.

A recent study by Hwang and Horton (162) has brought into question the validity of MC3T3-E1 as an osteoblast model. They found that the overall gene expression pattern in differentiating MC3T3-E1 was different to that in differentiating primary calvarial osteoblasts (isolated from six-week-old female mice) (162). For instance, *Sp7* was found to be upregulated in MC3T3-E1 subclone 4, as confirmed in my experiment, but not in the primary osteoblasts (162). MC3T3-E1 are likely to have diverged from the osteoblasts from which they were derived, during the processes of spontaneous immortalisation and prolonged *in vitro* culture. However, the observations by Hwang and Horton (162) could have also been influenced by the heterogeneous nature of primary cells, which usually have some level of contamination by other cell lineages and have a mixture of osteoblasts at various stages of maturation (163). Consequently, experiments using primary cells can hold a lot of variability (163), and thus, immortalised cell lines are often preferred over primary cells despite the known differences in behaviour to normal osteoblasts.

Among the established immortalised cell lines, MC3T3-E1 are considered to be the best model of osteoblasts (164), but the differences between mice and humans generated the need for human-derived options to be explored for this project. Cell lines derived from human osteosarcoma such as U2OS are commonly used in studies investigating osteoblastic function

(164). As briefly described in section 3.1.5, osteosarcoma is a type of bone cancer originating from MSCs that have lost the ability to differentiate at some stage following commitment to the osteoblast lineage (144). Some reports have questioned the utility of U2OS as an osteoblast model (145,146); however, I was able to demonstrate that U2OS can be stimulated to produce mineralised matrix following treatment with differentiation media for twenty days – similar to another study showing positive staining with Alizarin Red S after four weeks (165).

This level of mineralisation was, however, quite low compared to other cell lines that have been used to model osteoblasts (164), and this suggested that U2OS are slow to produce mineralised matrix. There are at least two possible explanations for this. Firstly, U2OS are said to represent a very early stage of osteoblast (145) and therefore they may require a long time to differentiate before they can begin to lay down the mineralised matrix. Alternatively, U2OS may have completely lost the ability to differentiate and instead secrete the mineralised matrix very slowly in their original state. One study found that U2OS cultured in differentiation media showed an increase in the expression of some but not all osteoblast markers, and suggested that this was due to partial and not terminal differentiation (165). U2OS exhibit behaviours different to the osteoprogenitors they originated from, probably due to the accumulated genetic and epigenetic changes typical of cancers (166,167). But because U2OS still have the capacity to deposit mineralised matrix, they would still be useful for investigating the effects of DCD-FLNA on mineralisation. However, my interest was in how DCD-FLNA affects normal osteoblastic differentiation and therefore U2OS may be less suitable for this experiment.

The two immortalised cell lines investigated in this work each have their own limitations – interspecific differences and cancerous changes. Other osteoblast models that could avoid these issues include: primary osteoblasts isolated from human tissues, human mesenchymal stem cells (hMSCs), induced pluripotent cells (iPSCs) or transdifferentiation of readily accessible

human cells such as dermal fibroblasts (164,168,169). However, these also have limitations including poor accessibility, complex differentiation protocols, and/or variability according to donor characteristics and the methodology used (163,169,170). The variable nature of these options lead to issues around reproducibility, which can complicate the interpretation of results compared to when established immortalised cell lines are used.

Note that only *in vitro* cultures of osteoblasts have been discussed here. The role of other cells residing in bone such as osteoclasts and osteocytes, and the intercommunications between such cells is undeniably important (171). Investigating the effect of a genetic variant on bone development may therefore be better conducted in co-cultures, or even using animal models. However, isolated cultures of osteoblast models still retain value for testing specific hypotheses, even with the drawbacks discussed in this section, so long as careful consideration is made in the experimental design. It is through such studies that complex intracellular signaling pathways can be disentangled and understood.

### 4.2.2 Mis-splicing of *FLNA* in DCD

Since DCD is caused by a mis-splicing event, the utility of AONs in reproducing this event was investigated. AONs transfected into MC3T3-E1 induced a different mis-splicing event to that in DCD, presumably due to interspecific differences (discussed in section 4.2.3). Meanwhile, the transfection of similarly designed AONs into human U2OS and fibroblast cells did not cause any mis-splicing. This latter observation was surprising because it was assumed that this splice site was weak, given that two different variants outside the splice donor dinucleotide have been shown to cause the mis-splicing event responsible for DCD (16).

The choice of the target for the AONs is likely to be responsible for the lack of effect observed in human cell lines. The AONs were designed to hybridise to the sites of the two DCD variants

in *FLNA*, so that the exact mis-splicing event would preferentially be induced over some other mis-splicing event. This did however, mean that the target sites (in human but not mouse) were not ideal as it had a high GC content (75%; ideally 40-50%) and contained stretches of six and four consecutive guanine bases (the recommendation was to avoid three or more consecutive guanines or cytosines) (125). Consequently, strong secondary structures that hinder AON binding were likely to be present in the pre-mRNA molecule at this site. One such structure could be a G-quadruplex, although the sequence does differ slightly from the canonical G-quadruplex sequence (172,173). Note that in the mouse, the intronic sequence does not contain these stretches of guanine nucleotides. This may provide an explanation as to why similarly designed AONs could readily hybridise to their target and induce mis-splicing when transfected into MC3T3-E1 but not in human cells.

The secondary structure in the human sequence might not only be hindering the binding of AONs but also the binding of splice factors. This would impair the assembly of the spliceosome at this site. This could explain why this splice site appears to be weak in humans and is vulnerable to mutations that further weaken this site to cause mis-splicing in DCD. Further exploration of this idea would involve validating the presence of secondary structures using experimental approaches such as SHAPE-seq, or immunoprecipitation with selective G-quadruplex binding proteins (174,175).

### 4.2.3 Regulation of *Flna* splicing in mice and other rodents

In the original study that identified the recurrent variant responsible for DCD, there was a brief mention that this nucleotide position was not conserved in rodents (16). However, they did not specify how the rodent sequence differed from human, and therefore the finding that rodents had the equivalent of the recurrent mutation was unexpected. While this variant causes mis-splicing in humans (16), I observed no such effect in the mouse developmental RNA-seq

dataset from the Wold lab, Caltech (139). This is presumably indicative of differences in the regulation of splicing at this site between mice and humans, which prevent mis-splicing in mice.

Within the few mis-splicing events identified as noise in the RNA-seq dataset, the event analogous to that responsible for DCD (utilising the -48 cryptic splice site) was least represented. This finding suggests that the -48 cryptic splice site is weaker than the other sites in mice (176), which is in contrast to humans, where the -48 site is presumably the strongest cryptic splice site as it is this one that is used when the original 5' splice site is weakened (by mutations in DCD). In support of this claim, disrupting the original 5' splice site in murine MC3T3-E1 with AONs, led to the use of the -132 cryptic splice site rather than the -48 site. It is possible that this latter observation was an artefact of the mechanism of splice site disruption (i.e. altered secondary structure also interferes with the use of the -48 cryptic splice site located closer to the original site); however, the -48 splice site being weak in the mouse is a more likely explanation given that it is consistent with what was observed in the RNA-seq dataset.

There may be one or more splicing regulatory factors that differ between humans and mice/rodents to account for the two observations mentioned above (i.e. normal splicing in the presence of the 'disease allele' in rodents, and differences in strength of the cryptic splice sites between mouse and human). Earlier, I discussed the possibility that secondary structures in the intron was responsible for making this splice site weak in humans but not rodents. However, there could also be other factors involved. The regulation of splicing is achieved by the combined effects of a wide range of factors which include: DNA methylation, chromatin structure, local secondary structure of the pre-mRNA, transcription elongation rate, motifs in the sequence for the binding of splice factors, and the expression levels of various proteins and RNA involved in splicing (177). Broadly speaking, these factors can be organised into two groups (178). The first group is comprised of factors that are related to the nucleotide sequence

and are termed *cis*-acting features. The second group includes factors which bind the nucleotide sequence at or near the region of interest – termed *trans*-acting factors.

Most interspecific differences in splicing regulation have been found to be *cis*-directed (179,180). Hence, possible *cis*-acting features that could be responsible for the differences between mice and humans, were investigated using a phylogenetic approach. Comparison of the nucleotide sequences from nine rodents with that from human revealed that there were twelve changes in *cis* with the G>A transition. This might not be a complete list of the possible *cis*-acting features responsible for the differences between mice and humans in the regulation of splicing at this site. Firstly, only the exon and intron involved in this splice site was inspected. Although most *cis*-acting features are located relatively close to the splice site concerned, there could also be relevant factors outside this region (181). Secondly, nucleotide changes were included only if they were conserved among the rodents. The motifs that provide sequence specific binding sites for *trans*-acting splicing factors are degenerate (182,183), which means that changes that differ within rodents may still be important. However, given that the nucleotide position of the G>A transition is highly conserved over a wide range of vertebrate species, I hypothesised that the *cis*-acting feature(s) protecting this site from mis-splicing was linked with the G>A transition, and therefore be identical within this group of rodents.

Minigene splicing assays could be used to distinguish the changes that affect splicing from those that are simply a result of genetic drift and not of functional effect. This would first involve the construction of a plasmid containing the human sequence of several exons and introns flanking the splice site of interest. The recurrent DCD variant (G>A at the end of exon 31) would be inserted into this construct along with one or more of the changes identified in Figure 3.5 to see whether any (combination) of these features could rescue the mis-splicing event. This work was in fact initiated during the course of the project but technical difficulties

in plasmid construction prevented this from being completed. Identification of the precise features involved in splice site recognition could help contribute to our understanding of the regulation of splicing. This knowledge can be applied to other splice sites to aid the interpretation of genetic variants for diagnostic purposes or to help identify targets for therapeutic interventions which involve the modulation of splicing.

## 4.3 CaSR in the pathogenesis of DCD

### 4.3.1 Expression of CaSR at the mRNA level

This second line of work aimed to explore the hypothesis that the skeletal manifestations of DCD arise through the disruption of a proposed pathway that involves FLNA and CaSR (see Introduction section 1.4.4 and Figure 1.6). Firstly, the expression of CaSR at the transcript level was investigated using RT-PCR. Consistent with previous literature (100,184), expression of *Casr* could be demonstrated in mouse bone using this method, thus supporting the possible role of CaSR in bone.

The expression of *Casr*, however, could not be detected in the osteoblastic MC3T3-E1 cell line using the same method. RT-PCR was repeated on MC3T3-E1 that had been cultured in differentiation media for up to twenty-five days, but expression of *Casr* could not be detected in any of the time-points examined. This suggests that *Casr* is not expressed at any stage of differentiation between pre-osteoblast and mature osteoblast.

However, rather than the complete absence of *Casr*, it is more likely that this finding reflects very low expression levels which RT-PCR lacks the sensitivity to detect. Indeed, the original study that demonstrated the expression of *Casr* in MC3T3-E1, reported difficulties in amplifying *Casr* using ordinary Taq DNA polymerase (110). Using qPCR, Yasukawa et al.

(112) showed that the mRNA levels of *Casr* in MC3T3-E1 was a hundred-thousand times lower than that of *Gapdh*, or a thousand times lower than *Runx2*. This low level of expression is probably responsible for the mixed reports in the literature regarding the expression of CaSR in this cell line (110,112,150,151).

Low expression of *CASR* also appears to be a feature of human cell lines and is likely responsible for the supposed technical difficulties encountered in attempts to amplify *CASR* using RT-PCR. None of the 69 immortalised human cell lines in the Human Protein Atlas (http://www.proteinatlas.org) (153) show very high *CASR* expression levels when compared to the data from tissue or single cell RNA-seq present in the same database.

The finding that *CASR/Casr* expression could be detected from mouse bone (represents mostly osteocytes (171)) but not in two osteoblastic cell lines (MC3T3-E1 and U2OS) might lead to the conclusion that CaSR expression is of greater importance in osteocytes than osteoblasts. However, it is also possible that the transcript levels of *CASR/Casr* in MC3T3-E1 and U2OS do not accurately reflect that of osteoblasts *in vivo*. Low expression of *CASR/Casr* in these cells could have been due to the *in vitro* culture conditions or perhaps is a feature of all immortalised cell lines. It would be prudent to investigate this further, either by comparing the expression of *Casr* between osteocytes and osteoblasts *in vitro* (e.g. murine osteocytic MLO-Y4 cell line vs murine osteoblastic MC3T3-E1) or *in vivo* using single cell RNA-seq.

The original motive for this line of work was to identify a cell line, preferably exhibiting osteoblastic behaviour that could serve as a workhorse for the investigation of the CaSR signaling pathway. Hence, my interest was in the expression of CaSR at the protein level rather than at the transcript level. While transcript levels are commonly used as a proxy for the protein expression, the variability in the RNA-to-protein (RTP) ratios between different genes can make this an inaccurate estimate (185). The study by Yasukawa et al. (112) found that, while

the expression of *Casr* in MC3T3-E1 was substantially lower than that of *Runx2*, the proteins level of CaSR was actually greater than that of Runx2. To account for this observation, CaSR must have a high RTP ratio. This could be mediated by high translational efficiency and/or high protein stability (185). No studies have looked into these factors, although, one study did describe CaSR to be a relatively stable with a protein half-life of ~8h (186). Given that the level of CaSR in MC3T3-E1 has been demonstrated to be functionally relevant in several different studies (112,120,187), it is possible there is functional CaSR in those cell lines that I failed to demonstrate expression using RT-PCR. Methods to detect the protein directly such as western blotting, immunocytochemistry, or enzyme-linked immunosorbent assays (ELISA), should be pursued in the future to investigate this. This has highlighted the importance of using multiple detection methods in confirming the expression of a specified protein in tissues or cultured cells.

### 4.3.2 CaSR-mediated MAPK activation in T24 cells

Following the identification of the T24 cell line as one that expresses CaSR, experiments to investigate CaSR-mediated activation of MAPK signaling was initiated. I was able to demonstrate a slight but significant increase in phosphorylated p38 following stimulation with calcium and strontium, but no change in phosphorylated ERK1/2 was observed. The effect sizes were smaller than what had previously been reported in similar experiments (154,155,188,189). There could be several factors that are contributing towards the observed discrepancy.

Firstly, low levels of CaSR in T24 cells may be producing an accordingly small response to calcium stimulation (190). I did not collect data on the levels of CaSR protein in this cell line and therefore it is unclear whether this could be responsible (see previous section for discussion on the levels of expression of CaSR at the protein and transcript levels).

Secondly, technical issues or insufficient optimisation could be at work here given the wide range of differences in the methods utilised in previous studies (151,154,155,187–189,191). For instance, the concentration of calcium used to stimulate CaSR ranges from 2 mM to 10 mM (155,187), and the duration of treatment from 5 minutes up to 2 hours (151,191). The conditions required to elicit this transient response appears to vary substantially between cell lines, which is expected given that different tissues have their own specific response to a given stimulus. The physiological role of CaSR in transitional epithelium, from which the T24 were derived, remains unclear (192). Thus, downstream signaling pathways other than p38 or ERK1/2 might instead be activated following stimulation of CaSR in T24 cells.

The cellular context is clearly an important determinant of the intracellular signaling pathways that are activated upon stimulation of a given receptor. As discussed in the introduction, the relationship between CaSR and FLNA has shown to vary between different cell lines. This might account for the apparent absence of calcium and parathyroid hormone abnormalities in individuals with DCD despite this being a major feature of disorders arising from pathogenic variants in CaSR (7,88). Future work aiming to elucidate the relationship between CaSR and FLNA in the cells of bone and comparisons with that in the parathyroid and kidney may be able to confirm this hypothesis.

### 4.3.3 Reconsideration of the role of CaSR in DCD

At the outset of this project, I hypothesised that the dysregulation of CaSR signaling occurred in osteoblasts to produce the abnormal bone phenotype. However, the finding of *Casr* expression in mouse bone, alongside the apparent absence of expression in two osteoblastic cell lines, has introduced the possibility that osteocytes may have a role in the pathogenesis of DCD. While the role of CaSR in osteoblasts have been extensively studied, this has not been the case for osteocytes and as such, the role of CaSR in this cell type remains elusive. It might therefore

be reasonable to propose a hypothesis where DCD-FLNA activates pathways downstream of CaSR to cause premature differentiation of osteoblasts into osteocytes. This could be investigated in a similar way to the differentiation assay conducted for the MC3T3-E1, but instead looking at the expression levels of genes specific to osteocytes.

Other Mendelian diseases of bone attributed to osteocytic dysfunction, do however have a different skeletal phenotype compared to that of DCD. For example, sclerosteosis and van Buchem disease exhibit thickening of the skull bones, which is not seen in DCD (193). Until recently, the study of osteocytes has largely been neglected because of the difficulties associated with isolation and culture of these cells (194). With the rapidly expanding understanding of the role of the osteocyte in bone, it is expected that further skeletal phenotypes will become associated with osteocyte dysfunction and perhaps the features observed in DCD may fit in this phenotype.

## 4.4 Clinical applications of findings

The first part of my project highlighted some of the key challenges faced in studying this disease, including the issues associated with modelling skeletal diseases *in vitro*. I was not able to obtain any clear results regarding what effects DCD-FLNA might have on osteoblasts due to technical difficulties with the plasmid transfection procedure. Other methods of transfection (e.g. electroporation) or gene editing techniques to introduce the disease variant could be explored in future work. Nevertheless, there were some discoveries surrounding the factors influencing splicing at this site which could lead on to the development of therapeutic interventions that target this process.

With regards to treatment and management of DCD, most of the manifestations are congenital and therefore not easily altered; however, the digital fibromata that develop after birth may

prove to be a target. Currently, there are no effective treatments for these fibromata. Intralesional corticosteroids and cryotherapy have been found to be ineffective (18), and surgical resection has been associated with recurrence and damage to the surrounding tissues (10). Although these fibromata do eventually regress with time, they can be debilitating while they are present and can cause permanent contractures in the most severe cases (10). As such, the development of prophylactic or therapeutic interventions that decrease mis-splicing to prevent or suppress growth of these lesions would undoubtedly be beneficial for these individuals.

By contrast, introducing this mis-splicing event into individuals not affected by DCD could also prove to have a therapeutic application. While more work is needed to understand the exact effects of DCD-FLNA on bone cells, it appears that the skeletal manifestations in DCD are hyperostotic. Therefore, it may be possible unleash the osteogenic potential of the mis-spliced form of *FLNA* in a controlled manner in settings where this may be beneficial, for example, to accelerate fracture healing.

Meanwhile, the second part of my project, which focused on the possible involvement of CaSR in the pathogenesis of DCD, has laid a foundation upon which this hypothesis could be investigated further. Exploration of the relationship between CaSR and FLNA may uncover a signaling pathway within which targets for therapeutic interventions may lie. Already, CaSR has been the target for the development of therapeutic approaches to improve bone anabolism (184). Strontium ranelate has been used to treat postmenopausal osteoporosis; however, it is no longer indicated for this condition in New Zealand due to the increased cardiovascular risk (195). More in depth studies of pathways specific to osteoblasts or osteocytes might allow better targets to be identified.

## 4.5 Future perspectives

The study of DCD is complicated by the X-linked nature of this disease. Readily accessible patient cells such as skin fibroblasts and peripheral blood leucocytes rarely ever express the disease allele due to the extremely skewed X-inactivation patterns (9,16). Meanwhile, the presence of skewing in other tissues is less clear. In the atypical case of DCD introduced in section 1.2.3, X-inactivation was highly skewed to favour the expression of the normal allele in affected lung tissue but not in the affected heart tissue (which had ~60% expression of disease allele). Evidently, the selection against cells expressing the disease allele begins after the development of abnormalities in affected organs. When exactly and why the skewing becomes established is unclear. It is possible that affected cells have decreased proliferative capacity, although, this hypothesis conflicts with the observation of digital fibromata (tumour growth) as a manifestation of this disease. Regardless, whether skewing of X-inactivation is present in bone tissue is currently unknown, since such tissues have not been studied due to inaccessibility.

Animal models would be useful for the study of this disorder. But note that rats and mice already have the equivalent of the recurrent DCD variant, as discussed earlier, and therefore simply introducing the nucleotide variant into these models is not possible. Instead, a 'knock-in' model, which involves replacing the murine *Flna* locus with the human *FLNA* sequence containing the DCD variant, could be used (196). There are some caveats around using this approach, but the validity of this model could be confirmed by analysing the mouse phenotypes and comparing them to the phenotypes observed in individuals with DCD.

Ideally, the study of hemizygous males would allow a clear signal to be obtained, although, conditional alleles would need to be used given that this variant is presumably embryonic lethal. Alternatively, female mice could be investigated using single cell RNA-seq, a technique that

could be used to sort cells based on whether the disease allele is transcriptionally active or not (197). This could be used to gain some insight into the transcriptomic effects of DCD-FLNA in various cell types.

Embryonic tissue would be of interest given that this is when the disease is active in causing abnormal development of affected organs. While bone cells such as osteoblasts, osteocytes, and osteoclasts would be an obvious choice to investigate, it may also be of interest to look at embryonic parathyroid, given the proposed hypothesis of CaSR involvement in the pathogenesis of DCD.

Presumably, individuals affected with DCD do not have abnormal serum calcium or PTH levels since none of the clinical reports mention these, bar one which stated that routine blood examinations were unremarkable (7). However, we cannot rule out the possibility that calcium and PTH abnormalities exist prenatally which is when the abnormal skeletal development begins. As mentioned in the introduction, the skeletal manifestations of DCD differ somewhat from the allelic OPDSD conditions. Prenatal PTH abnormalities could be a mechanism unique to DCD, that contributes to the skeletal abnormalities.

## 4.6 Conclusions

The main goal of this work was to investigate the pathomechanisms that underlie the skeletal manifestations of DCD. The first part of this work uncovered some of the putative factors influencing the mis-splicing of *FLNA* in DCD. These factors can be explored further to better understand how the mis-splicing of *FLNA* might be manipulated. Meanwhile, investigations into the possible involvement of CaSR in this mechanism, revealed the unexpectedly low expression of CaSR mRNA in osteoblastic cell lines and the comparatively higher expression in osteocytes. The role of CaSR in the osteocyte is currently unclear and is something that

should be explored in future work. Steps taken to understand the of the pathogenesis of this rare skeletal dysplasia will lead to a greater understanding of bone biology and is hoped that it could aid the development of more targeted treatment and management strategies for various disorders involving bone.

# References

# References


1. Su N, Yang J, Xie Y, Du X, Chen H, Zhou H, et al. Bone function, dysfunction and its role in diseases including critical illness. Int J Biol Sci. 2019;15(4):776.
2. Osteoporosis New Zealand: Osteoporosis & fractures [Internet]. [cited 2020 Sep 19]. Available from: https://osteoporosis.org.nz/osteoporosis-fractures/
3. Li Z, Xie Y, Xiao Q, Wang L. Terminal osseous dysplasia with pigmentary defects in a Chinese girl with the FLNA mutation: A case report and published work review. J Dermatol. 2020/01/11. 2020;47(3):295–9.
4. Gorlin RJ, Cohen MM, Hennekam RCM. Syndromes of the Head and Neck. Oxford University Press; 2001. (Oxford monographs on medical genetics).
5. Bloem JJ, Vuzevski VD, Huffstadt AJ. Recurring digital fibroma of infancy. J Bone Jt Surg (British Vol. 1974/11/01. 1974;56-b(4):746–51.
6. Dabney KW, MacEwen GD, Davis NE. Recurring digital fibrous tumor of childhood: case report with long-term follow-up and review of the literature. J Pediatr Orthop. 1986/09/01. 1986;6(5):612–7.
7. Horii E, Sugiura Y, Nakamura R. A syndrome of digital fibromas, facial pigmentary dysplasia, and metacarpal and metatarsal disorganization. Am J Med Genet [Internet]. 1998;80(1):1–5. Available from: https://onlinelibrary.wiley.com/doi/abs/10.1002/%28SICI%291096-8628%2819981102%2980%3A1%3C1%3A%3AAID-AJMG1%3E3.0.CO%3B2-8
8. Bacino CA, Stockton DW, Sierra RA, Heilstedt HA, Lewandowski R, Van den Veyver IB. Terminal osseous dysplasia and pigmentary defects: clinical characterization of a novel male lethal X-linked syndrome. Am J Med Genet. 2000/09/13. 2000;94(2):102–12.
9. Zhang W, Amir R, Stockton DW, Van den Veyver IB, Bacino CA, Zoghbi HY. Terminal Osseous Dysplasia with Pigmentary Defects Maps to Human Chromosome Xq27.3-Xqter. Am J Hum Genet [Internet]. 2000;66(4):1461–4. Available from: http://www.sciencedirect.com/science/article/pii/S0002929707601773
10. Breuning MH, Oranje AP, Langemeijer RA, Hovius SE, Diepstraten AF, den Hollander JC, et al. Recurrent digital fibroma, focal dermal hypoplasia, and limb malformations. Am J Med Genet. 2000/09/13. 2000;94(2):91–101.
11. Lin BP, Lin MI, Berlocher WC. Clinical manifestations of terminal osseous dysplasia and pigmentary defects in a young girl. Oral Surgery, Oral Med Oral Pathol Oral Radiol Endod. 2003/05/10. 2003;95(5):607–13.
12. Drut R, Pedemonte L, Rositto A. Noninclusion-body infantile digital fibromatosis: a lesion heralding terminal osseous dysplasia and pigmentary defects syndrome. Int J Surg Pathol. 2005/05/03. 2005;13(2):181–4.
13. Baroncini A, Castelluccio P, Morleo M, Soli F, Franco B. Terminal osseous dysplasia with pigmentary defects: clinical description of a new family. Am J Med Genet A. 2006/12/08. 2007;143a(1):51–7.
14. Izadpanah A, Hogeling M, Buka RL, Eichenfield LF, Bird LM. Digitocutaneous dysplasia. J Am Acad Dermatol [Internet]. 2007;56(2, Supplement):S6–9. Available

from: http://www.sciencedirect.com/science/article/pii/S019096220601187X

15. Kokitsu-Nakata NM, Antunes LF, Guion-Almeida ML. Terminal osseous dysplasia and pigmentary defects in a Brazilian girl. Am J Med Genet A. 2008/09/17. 2008;146a(20):2698–700.

16. Sun Y, Almomani R, Aten E, Celli J, Van der Heijden J, Venselaar H, et al. Terminal osseous dysplasia is caused by a single recurrent mutation in the FLNA gene. Am J Hum Genet. 2010;87(1):146–53.

17. Brunetti-Pierri N, Lachman R, Lee K, Leal SM, Piccolo P, Van den Veyver IB, et al. Terminal osseous dysplasia with pigmentary defects (TODPD): Follow-up of the first reported family, characterization of the radiological phenotype, and refinement of the linkage region. Am J Med Genet Part A. 2010;152(7):1825–31.

18. González MC, López LMP, Iglesia DG de la, Zurriaga CR, Sampol LM, Enseñat AG. Diagnosis and Treatment of Digitocutaneous Dysplasia, a Rare Infantile Digital Fibromatosis: A Case Report. HAND [Internet]. 2013 Mar 2;8(4):473–8. Available from: https://doi.org/10.1007/s11552-013-9515-8

19. Brunetti-Pierri N, Torrado M, Fernandez M del C, Tello AM, Arberas CL, Cardinale A, et al. Terminal osseous dysplasia with pigmentary defects (TODPD) due to a recurrent filamin A (FLNA) mutation. Mol Genet genomic Med. 2014;2(6):467–71.

20. Connor CJ, Shchelochkov OA, Ciliberto H. Anetoderma in a patient with terminal osseous dysplasia with pigmentary defects. Am J Med Genet A. 2015/06/11. 2015;167a(10):2459–62.

21. Bhabha FK, Walsh M, Orchard D, Savarirayan R. Terminal osseous dysplasia with pigmentary defects; Case and brief review of filamin A-related disorders. Australas J Dermatol. 2015/06/11. 2016;57(4):312–5.

22. Gontijo JR V, dos Santos WF, Gontijo B, Happle R. Terminal osseous dysplasia presenting with intracytoplasmic inclusion bodies in digital fibromas. Pediatr Dermatol [Internet]. 2018;35(6):e353–6. Available from: https://onlinelibrary.wiley.com/doi/abs/10.1111/pde.13656

23. Azakli H, Akkaya AD, Aygun MS, Demirkesen C, Eraslan S, Kayserili H. Terminal osseous dysplasia with pigmentary defects (TODPD) in a Turkish girl with new skin findings. Am J Med Genet A [Internet]. 2018/12/19. 2019;179(1):123–9. Available from: https://onlinelibrary.wiley.com/doi/abs/10.1002/ajmg.a.60686

24. Marks E, Ewart M. Infantile digital fibroma: A rare fibromatosis. Arch Pathol Lab Med. 2016;140(10):1157–62.

25. Laskin WB, Miettinen M, Fetsch JF. Infantile Digital Fibroma/Fibromatosis: A Clinicopathologic and Immunohistochemical Study of 69 Tumors From 57 Patients With Long-term Follow-up. Am J Surg Pathol [Internet]. 2009;33(1). Available from: https://journals.lww.com/ajsp/Fulltext/2009/01000/Infantile_Digital_Fibroma_Fibromatosis__A.1.aspx

26. Lyon MF. Gene Action in the X-chromosome of the Mouse (Mus musculus L.). Nature [Internet]. 1961;190(4773):372–3. Available from: https://doi.org/10.1038/190372a0

27. Roca X, Olson AJ, Rao AR, Enerly E, Kristensen VN, Børresen-Dale A-L, et al. Features of 5′-splice-site efficiency derived from disease-causing mutations and comparative genomics. Genome Res. 2008;18(1):77–87.

28. Roca X, Krainer AR, Eperon IC. Pick one, but be quick: 5′ splice sites and the problems of too many choices. Genes Dev. 2013;27(2):129–44.

29. Burset M, Seledtsov IA, Solovyev V V. Analysis of canonical and non-canonical splice sites in mammalian genomes. Nucleic Acids Res. 2000;28(21):4364–75.

30. Wade EM, Halliday BJ, Jenkins ZA, O'Neill AC, Robertson SP. The X-linked filaminopathies: Synergistic insights from clinical and molecular analysis. Hum Mutat. 2020;(January).

31. Yates AD, Achuthan P, Akanni W, Allen JJ, Allen JJ, Alvarez-Jarreta J, et al. Ensembl 2020. Nucleic Acids Res. 2020;48(D1):D682–8.

32. Fox JW, Lamperti ED, Ekşioğlu YZ, Hong SE, Feng Y, Graham DA, et al. Mutations in filamin 1 prevent migration of cerebral cortical neurons in human periventricular heterotopia. Neuron. 1998;21(6):1315–25.

33. Gargiulo A, Auricchio R, Barone MV, Cotugno G, Reardon W, Milla PJ, et al. Filamin A is mutated in X-linked chronic idiopathic intestinal pseudo-obstruction with central nervous system involvement. Am J Hum Genet. 2007;80(4):751–8.

34. Kyndt F, Gueffet J-P, Probst V, Jaafar P, Legendre A, Le Bouffant F, et al. Mutations in the gene encoding filamin A as a cause for familial cardiac valvular dystrophy. Circulation. 2007;115(1):40.

35. Nurden P, Debili N, Coupry I, Bryckaert M, Youlyouz-Marfak I, Solé G, et al. Thrombocytopenia resulting from mutations in filamin A can be expressed as an isolated syndrome. Blood, J Am Soc Hematol. 2011;118(22):5928–37.

36. Parrini E, Rivas IL, Toral JF, Pucatti D, Giglio S, Mei D, et al. In-frame deletion in FLNA causing familial periventricular heterotopia with skeletal dysplasia in males. Am J Med Genet Part A. 2011;155(5):1140–6.

37. Zenker M, Rauch A, Winterpacht A, Tagariello A, Kraus C, Rupprecht T, et al. A dual phenotype of periventricular nodular heterotopia and frontometaphyseal dysplasia in one patient caused by a single FLNA mutation leading to two functionally different aberrant transcripts. Am J Hum Genet. 2004;74(4):731–7.

38. Sasaki E, Byrne AT, Phelan E, Cox DW, Reardon W. A review of filamin A mutations and associated interstitial lung disease. Eur J Pediatr. 2019;178(2):121–9.

39. Baldassarre M, Razinia Z, Burande CF, Lamsoul I, Lutz PG, Calderwood DA. Filamins regulate cell spreading and initiation of cell migration. PLoS One. 2009;4(11):e7830.

40. Glogauer M, Arora P, Chou D, Janmey PA, Downey GP, McCulloch CAG. The role of actin-binding protein 280 in integrin-dependent mechanoprotection. J Biol Chem. 1998;273(3):1689–98.

41. Shifrin Y, Arora PD, Ohta Y, Calderwood DA, McCulloch CA. The role of FilGAP-filamin A interactions in mechanoprotection. Mol Biol Cell. 2009;20(5):1269–79.

42. Yoshida N, Ogata T, Tanabe K, Li S, Nakazato M, Kohu K, et al. Filamin A-bound PEBP2β/CBFβ is retained in the cytoplasm and prevented from functioning as a partner of the Runx1 transcription factor. Mol Cell Biol. 2005;25(3):1003–12.

43. Ohta Y, Hartwig JH, Stossel TP. FilGAP, a Rho-and ROCK-regulated GAP for Rac binds filamin A to control actin remodelling. Nat Cell Biol. 2006;8(8):803–14.

44. Pentikäinen U, Ylänne J. The regulation mechanism for the auto-inhibition of binding of

human filamin A to integrin. J Mol Biol. 2009;393(3):644–57.

45. Cukier IH, Li Y, Lee JM. Cyclin B1/Cdk1 binds and phosphorylates Filamin A and regulates its ability to cross-link actin. FEBS Lett. 2007;581(8):1661–72.

46. Wang H-Y, Lee K-C, Pei Z, Khan A, Bakshi K, Burns LH. PTI-125 binds and reverses an altered conformation of filamin A to reduce Alzheimer's disease pathogenesis. Neurobiol Aging. 2017;55:99–114.

47. Loy CJ, Sim KS, Yong EL. Filamin-A fragment localizes to the nucleus to regulate androgen receptor and coactivator functions. Proc Natl Acad Sci. 2003;100(8):4562–7.

48. Gorlin JB, Yamin R, Egan S, Stewart M, Stossel TP, Kwiatkowski DJ, et al. Human endothelial actin-binding protein (ABP-280, nonmuscle filamin): a molecular leaf spring. J Cell Biol. 1990;111(3):1089–105.

49. van der Flier A, Sonnenberg A. Structural and functional aspects of filamins. Biochim Biophys Acta - Mol Cell Res [Internet]. 2001;1538(2):99–117. Available from: http://www.sciencedirect.com/science/article/pii/S0167488901000726

50. Nakamura F, Stossel TP, Hartwig JH. The filamins: organizers of cell structure and function. Cell Adh Migr. 2011;5(2):160–9.

51. Zhou A-X, Hartwig JH, Akyürek LM. Filamins in cell signaling, transcription and organ development. Trends Cell Biol. 2010;20(2):113–23.

52. Nakamura F, Osborn TM, Hartemink CA, Hartwig JH, Stossel TP. Structural basis of filamin A functions. J Cell Biol. 2007;179(5):1011–25.

53. Gardel ML, Nakamura F, Hartwig JH, Crocker JC, Stossel TP, Weitz DA. Prestressed F-actin networks cross-linked by hinged filamins replicate mechanical properties of cells. Proc Natl Acad Sci. 2006;103(6):1762–7.

54. Robertson SP, Jenkins ZA, Morgan T, Adès L, Aftimos S, Boute O, et al. Frontometaphyseal dysplasia: mutations in FLNA and phenotypic diversity. Am J Med Genet Part A. 2006;140(16):1726–36.

55. Tomizawa T, Tochio N, Koshiba S, Watanabe S, Harada T, Kigawa T, et al. Solution structure of the 15th Filamin domain from human Filamin-B [Internet]. 2006. Available from: https://www.rcsb.org/structure/2DMB

56. Zenker M, Nährlich L, Sticht H, Reis A, Horn D. Genotype–epigenotype–phenotype correlations in females with frontometaphyseal dysplasia. Am J Med Genet Part A. 2006;140(10):1069–73.

57. Atwal PS, Blease S, Braxton A, Graves J, He W, Person R, et al. Novel X-linked syndrome of cardiac valvulopathy, keloid scarring, and reduced joint mobility due to filamin A substitution G1576R. Am J Med Genet Part A. 2016;170(4):891–5.

58. Lah M, Niranjan T, Srikanth S, Holloway L, Schwartz CE, Wang T, et al. A distinct X-linked syndrome involving joint contractures, keloids, large optic cup-to-disc ratio, and renal stones results from a filamin A (FLNA) mutation. Am J Med Genet Part A. 2016;170(4):881–90.

59. Kircher P, Hermanns C, Nossek M, Drexler MK, Grosse R, Fischer M, et al. Filamin A interacts with the coactivator MKL1 to promote the activity of the transcription factor SRF and cell migration. Sci Signal. 2015;8(402):1–10.

60. Berry FB, O'Neill MA, Coca-Prados M, Walter MA. FOXC1 Transcriptional Regulatory

Activity Is Impaired by PBX1 in a Filamin A-Mediated Manner. Mol Cell Biol. 2005;25(4):1415–24.

61. Smith L, Litman P, Kohli E, Amick J, Page RC, Misra S, et al. RACK1 interacts with filamin-A to regulate plasma membrane levels of the cystic fibrosis transmembrane conductance regulator. Am J Physiol - Cell Physiol. 2013;305(1):111–20.

62. Playford MP, Nurminen E, Pentikäinen OT, Milgram SL, Hartwig JH, Stossel TP, et al. Cystic fibrosis transmembrane conductance regulator interacts with multiple immunoglobulin domains of filamin A. J Biol Chem. 2010;285(22):17156–65.

63. Smith L, Page RC, Xu Z, Kohli E, Litman P, Nix JC, et al. Biochemical basis of the interaction between cystic fibrosis transmembrane conductance regulator and immunoglobulin-like repeats of filamin. J Biol Chem. 2010;285(22):17166–76.

64. Li C, Yu S, Nakamura F, Yin S, Xu J, Petrolla AA, et al. Binding of pro-prion to filamin A disrupts cytoskeleton and correlates with poor prognosis in pancreatic cancer. J Clin Invest. 2009;119(9):2725–36.

65. Li C, Yu S, Nakamura F, Pentikäinen OT, Singh N, Yin S, et al. Pro-prion binds filamin A, facilitating its interaction with integrin β1, and contributes to melanomagenesis. J Biol Chem. 2010;285(39):30328–39.

66. Liu G, Thomas L, Warren RA, Enns CA, Cunningham CC, Hartwig JH, et al. Cytoskeletal protein ABP-280 directs the intracellular trafficking of furin and modulates proprotein processing in the endocytic pathway. J Cell Biol. 1997;139(7):1719–33.

67. Hjalm G, MacLeod RJ, Kifor O, Chattopadhyay N, Brown EM. Filamin-A binds to the carboxyl-terminal tail of the calcium-sensing receptor, an interaction that participates in CaR-mediated activation of mitogen-activated protein kinase. J Biol Chem. 2001/06/08. 2001;276(37):34880–7.

68. Awata H, Huang C, Handlogten ME, Miller RT. Interaction of the calcium-sensing receptor and filamin, a potential scaffolding protein. J Biol Chem. 2001/06/08. 2001;276(37):34871–9.

69. Zhang M, Breitwieser GE. High Affinity Interaction with Filamin A Protects against Calcium-sensing Receptor Degradation. J Biol Chem [Internet]. 2005;280(12):11140–6. Available from: http://www.jbc.org/content/280/12/11140.abstract

70. Eun YK, Ridgway LD, Dryer SE. Interactions with filamin A stimulate surface expression of large-conductance Ca2+-activated K+ channels in the absence of direct actin binding. Mol Pharmacol. 2007;72(3):622–30.

71. Donaldson JC, Dise RS, Ritchie MD, Hanks SK. Nephrocystin-conserved domains involved in targeting to epithelial cell-cell junctions, interaction with filamins, and establishing cell polarity. J Biol Chem. 2002;277(32):29028–35.

72. Nikki M, Inen JM, Lehto VP. FAP52 regulates actin organization via binding to filamin. J Biol Chem. 2002;277(13):11432–40.

73. Begonja AJ, Pluthero FG, Suphamungmee W, Giannini S, Christensen H, Leung R, et al. FlnA binding to PACSIN2 F-BAR domain regulates membrane tubulation in megakaryocytes and platelets. Blood. 2015;126(1):80–8.

74. Armstrong LJ, Heath VL, Sanderson S, Kaur S, Beesley JFJ, Herbert JMJ, et al. ECSM2, an endothelial specific filamin a binding protein that mediates chemotaxis. Arterioscler Thromb Vasc Biol. 2008;28(9):1640–6.

75. Nagano T, Yoneda T, Hatanaka Y, Kubota C, Murakami F, Sato M. Filamin A-interacting protein (FILIP) regulates cortical cell migration out of the ventricular zone. Nat Cell Biol. 2002;4(7):495–501.

76. Leonardi A, Ellinger-Ziegelbauer H, Franzoso G, Brown K, Siebenlist U. Physical and functional interaction of filamin (actin-binding protein- 280) and tumor necrosis factor receptor-associated factor 2. J Biol Chem. 2000;275(1):271–8.

77. Huang C, Miller RT, Freter CE. Signaling regulation and role of filamin A cleavage in Ca2+-stimulated migration of androgen receptor-deficient prostate cancer cells. Oncotarget. 2017;8(3):3840.

78. Grimbert P, Valanciute A, Audard V, Lang P, Guellaën G, Sahali D. The Filamin-A is a partner of Tc-mip, a new adapter protein involved in c-maf-dependent Th2 signaling pathway. Mol Immunol. 2004;40(17):1257–61.

79. Paudyal P, Shrestha S, Madanayake T, Shuster CB, Rohrschneider LR, Rowland A, et al. Grb7 and Filamin-a associate and are colocalized to cell membrane ruffles upon EGF stimulation. J Mol Recognit. 2013;26(11):532–41.

80. Nishimura A, Shimauchi T, Tanaka T, Shimoda K, Toyama T, Kitajima N, et al. Hypoxia-induced interaction of filamin with Drp1 causes mitochondrial hyperfission-associated myocardial senescence. Sci Signal. 2018;11(556).

81. Nguyen LXT, Chan SM, Ngo TD, Raval A, Kim KK, Majeti R, et al. Interaction of TIF-90 and filamin A in the regulation of rRNA synthesis in leukemic cells. Blood. 2014;124(4):579–89.

82. Nakamura F, Pudas R, Heikkinen O, Permi P, Kilpeläinen I, Munday AD, et al. The structure of the GPIb-filamin A complex. Blood. 2006;107(5):1925–32.

83. Rider L, Diakonova M. Adapter protein sh2b1β binds filamin A to regulate prolactin-dependent cytoskeletal reorganization and cell motility. Mol Endocrinol. 2011;25(7):1231–43.

84. Brückner A, Polge C, Lentze N, Auerbach D, Schlattner U. Yeast two-hybrid, a powerful tool for systems biology. Int J Mol Sci. 2009;10(6):2763–88.

85. Takafuta T, Wu G, Murphy GF, Shapiro SS. Human β-filamin is a new protein that interacts with the cytoplasmic tail of glycoprotein Ibα. J Biol Chem. 1998;273(28):17531–8.

86. Xie Z, Xu W, Davie EW, Chung DW. Molecular cloning of human ABPL, an actin-binding protein homologue. Biochem Biophys Res Commun. 1998;251(3):914–9.

87. Mao Z, Nakamura F. Structure and function of filamin c in the muscle z-disc. Int J Mol Sci. 2020;21(8):17–9.

88. Hannan FM, Kallay E, Chang W, Brandi ML, Thakker R V. The calcium-sensing receptor in physiology and in calcitropic and noncalcitropic diseases. Nat Rev Endocrinol [Internet]. 2018;15(1):33–51. Available from: http://dx.doi.org/10.1038/s41574-018-0115-0

89. Washburn DLS, Anderson JW, Ferguson A V. The calcium receptor modulates the hyperpolarization-activated current in subfornical organ neurons. Neuroreport. 2000;11(14):3231–5.

90. Brennan SC, Wilkinson WJ, Tseng H-E, Finney B, Monk B, Dibble H, et al. The extracellular calcium-sensing receptor regulates human fetal lung development via

CFTR. Sci Rep. 2016;6:21975.

91. Pollak MR, Brown EM, Chou Y-HW, Hebert SC, Marx SJ, Stelnmann B, et al. Mutations in the human Ca2+-sensing receptor gene cause familial hypocalciuric hypercalcemia and neonatal severe hyperparathyroidism. Cell. 1993;75(7):1297–303.

92. Vahe C, Benomar K, Espiard S, Coppin L, Jannin A, Odou MF, et al. Diseases associated with calcium-sensing receptor. Orphanet J Rare Dis. 2017;12(1):1–9.

93. Bastepe M. A gain-of-function CASR mutation causing hypocalcemia in a recessive manner. J Clin Endocrinol Metab. 2018;103(9):3514–5.

94. Lienhardt A, Garabédian M, Bai M, Sinding C, Zhang Z, Lagarde J-P, et al. A large homozygous or heterozygous in-frame deletion within the calcium-sensing receptor's carboxylterminal cytoplasmic tail that causes autosomal dominant hypocalcemia. J Clin Endocrinol Metab. 2000;85(4):1695–702.

95. Pollak MR, Brown EM, Estep HL, McLaine PN, Kifor O, Park J, et al. Autosomal dominant hypocalcaemia caused by a Ca 2+-sensing receptor gene mutation. Nat Genet. 1994;8(3):303–7.

96. Vezzoli G, Terranegra A, Aloia A, Arcidiacono T, Milanesi L, Mosca E, et al. Decreased transcriptional activity of calcium-sensing receptor gene promoter 1 is associated with calcium nephrolithiasis. J Clin Endocrinol Metab. 2013;98(9):3839–47.

97. Vezzoli G, Tanini A, Ferrucci L, Soldati L, Bianchin C, Franceschelli F, et al. Influence of calcium-sensing receptor gene on urinary calcium excretion in stone-forming patients. J Am Soc Nephrol. 2002;13(10):2517–23.

98. Mingione A, Verdelli C, Ferrero S, Vaira V, Guarnieri V, Scillitani A, et al. Filamin A is reduced and contributes to the CASR sensitivity in human parathyroid tumors. J Mol Endocrinol. 2017;58(2):91–103.

99. Rodriguez M, Nemeth E, Martin D. The calcium-sensing receptor: a key factor in the pathogenesis of secondary hyperparathyroidism. Am J Physiol Physiol. 2005;288(2):F253–64.

100. Chang W, Tu C, Chen T-H, Komuves L, Oda Y, Pratt SA, et al. Expression and signal transduction of calcium-sensing receptors in cartilage and bone. Endocrinology. 1999;140(12):5883–93.

101. Ho C, Conner DA, Pollak MR, Ladd DJ, Kifor O, Warren HB, et al. A mouse model of human familial hypocalciuric hypercalcemia and neonatal severe hyperparathyroidism. Nat Genet. 1995;11(4):389–94.

102. Garner SC, Pi M, Tu Q, Quarles LD. Rickets in cation-sensing receptor-deficient mice: an unexpected skeletal phenotype. Endocrinology [Internet]. 2001;142(9):3996–4005. Available from: https://doi.org/10.1210/endo.142.9.8364

103. Tu Q, Pi M, Karsenty G, Simpson L, Liu S, Quarles LD. Rescue of the skeletal phenotype in CasR-deficient mice by transfer onto the Gcm2 null background. J Clin Invest. 2003;111(7):1029–37.

104. Kos CH, Karaplis AC, Peng J-B, Hediger MA, Goltzman D, Mohammad KS, et al. The calcium-sensing receptor is required for normal calcium homeostasis independent of parathyroid hormone. J Clin Invest. 2003;111(7):1021–8.

105. Rodriguez L, Tu C, Cheng Z, Chen T-H, Bikle D, Shoback D, et al. Expression and functional assessment of an alternatively spliced extracellular Ca2+-sensing receptor in

growth plate chondrocytes. Endocrinology. 2005;146(12):5294–303.

106. Oda Y, Tu C-L, Chang W, Crumrine D, Kömüves L, Mauro T, et al. The calcium sensing receptor and its alternatively spliced form in murine epidermal differentiation. J Biol Chem. 2000;275(2):1183–90.

107. Chang W, Tu C, Chen T-H, Bikle D, Shoback D. The extracellular calcium-sensing receptor (CaSR) is a critical modulator of skeletal development. Sci Signal. 2008;1(35):ra1–ra1.

108. Egbuna O, Quinn S, Kantham L, Butters R, Pang J, Pollak M, et al. The full-length calcium-sensing receptor dampens the calcemic response to 1α, 25 (OH) 2 vitamin D3 in vivo independently of parathyroid hormone. Am J Physiol Physiol. 2009;297(3):F720–8.

109. Dvorak MM, Chen T-H, Orwoll B, Garvey C, Chang W, Bikle DD, et al. Constitutive activity of the osteoblast Ca2+-sensing receptor promotes loss of cancellous bone. Endocrinology. 2007;148(7):3156–63.

110. Yamaguchi T, Chattopadhyay N, Kifor O, Butters JR RR, Sugimoto T, Brown EM, et al. Mouse Osteoblastic Cell Line (MC3T3-E1) Expresses Extracellular Calcium (Ca2+ o)–Sensing Receptor and Its Agonists Stimulate Chemotaxis and Proliferation of MC3T3-E1 Cells. J Bone Miner Res [Internet]. 1998;13(10):1530–8. Available from: https://asbmr.onlinelibrary.wiley.com/doi/abs/10.1359/jbmr.1998.13.10.1530

111. Dvorak MM, Siddiqua A, Ward DT, Carter DH, Dallas SL, Nemeth EF, et al. Physiological changes in extracellular calcium concentration directly control osteoblast function in the absence of calciotropic hormones. Proc Natl Acad Sci. 2004;101(14):5140–5.

112. Yasukawa T, Hayashi M, Tanabe N, Tsuda H, Suzuki Y, Kawato T, et al. Involvement of the calcium-sensing receptor in mineral trioxide aggregate-induced osteogenic gene expression in murine MC3T3-E1 cells. Dent Mater J. 2017;36(4):469–75.

113. Pi M, Spurney RF, Tu Q, Hinson T, Quarles LD. Calcium-sensing receptor activation of rho involves filamin and rho-guanine nucleotide exchange factor. Endocrinology. 2002;143(10):3830–8.

114. Thiel G, Lesch A, Keim A. Transcriptional response to calcium-sensing receptor stimulation. Endocrinology. 2012;153(10):4716–28.

115. Rey O, Young SH, Yuan J, Slice L, Rozengurt E. Amino acid-stimulated Ca2+ oscillations produced by the Ca2+-sensing receptor are mediated by a phospholipase C/inositol 1, 4, 5-trisphosphate-independent pathway that requires G12, Rho, filamin-A, and the actin cytoskeleton. J Biol Chem. 2005;280(24):22875–82.

116. Tu C-L, Chang W, Bikle DD. The calcium-sensing receptor-dependent regulation of cell–cell adhesion and keratinocyte differentiation requires Rho and filamin A. J Invest Dermatol. 2011;131(5):1119–28.

117. Rodríguez-Carballo E, Gámez B, Ventura F. p38 MAPK signaling in osteoblast differentiation. Front cell Dev Biol. 2016;4:40.

118. Wade EM, Daniel PB, Jenkins ZA, McInerney-Leo A, Leo P, Morgan T, et al. Mutations in MAP3K7 that Alter the Activity of the TAK1 Signaling Complex Cause Frontometaphyseal Dysplasia. Am J Hum Genet [Internet]. 2016;99(2):392–406. Available from: https://doi.org/10.1016/j.ajhg.2016.05.024

119. Wade EM, Jenkins ZA, Daniel PB, Morgan T, Addor MC, Adés LC, et al. Autosomal dominant frontometaphyseal dysplasia: Delineation of the clinical phenotype. Am J Med Genet Part A. 2017;173(7):1739–46.

120. Yamaguchi T, Chattopadhyay N, Kifor O, Sanders JL, Brown EM. Activation of p42/44 and p38 mitogen-activated protein kinases by extracellular calcium-sensing receptor agonists induces mitogenic responses in the mouse osteoblastic MC3T3-E1 cell line. Biochem Biophys Res Commun. 2000;279(2):363–8.

121. Walter M. Relative Quantification of Multiple mRNA Targets and Reference Genes in Spinocerebellar Ataxia.

122. Kent WJ, Sugnet CW, Furey TS, Roskin KM, Pringle TH, Zahler AM, et al. The human genome browser at UCSC. Genome Res. 2002;12(6):996–1006.

123. Edgar RC. MUSCLE: multiple sequence alignment with high accuracy and high throughput. Nucleic Acids Res. 2004;32(5):1792–7.

124. Stecher G, Tamura K, Kumar S. Molecular evolutionary genetics analysis (MEGA) for macOS. Mol Biol Evol. 2020;37(4):1237–9.

125. Aartsma-Rus A. Overview on AON design. In: Methods in Molecular Biology. Springer; 2012. p. 117–29.

126. Gruber AR, Lorenz R, Bernhart SH, Neuböck R, Hofacker IL. The Vienna RNA Websuite. Nucleic Acids Res [Internet]. 2008;36(suppl_2):W70–4. Available from: https://doi.org/10.1093/nar/gkn188

127. Desmet F-O, Hamroun D, Lalande M, Collod-Béroud G, Claustres M, Béroud C. Human Splicing Finder: an online bioinformatics tool to predict splicing signals. Nucleic Acids Res. 2009;37(9):e67–e67.

128. Bellaousov S, Reuter JS, Seetin MG, Mathews DH. RNAstructure: web servers for RNA secondary structure prediction and analysis. Nucleic Acids Res. 2013;41(W1):W471–4.

129. Schneider CA, Rasband WS, Eliceiri KW. NIH Image to ImageJ: 25 years of image analysis. Nat Methods. 2012;9(7):671–5.

130. Kodama H, Amagai Y, Sudo H, Kasai S, Yamamoto S. Establishment of a clonal osteogenic cell line from newborn mouse calvaria. Japanese J Oral Biol. 1981;23(4):899–901.

131. Sudo H, Kodama H-A, Amagai Y, Yamamoto S, Kasai S. In vitro differentiation and calcification in a new clonal osteogenic cell line derived from newborn mouse calvaria. J Cell Biol. 1983;96(1):191–8.

132. Franceschi RT, Iyer BS, Cui Y. Effects of ascorbic acid on collagen matrix formation and osteoblast differentiation in murine MC3T3-E1 cells. J Bone Miner Res. 1994;9(6):843–54.

133. Marsh ME, Munne AM, Vogel JJ, Cui Y, Franceschi RT. Mineralization of bone-like extracellular matrix in the absence of functional osteoblasts. J Bone Miner Res. 1995;10(11):1635–43.

134. Bellows CG, Aubin JE, Heersche JNM, Antosz ME. Mineralized bone nodules formedin vitro from enzymatically released rat calvaria cell populations. Calcif Tissue Int. 1986;38(3):143–54.

135. Nakashima K, Zhou X, Kunkel G, Zhang Z, Deng JM, Behringer RR, et al. The novel

zinc finger-containing transcription factor osterix is required for osteoblast differentiation and bone formation. Cell. 2002;108(1):17–29.

136. Karsenty G, Ducy P, Starbuck M, Priemel M, Shen J. Cbfa1 as a regulator of osteoblast differentiation and function. Bone (New York, NY). 1999;25(1):107–8.

137. Kaneto CM, Lima PSP, Zanette DL, Oliveira TYK, de Assis Pereira F, Lorenzi JCC, et al. Osteoblastic differentiation of bone marrow mesenchymal stromal cells in Bruck Syndrome. BMC Med Genet. 2016;17(1):1–9.

138. Hughes AL, Yeager M. Comparative evolutionary rates of introns and exons in murine rodents. J Mol Evol. 1997;45(2):125–30.

139. He P, Williams BA, Trout D, Marinov GK, Amrhein H, Berghella L, et al. The changing mouse embryo transcriptome at whole tissue and single-cell resolution. Nature. 2020;583(7818):760–7.

140. Springer MS, Murphy WJ, Eizirik E, O'Brien SJ. Placental mammal diversification and the Cretaceous–Tertiary boundary. Proc Natl Acad Sci. 2003;100(3):1056–61.

141. Letunic I, Bork P. Interactive Tree Of Life (iTOL) v4: recent updates and new developments. Nucleic Acids Res. 2019;47(W1):W256–9.

142. Vertebrate Multiz Alignment & Conservation (100 Species) [Internet]. [cited 2020 Oct 23]. Available from: https://genome.ucsc.edu/cgi-bin/hgTrackUi?hgsid=925777277_e0v07FxycaGCS5cMsML5klBApQuL&c=chrX&g=cons100way

143. Ponten J, Saksela E. Two established in vitro cell lines from human mesenchymal tumours. Int J cancer. 1967;2(5):434–47.

144. Mutsaers AJ, Walkley CR. Cells of origin in osteosarcoma: mesenchymal stem cells or osteoblast committed cells? Bone. 2014;62:56–63.

145. Pautke C, Schieker M, Tischer T, Kolk A, Neth P, Mutschler W, et al. Characterization of osteosarcoma cell lines MG-63, Saos-2 and U-2 OS in comparison to human osteoblasts. Anticancer Res. 2005/03/02. 2004;24(6):3743–8.

146. Orimo H, Goseki-Sone M, Hosoi T, Shimada T. Functional assay of the mutant tissue-nonspecific alkaline phosphatase gene using U2OS osteoblast-like cells. Mol Genet Metab. 2008;94(3):375–81.

147. Havens MA, Hastings ML. Splice-switching antisense oligonucleotides as therapeutic drugs. Nucleic Acids Res. 2016;44(14):6549–63.

148. Hang J, Wan R, Yan C, Shi Y. Structural basis of pre-mRNA splicing. Science (80- ). 2015;349(6253):1191–8.

149. Dieffenbach CW, Lowe TMJ, Dveksler GS. General concepts for PCR primer design. Genome Res. 1993;3(3).

150. Pi M, Quarles LD. Osteoblast calcium-sensing receptor has characteristics of ANF/7TM receptors. J Cell Biochem. 2005;95(6):1081–92.

151. Caverzasio J, Thouverey C. Activation of FGF receptors is a new mechanism by which strontium ranelate induces osteoblastic cell growth. Cell Physiol Biochem. 2011;27(3–4):243–50.

152. D'Espessailles A, Mora YA, Fuentes C, Cifuentes M. Calcium-sensing receptor activates the NLRP3 inflammasome in LS14 preadipocytes mediated by ERK1/2 signaling. J Cell

Physiol. 2018;233(8):6232–40.

153. Uhlen M, Zhang C, Lee S, Sjöstedt E, Fagerberg L, Bidkhori G, et al. A pathology atlas of the human cancer transcriptome. Science (80- ). 2017;357(6352).

154. Kawashima N, Hashimoto K, Kuramoto M, Bakhit A, Wakabayashi Y, Okiji T. A Novel Bioactive Endodontic Sealer Containing Surface-Reaction-Type Prereacted Glass-Ionomer Filler Induces Osteoblast Differentiation. Materials (Basel). 2020;13(20):4477.

155. Mizumachi H, Yoshida S, Tomokiyo A, Hasegawa D, Hamano S, Yuda A, et al. Calcium-sensing receptor-ERK signaling promotes odontoblastic differentiation of human dental pulp cells. Bone. 2017;101:191–201.

156. Centeno PP, Herberger A, Mun H-C, Tu C, Nemeth EF, Chang W, et al. Phosphate acts directly on the calcium-sensing receptor to stimulate parathyroid hormone secretion. Nat Commun. 2019;10(1):1–12.

157. Fan Q, Li Y, Sun Q, Jia Y, He C, Sun T. miR-532-3p inhibits osteogenic differentiation in MC3T3-E1 cells by downregulating ETS1. Biochem Biophys Res Commun. 2020;

158. Warita K, Aoki R, Kitamura N, Shibuya I, Hosaka YZ. The precursor osteoblast-like cell, MC3T3-E1 cell line, enhances sodium–calcium exchanger 1 (Ncx1) gene expression by stretch stimuli prior to osteoblast differentiation. J Vet Med Sci. 2019;18–766.

159. Wu J, Ren W, Zheng Z, Huang Z, Liang T, Li F, et al. Mmu_circ_003795 regulates osteoblast differentiation and mineralization in MC3T3-E1 and MDPC23 by targeting COL15A1. Mol Med Rep. 2020;22(3):1737–46.

160. Okamura K, Inagaki Y, Matsui TK, Matsubayashi M, Komeda T, Ogawa M, et al. RT-qPCR analyses on the osteogenic differentiation from human iPS cells: An investigation of reference genes. bioRxiv. 2020;

161. Tang J, Lin X, Zhong J, Xu F, Wu F, Liao X, et al. miR-124 regulates the osteogenic differentiation of bone marrow-derived mesenchymal stem cells by targeting Sp7. Mol Med Rep. 2019;19(5):3807–14.

162. Hwang PW, Horton JA. Variable osteogenic performance of MC3T3-E1 subclones impacts their utility as models of osteoblast biology. Sci Rep. 2019;9(1):1–9.

163. Hughes FJ, Aubin JE. Culture of cells of the osteoblast lineage BT - Methods in Bone Biology. In: Arnett TR, Henderson B, editors. Boston, MA: Springer US; 1998. p. 1–49. Available from: https://doi.org/10.1007/978-0-585-38227-2_1

164. Czekanska EM, Stoddart MJ, Richards RG, Hayes JS. In search of an osteoblast cell model for in vitro research. Eur Cells Mater. 2012;24:1–17.

165. Zhang W, Zhuang Y, Zhang Y, Yang X, Zhang H, Wang G, et al. Uev1A facilitates osteosarcoma differentiation by promoting Smurf1-mediated Smad1 ubiquitination and degradation. Cell Death Dis. 2017;8(8):e2974–e2974.

166. Akan P, Alexeyenko A, Costea PI, Hedberg L, Solnestam BW, Lundin S, et al. Comprehensive analysis of the genome transcriptome and proteome landscapes of three tumor cell lines. Genome Med. 2012;4(11):86.

167. Al-Romaih K, Somers GR, Bayani J, Hughes S, Prasad M, Cutz J-C, et al. Modulation by decitabine of gene expression and growth of osteosarcoma U2OS cells in vitro and in xenografts: identification of apoptotic genes as targets for demethylation. Cancer Cell Int. 2007;7(1):14.

168. Hanna H, Mir LM, Andre FM. In vitro osteoblastic differentiation of mesenchymal stem cells generates cell layers with distinct properties. Stem Cell Res Ther. 2018;9(1):203.

169. Claeys L, Bravenboer N, Eekhoff EMW, Micha D. Human Fibroblasts as a Model for the Study of Bone Disorders. Front Endocrinol (Lausanne). 2020;11.

170. Klontzas ME, Vernardis SI, Heliotis M, Tsiridis E, Mantalaris A. Metabolomics analysis of the osteogenic differentiation of umbilical cord blood mesenchymal stem cells reveals differential sensitivity to osteogenic agents. Stem Cells Dev. 2017;26(10):723–33.

171. Ansari N, Sims NA. The Cells of Bone and Their Interactions. In: Handbook of Experimental Pharmacology [Internet]. Berlin, Heidelberg: Springer, Berlin, Heidelberg; 2019. p. 1–25. Available from: https://doi.org/10.1007/164_2019_343

172. Fay MM, Lyons SM, Ivanov P. RNA G-quadruplexes in biology: principles and molecular mechanisms. J Mol Biol. 2017;429(14):2127–47.

173. Puig Lombardi E, Londoño-Vallejo A. A guide to computational methods for G-quadruplex prediction. Nucleic Acids Res. 2020;48(1):1–15.

174. Strobel EJ, Angela MY, Lucks JB. High-throughput determination of RNA structures. Nat Rev Genet. 2018;19(10):615–34.

175. Di Antonio M, Rodriguez R, Balasubramanian S. Experimental approaches to identify cellular G-quadruplex structures and functions. Methods. 2012;57(1):84–92.

176. Pickrell JK, Pai AA, Gilad Y, Pritchard JK. Noisy splicing drives mRNA isoform diversity in human cells. PLoS Genet. 2010;6(12):e1001236.

177. Wang Y, Liu J, Huang BO, Xu Y, Li J, Huang L, et al. Mechanism of alternative splicing and its regulation. Biomed reports. 2015;3(2):152–8.

178. Dvinge H. Regulation of alternative mRNA splicing: old players and new perspectives. FEBS Lett. 2018;592(17):2987–3006.

179. Barbosa-Morais NL, Irimia M, Pan Q, Xiong HY, Gueroussov S, Lee LJ, et al. The evolutionary landscape of alternative splicing in vertebrate species. Science (80- ). 2012;338(6114):1587–93.

180. Gao Q, Sun W, Ballegeer M, Libert C, Chen W. Predominant contribution of cis-regulatory divergence in the evolution of mouse alternative splicing. Mol Syst Biol. 2015;11(7):816.

181. Baralle D, Baralle M. Splicing in action: assessing disease causing sequence changes. J Med Genet. 2005;42(10):737–48.

182. Tacke R, Manley JL. Determinants of SR protein specificity. Curr Opin Cell Biol. 1999;11(3):358–62.

183. Jain N, Lin H-C, Morgan CE, Harris ME, Tolbert BS. Rules of RNA specificity of hnRNP A1 revealed by global and quantitative analysis of its affinity distribution. Proc Natl Acad Sci. 2017;114(9):2206–11.

184. Goltzman D, Hendy GN. The calcium-sensing receptor in bone-mechanistic and therapeutic insights. Nat Rev Endocrinol. 2015;11(5):298–307.

185. Edfors F, Danielsson F, Hallström BM, Käll L, Lundberg E, Pontén F, et al. Gene-specific correlation of RNA and protein levels in human cells and tissues. Mol Syst Biol. 2016;12(10):883.

186. Cavanaugh A, McKenna J, Stepanchick A, Breitwieser GE. Calcium-sensing receptor biosynthesis includes a cotranslational conformational checkpoint and endoplasmic reticulum retention. J Biol Chem. 2010;285(26):19854–64.

187. Caverzasio J. Strontium ranelate promotes osteoblastic cell replication through at least two different mechanisms. Bone. 2008;42(6):1131–6.

188. Ogata S, Kubota Y, Satoh S, Ito S, Takeuchi H, Ashizuka M, et al. Ca2+ stimulates COX-2 expression through calcium-sensing receptor in fibroblasts. Biochem Biophys Res Commun. 2006;351(4):808–14.

189. Sun Y, Liu M, Li H, Shi S, Zhao Y, Wang R, et al. Calcium-sensing receptor induces rat neonatal ventricular cardiomyocyte apoptosis. Biochem Biophys Res Commun. 2006;350(4):942–8.

190. Brennan SC, Mun H-C, Leach K, Kuchel PW, Christopoulos A, Conigrave AD. Receptor expression modulates calcium-sensing receptor mediated intracellular Ca2+ mobilization. Endocrinology. 2015;156(4):1330–42.

191. Tfelt-Hansen J, MacLeod RJ, Chattopadhyay N, Yano S, Quinn S, Ren X, et al. Calcium-sensing receptor stimulates PTHrP release by pathways dependent on PKC, p38 MAPK, JNK, and ERK1/2 in H-500 cells. Am J Physiol Metab. 2003;285(2):E329–37.

192. Cristofaro V, Hofer A, Yalla S, Curci S, Sullivan M. Activation of calcium-sensing receptor modulates bladder smooth muscle contraction. In: NEUROUROLOGY AND URODYNAMICS. WILEY-LISS DIV JOHN WILEY & SONS INC, 111 RIVER ST, HOBOKEN, NJ 07030 USA; 2005. p. 439–41.

193. Sebastian A, Loots GG. Genetics of Sost/SOST in sclerosteosis and van Buchem disease animal models. Metabolism. 2018;80:38–47.

194. Bonewald LF. The role of the osteocyte in bone and nonbone disease. Endocrinol Metab Clin. 2017;46(1):1–18.

195. Bolland MJ, Grey A. Ten years too long: strontium ranelate, cardiac events, and the European Medicines Agency. Bmj. 2016;354:i5109.

196. Zhu F, Nair RR, Fisher EMC, Cunningham TJ. Humanising the mouse genome piece by piece. Nat Commun. 2019;10(1):1–13.

197. Hwang B, Lee JH, Bang D. Single-cell RNA sequencing technologies and bioinformatics pipelines. Exp Mol Med. 2018;50(8):1–14.

# Appendices

# Appendix A

### Primers for qPCR

| Target gene | Forward primer | Reverse primer | Product size (bp) | Efficiency | Cp range |
|---|---|---|---|---|---|
| *Gapdh* | CATCTTCCAGGAGCGAGACC | GGCGGAGATGATGACCCTTT | 145 | 2.018 | 17.59-31.81 |
| *Ppia* | GTCCTGGCATCTTGTCCATG | TGCCTTCTTTCACCTTCCCA | 126 | 1.961 | 18.00-32.00 |
| *Rps29* | CCGACTCGTTCCTTTCTCCT | GCACATGTTCAGCCCGTATT | 158 | 1.916 | 21.51-37.13 |
| *Flna* | CCAACAGCCCCTTCCAAGTT | CCACCATGGGCCTCTCTG | 141 | 1.933 | 21.56-34.53 |
| *Sp7* | CTCGGTTCTCTCCATCTGCC | TCTTTGTGCCTCCTTTCCCC | 188 | 1.976 | 27.34-40.00 |
| *Runx2* | ATCCCCATCCATCCACTCCA | GAACTGCCTGGGGTCTGAAA | 196 | 1.824 | 24.34-40.00 |
| *Col1a1* | CCAGGTCCTAAGGGTGACAG | AATGGGACCAGTCAGACCAC | 93 | 1.941 | 21.94-36.40 |

# Appendix B

### Transcripts used for alignment of *FLNA* sequences

| Species | Ensembl transcript ID | Exon # |
|---|---|---|
| Human (*Homo sapiens*) | ENST00000369850.10 | 31 |
| Squirrel (*Ictidomys tridecemlineatus*) | ENSSTOT00000005104.3 | 31 |
| Lesser Egyptian jerboa (*Jaculus jaculus*) | ENSJJAT00000018989.1 | 30 |
| Prairie vole (*Microtus ochrogaster*) | ENSMOCT00000010136.1 | 31 |
| Chinese hamster (*Cricetulus griseus*) | ENSCGRT00000003103.1 | 30 |
| Mouse (*Mus musculus*) | ENSMUST00000033699.12 | 30 |
| Rat (*Rattus norvegicus*) | ENSRNOT00000079889.1 | 29 |
| Mole rat (*Heterocephalus glaber*) | ENSHGLT00000002405.1 | 30 |
| Guinea pig (*Cavia porcellus*) | ENSCPOT00000039584.1 | 30 |
| Brush tailed rat (*Octodon degus*) | ENSODET00000005460.1 | 30 |

# Appendix C

## RT-PCR primer sequences and optimised PCR conditions

| Target | Primer name | Sequence | Product size (bp) | PCR conditions | Notes |
|---|---|---|---|---|---|
| *Flna* exon 30-31 (mouse) | mFLNA F1 | GGGGAGGAGACGGTGATTAC | 251 | Standard | - |
| | mFLNA R1 | GTCTGCACTGTTGGTTGGTC | | | |
| *FLNA* exon 31-32 (human) | FC16F | CCATTCAGATTGGGGAGGAGA | 309 | Standard | - |
| | FLNA R9 | CCTGGGCGTAGGTGTACTGT | | | |
| *Casr* exon 2-3 (mouse) | mCaSR F | ATGGTTTGGCTACTGTTTGG | 319 | Touchdown + CES | From: Yamaguchi et al. (110) |
| | mCaSR R | CAGAGCCTTGGAGACGGTGT | | | |
| *CASR* exon 6-7 (human) | hCaSR F | GATGAGACAGATGCCAGTGC | 135 | Touchdown + CES | From: D'Espessailles et al. (152)<br>Off-target amplification of *RPS2* |
| | hCaSR R | AAAGAGGGTGAGTGCGATCC | | | |
| *CASR* exon 2-3 (human) | CaSR2-3 F | AATCAAGGCCGGAGTCTGTG | 118 | n/a | Primer dimers only |
| | CaSR 2-3 R | AAGTTGGGAAGAAGGGCTGG | | | |
| *CASR* exon 6-7 (human) | CaSR 6-7 F | ACCTGCTGCTTTGAGTGTGT | 180 | n/a | Primer dimers only |
| | hCaSR R | AAAGAGGGTGAGTGCGATCC | | | |
| *CASR* exon 1-4 (human) | CasR-F13 | ACCGAGGTCTTGCGGCACAGGCAAC | 820 | n/a | No product when CaSR plasmid was used as template |
| | CasR-R17 | GTTGCTGAGGAGTCTGCTGGAG | | | |
| *CASR* exon 2-4 (human) | CasR-F10 | ACCATGGCATTTTATAGCTGCTGCTGG | 531 | Touchdown + CES | Off-target amplification of *GNAS, NAT10* |
| | CasR-R17 | GTTGCTGAGGAGTCTGCTGGAG | | | |
| *CASR* exon 2-4 (human) | CasR-F9 | ACCATGGCATTTTATAGCTGCTGCT | 531 | n/a | Off-target amplification only |
| | CasR-R17 | GTTGCTGAGGAGTCTGCTGGAG | | | |
| *CASR* exon 5-7 (human) | CasR-F6 | AGACTCTTCATCAACGAGGAG | 300 | n/a | Off-target amplification only |
| | hCaSR R | AAAGAGGGTGAGTGCGATCC | | | |

# Appendix D

### Oligos of shRNA1 and shRNA2 with the overhang sequences

| Name | Sequence |
|---|---|
| **shRNA1 F** | TATATCTTGTGGAAAGGACGCCGGCTAGAAGCTCCCATGGCAATGCTCGAGCATTGCCATGGGAGCTTCTAGTTTTTGATCTACCTCGAGGTTTCTAG |
| **shRNA1 R** | CTAGAAACCTCGAGGTAGATCAAAAACTAGAAGCTCCCATGGCAATGCTCGAGCATTGCCATGGGAGCTTCTAGCCGGCGTCCTTTCCACAAGATATA |
| **shRNA2 F** | TATATCTTGTGGAAAGGACGCACCGCCTACTGCTTTAATTAAAGGCGAACCTTTAATTAAAGCAGTAGGCTTTTATCTACCTCGAGGTTTCTAG |
| **shRNA2 R** | CTAGAAACCTCGAGGTAGATAAAAGCCTACTGCTTTAATTAAAGGTTCGCCTTTAATTAAAGCAGTAGGCGGTGCGTCCTTTCCACAAGATATA |

### Primers for the production of hU6 and eGFP fragments

| Fragment | Primer name | Primer sequence | Product size (bp) |
|---|---|---|---|
| **hU6 (shRNA1 overhang)** | hU6 PvuI F | CGTCAGCTTACCTTTTTGGCAGCGATAAGGTCGGGCAGGAAGAGGGCCTAT | 303 |
| | hU6 shRNA1 R | CCATGGGAGCTTCTAGCCGGCGTCCTTTCCACAAGATATA | |
| **hU6 (shRNA2 overhang)** | hU6 PvuI F | CGTCAGCTTACCTTTTTGGCAGCGATAAGGTCGGGCAGGAAGAGGGCCTAT | 303 |
| | hU6 shRNA 2 R | AATTAAAGCAGTAGGCGGTGCGTCCTTTCCACAAGATATA | |
| **eGFP** | eGFP Sal1 F | GGGCCCAAAGTACTAAAGATGGTGAGCAAGGGCGAGGAGCTGT | 756 |
| | pEGFP STOP R | CGTTATTACATGTTGGCGTTACTTGTACAGCTCGTCCATGCCGAGA | |

**Primers for colony PCR**

| Target | Primer name | Primer sequence | Product size (bp) | PCR conditions |
|---|---|---|---|---|
| **Insert of hU6-shRNA** | 5’ PvuI seq F | ACTCGACTCTGGCTCTATCGAATC | 562 (shRNA1)<br>558 (shRNA2) | Standard |
| | pSF CMV1-R | GTCTGTGAGCTGAAGGTACGCTG | | |
| **Insert of eGFP** | pSF CMV2 F2 | ATTCGACCAACCTTCCTTCGACACG | 934 with insert<br>(218, no insert) | Standard |
| | pSF Sal1-R | TAGAATGACACCTACTCAGACAATGC | | |

**Primers for sequencing plasmids**

| Primer name | Primer sequence |
|---|---|
| 5’ PvuI seq F | ACTCGACTCTGGCTCTATCGAATC |
| pSF CMV1-R | GTCTGTGAGCTGAAGGTACGCTG |
| pSF CMV2 F | CAGAAATTTATCCTTAAGGTCGTCA |
| EGFP seq F | GCGATGCCACCTACGGCAAGCTGAC |
| pSF Sal1-R | TAGAATGACACCTACTCAGACAATGC |
| CMV2 seq R | GCTTCATGTGGTCGGGGTAGCGGC |

# Appendix E

### Tris-HCl 0.5 M, pH 6.8

| | |
|---|---|
| UltraPure Tris Buffer (Invitrogen) | 30.285 g |
| HCl (ACS reagent, 37%; Sigma) | Add until pH is 6.8 |
| Distilled $H_2O$ | Make up to 500 mL |

### Tris-HCl 1.5 M, pH 8.8

| | |
|---|---|
| UltraPure Tris Buffer (Invitrogen) | 90.855 g |
| HCl (ACS reagent, 37%; Sigma) | Add until pH is 8.8 |
| Distilled $H_2O$ | Make up to 500 mL |

### 6X denaturing-SDS loading dye for western blot

| | |
|---|---|
| Tris-HCl 0.5 M, pH 6.8 (see below) | 3 mL |
| Glycerol 50% (Sigma) | 2 mL |
| SDS 20% (Sigma) | 4 mL |
| Bromophenol blue (BDH) | 0.01 % w/v |
| Distilled $H_2O$ | 1 mL |

Add 1 μL 2-mercaptoethanol (Sigma) to 5 μL of the above solution prior to use

**10% polyacrylamide gel with 0.1% SDS for western blot**

| | |
|---|---|
| Tris-HCl 1.5 M, pH 8.8 | 1500 µL |
| 40% Acrylamide/Bis solution, 19:1 (Bio-Rad) | 1500 µL |
| SDS 20% (Sigma) | 30 µL |
| Ammonium Persulfate, 1% w/v (Sigma) | 60 µL |
| TEMED (Sigma) | 5 µL |
| Distilled $H_2O$ | 2905 µL |

**Tris/Glycine running buffer with 0.1% SDS**

| | |
|---|---|
| UltraPure Tris Buffer (Invitrogen) | 2.42 g |
| Glycine (Sigma) | 11.53 g |
| SDS 20% (Sigma) | 4 mL |
| Distilled $H_2O$ | Make up to 800 mL |

**Tris/Glycine transfer buffer with 10% isopropanol**

| | |
|---|---|
| UltraPure Tris Buffer (Invitrogen) | 0.303 g |
| Glycine (Sigma) | 1.44 g |
| 2-Propanol (Merck) | 10mL |
| Distilled $H_2O$ | Make up to 100 mL |